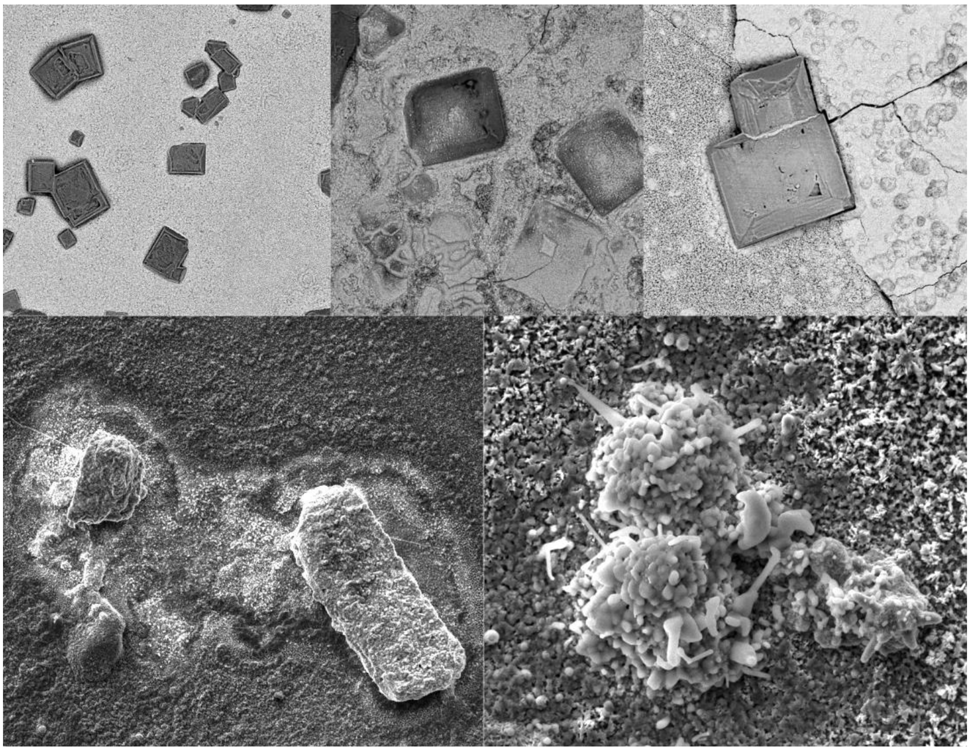

Alkali and zinc chlorides in waterwall tube corrosion:

Effects of pure salts and mixtures

Master of Science Thesis in the Master Degree Programme, *Materials Chemistry and Nanotechnology*

ANDREAS SLOMIAN

Department of Chemical and Biological Engineering
Division of Energy and Materials
CHALMERS UNIVERSITY OF TECHNOLOGY
Gothenburg, Sweden, 2013

Alkali and zinc chlorides in waterwall tube corrosion:

Effects of pure salts and mixtures

ANDREAS SLOMIAN

Examiner:
Prof. Jan-Erik Svensson

Supervisors:
Ass. Prof. Jesper Liske
Dr. Torbjörn Jonsson

Department of Chemical and Biological Engineering
CHALMERS UNIVERSITY OF TECHNOLOGY
Göteborg, Sweden 2013

Alkali and zinc chlorides in waterwall tube corrosion:
Effects of pure salts and mixtures
ANDREAS SLOMIAN

Department of Chemical and Biological Engineering
Chalmers University of Technology
SE-412 96 Göteborg
Sweden
Telephone + 46 (0)31-772 1000

Cover:
Top row: SEM images of NaCl crystals on T22 steel after 1 hour (left), 24 hours (middle) and 168 hours (right) of exposure. Bottom row: SEM images of local melt corrosion attack on T22 steel after 24 hours of exposure with a mixture of $NaCl/ZnCl_2$ (left) and $KCl/ZnCl_2$ (right) respectively.

Göteborg, Sweden 2013

Acknowledgements

First of all I would like to thank my supervisors Ass. Prof. Jesper Liske and Dr. Torbjörn Jonsson for their guidance and enthusiasm to share their knowledge with me. Furthermore, I would like to thank Prof. Jan-Erik Svensson for giving me the opportunity to write this thesis.

I would also like to extend my gratitude to Andrea Olivas and Erik Larsson for help and advice regarding practical work as well as for good discussions concerning laboratory exposures. Likewise, I would like to thank both Prof. Vratislav Langer for reading the part on XRD, Dr. Anders Kvist for help with SEM and Dr. Dongmei Zhao for help with IC.

Everyone at the HTC is acknowledged for providing a fun working environment.

Last but not least, I would like to thank my friends and family, especially my parents Jadwiga and Andrej Slomian: Without their love and support I highly doubt that I ever would have written this.

Abstract

In recent years, climate concerns and growing energy demands have caused a striving for the use of more renewable energy. As demand rises, the output levels from power production plants need to be as high as possible. Among the different renewable energy sources, biomass and municipal solid waste are the top contributors to the renewable heat and power generation in the EU. High temperature corrosion associated with certain species in biomass and municipal solid waste is, however, currently forcing a lower steam temperature in these plants, thus lowering the electric efficiency. One of the boiler components attacked by these corrosive species are the furnace waterwall tubes, which are suspected to suffer from a molten salt corrosion attack caused by low melting point eutectics. Since the corrosivity of these eutectics is not fully elucidated and their corrosion mechanism is still unclear, investigation of these systems is important in order to enable mitigation of waterwall corrosion in the future.

In this work, the corrosive behaviour of the two eutectic systems $NaCl/ZnCl_2$ and $KCl/ZnCl_2$ as well as their respective pure salts on T22 low alloyed steel has been studied in laboratory exposures. The exposures were performed in lab furnace systems at simplified boiler conditions for 1, 24 and 168 hours. Analysis consisted of gravimetry, SEM with EDX, XRD and IC.

The results showed that all salts accelerated the corrosion attack. The alkali salts yielded higher mass gains than their corresponding mixtures with $ZnCl_2$, while the $ZnCl_2$ system caused the lowest mass gain among the investigated salt systems, although exhibiting the most prominent signs of spallation. Even though indications of local melt attack were detected and the mixtures increased the loss of detectable chloride ions after exposure, the corrosion attack can possibly be explained by mechanisms other than salt melt corrosion. To further expand the knowledge of the eutectic systems investigated in this work, cross-sectional studies are suggested as a next step in the study of the corrosive properties of these mixtures.

Keywords: High temperature corrosion, biomass and waste incineration, chlorine induced corrosion, low melting point eutectics, waterwall tube corrosion, alkali chlorides, heavy metal chlorides

Table of Contents

1 Introduction

1.1 Background

In recent years, climate concerns have led to an increased use of biomass as fuel in waste fired boilers, as the use of renewable energy sources is much less straining on the environment in comparison to fossil fuels. However, these renewable fuels cause a much more corrosive environment in the boiler during combustion, which is mainly attributed to that renewable fuels have a different chemical composition than traditional fossil fuels. Since the furnaces may not be designed to fire biomass, this leads to a highly increased rate of corrosion. The faster corrosion can be mitigated by lowering the steam temperature, but this results in a decreased boiler efficiency and energy output. Alkali salts as well as heavy metals that form low melting point salts have been suspected to be the cause of this highly increased rate of corrosion. However, it is still not fully understood to which extent this actually occurs in boilers where biomass is incinerated. This study focuses on the corrosive behaviour of several chloride salts and mixtures of these on a low alloyed steel that would be of interest for use in commercial boilers.

1.2 Aim

The aim of this master's thesis is to investigate the effect of alkali- and heavy metal salts on the corrosion of low alloyed steels under similar conditions simulating the flue gas in biomass and waste fired heating boilers. By examining how these salts affect the initial corrosion attack, this work aims for an increased understanding of the actual corrosion phenomenon. This could be used for writing recommendations about different possible countermeasures that can be taken in order to mitigate attacks of this type.

1.3 Delimitations

- One material will be tested: T22 low alloyed carbon steel
- The metal samples will only be exposed to three different salts during this study: $ZnCl_2$, KCl and NaCl, as individual salt exposures and as mixed salt exposures.
- The sample exposures will be performed in controlled environments in laboratory tube furnaces; no field exposures will be performed.
- The sample exposures will be performed at 400°C.

1.4 Questions to be answered in the project

- What characterises a corrosion attack of this type?
- How do the different chlorides and mixtures of these affect the corrosion?
- How does the corrosion morphology look like and how does it affect the corrosion rate?

2 Biomass, waste and boilers

2.1 Shift in energy carriers

One of the most pressing environmental issues today is the global warming caused by emission of greenhouse gases, mainly CO_2, originating from the industry, transportation, domestic and service sectors. Even though naturally occurring in the atmosphere, accumulation of CO_2 is caused by combustion of fossil fuels without the possibility to fixate all the gas by natural means. This, especially when paired with the continued deforestation and increasing energy demand around the world, is one of the most challenging problems to solve in the foreseeable future. As these issues have become an increasing point of concern, national and international regulations and directives are pushing more and more towards sustainable solutions in the modern society.

A way to reduce the net emissions of CO_2 and still meet the energy demands is to force a shift in energy carriers towards renewable and more CO_2-neutral energy sources. In 2009, the European Union issued directive *2009/28/EC*, setting a goal for its member states to by the year 2020 lower their emissions of greenhouse gases by 20%, to increase their energy efficiency by 20% and to have at least 20% of their energy demands met by renewable energy sources [1-3]. This has created an incentive to develop and optimize renewable energy generation processes in order to meet the 2020 goals. Today, biomass and renewable wastes[1] are the top contributors to the generation of renewable energy in the EU, together accounting for about 67% of the total which also includes solar, hydro, geothermal and wind power, where the share of each energy carrier can be seen in Figure 1 below. In addition to being the largest contributors to renewable energy generation, the use of biomass and renewable wastes increased with 4,7% (nearly double the increase of the second fastest growing renewable; wind power) in between 2009 and 2011 in the EU, making it the fastest growing among the renewable energy carriers [5].

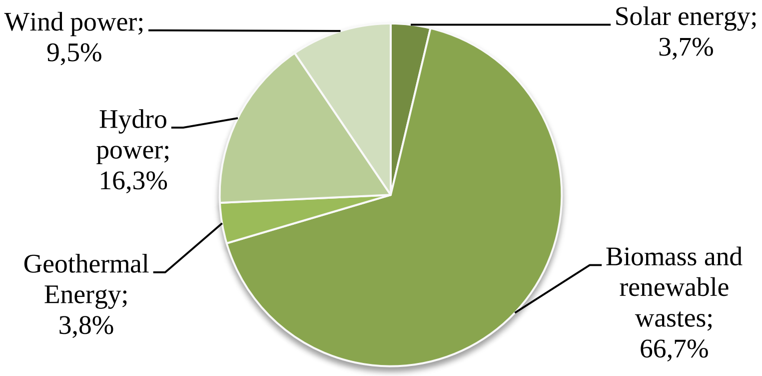

Figure 1: Share of renewable energy production in the EU by type (data from 2011, adapted from [5]).

---

[1] Contribution is based on heat content of both processed biomass e.g. biofuels and biogas, as well as unprocessed e.g. wood and municipal solid waste [4] Glossary:Biomass: Eurostat; [updated 29-11-2012; cited 2013 2/6]. Available from: http://epp.eurostat.ec.europa.eu/statistics_explained/index.php/Glossary:Biomass..

Over the course of the recent years, incineration has become the encouraged method for disposal of industrial and municipal solid waste (MSW) that cannot otherwise be reused or recycled. According to directive *2008/98/EC* [6] that entered into force in the EU in December 2008, incineration of MSW is considered as *energy recovery*, which in contrast to deposition in landfills is endorsed. This is mainly due to that the energy content in the waste can be utilised in heat and power generation while avoiding many problems associated with landfilling. This increases the energy efficiency as well, improving progress towards one of the 2020 goals. Even though incineration still isn't a common practise, merely accounting for 5,7% of the total waste treatment in the EU in 2010 [7], the amount of waste disposed through incineration has increased with 27,2% in between 2004 and 2010 [8]. Also, between 2008 and 2010, the amount of waste incinerated for energy recovery increased by 9,6% while incineration without energy recovery decreased with 10,7% [8]. This indicates that MSW based heat and power generation is a growing sector, which together with the increased use of biomass due to the 20% CO_2 emission reduction 2020 goal in the EU could increase the load on incineration-based plants.

2.2 Boilers

The heat content in biomass can be made available for practical use in three general ways, namely by thermochemical, biochemical and thermal processes [9]. In the thermo- and biochemical routes, the biomass is converted to various biogases and –liquids that are used as fuels in several different combustion processes that occur in a later stage of the energy generation procedure. The thermal process, commonly known as combustion, utilises raw, solid biomass that in contrast to the thermo- and biochemical techniques has not been significantly processed beforehand.

The combustion of solid biomass to generate heat and power is performed in a facility commonly referred to as a *boiler*. In a boiler, the high heat capacity of water is not only utilised to transport the energy to a turbine in the form of high pressure steam, but it is also used to harness the heat of condensation to warm various process streams such as district heating. A typical boiler consists of some general parts: Furnace, fuel delivery system, various heat exchangers (superheater, economizer and preheater, for instance), steam drum, turbine, flue gas cleaning systems, particle filters and a smokestack, some of which can be seen in Figure 2 below [10]. The walls of the furnace are commonly lined with tubes cooled by water, thus forming a so-called *waterwall* which acts as a single large heat exchanger.

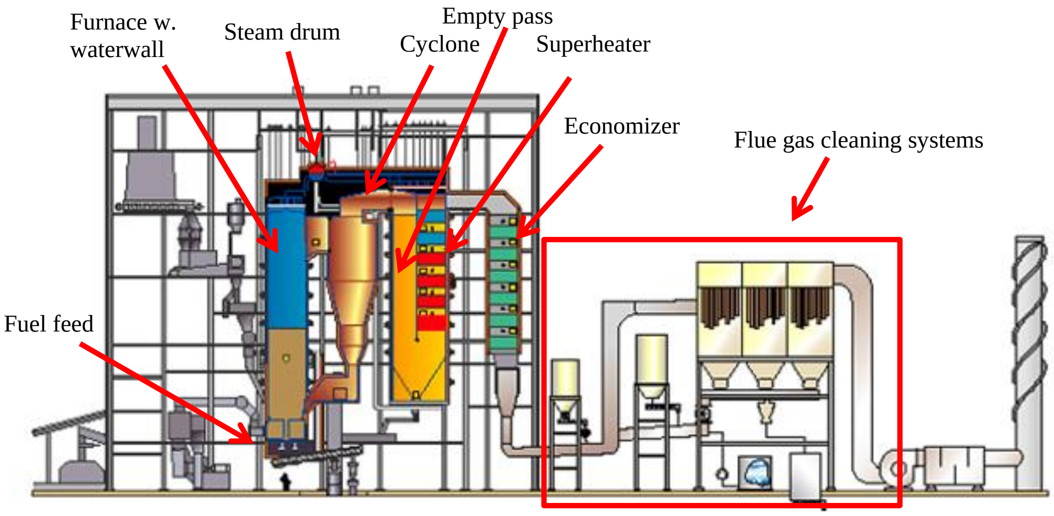

Figure 2: Typical waste fired circulating fluidised bed boiler and some of its main components.

Since a boiler is a fairly sizeable structure with large heat exchanging areas, the temperature is not uniform throughout its different parts. The hottest part of the boiler is the furnace, which counterintuitively does not produce the hottest water or steam streams in the plant. The hottest streams are produced in the different superheaters where the saturated steam becomes superheated to as high temperatures as possible in order to maximize efficiency. Some typical temperatures in various parts of a boiler are presented in Table 1 below [10].

Table 1: Typical temperatures in a waste fired circulating fluidised bed boiler.

Boiler part	Max gas temperature (°C)	Max steam or water temperature (°C)	Tube surface temperature (°C)
Furnace/waterwall	900	290	315
Empty pass	850	290	298
Tertiary superheater	900	470	520
Boiler bank	650	290	295
Secondary superheater gas inlet	630	400	360
Secondary superheater gas outlet	500	340	415
Primary superheater gas inlet	500	370	380
Primary superheater gas outlet	440	290	300
Boiler bank	440	290	
Economiser	350	240	

There are a number of configurations available for the waste fired boilers, where the most distinct difference lies in the furnace type. Depending on the type, the furnace can operate in different ways with different grate firing and fluidised bed combustion modes. During grate firing, the fuel is slowly transported on a conveyor belt into various firing zones before the actual combustion occurs. This makes grate firing a suitable process for mainly coarser fuels as the different zones allow for drying and gasification of the fuel in order to ensure an effective incineration. The fluidised bed boiler on the other hand, such as the one illustrated in Figure 2, suspends the fuel in an inert medium such as sand which then is fluidised by pumping gas through the bed, which allows for good heat transfer to the fuel as well as for in-line emission control of e.g. sulfur, which could be important issues to solve for some fuels.

As the fluidized bed combustion and grate firing processes have their different advantages and disadvantages, biomass and MSW are incinerated in both types of furnaces.

2.3 Biomass and MSW

Biomass is a collective term for both non-fossil biodegradable wastes as well as for energy crops that are solely grown to be used as fuel. This broad definition can at times be problematic due to the difference in physical and chemical properties between different kinds of biomass, which is why it is important to keep in mind that biomass is not a homogeneous classification. The term biodegradable waste can in the same fashion be as ambiguous since it is highly dependent on how the life-cycle boundaries are set. The European commission has defined biodegradable waste as *"...garden and park waste, food and kitchen waste from households, restaurants, caterers and retail premises, and comparable waste from food processing plants."* [11], which does not include wood and crop residues among others that some authors consider being biomass. In this work, the term *biodegradeable waste* will follow the definition set by the European commission as well as with the additional definition provided by Yin et al. [12], which further adds wood and crop materials as well as industrial and MSW of plant origin.

Since the net emissions of CO_2 are theoretically zero from incineration biomass as fuel due to the fixation of CO_2 by plants, cultivation of certain crops for the sole purpose of using them as fuel is an attractive renewable solution. These so called energy crops are often either wood crops or straws, both of which having a fast growth rate in order to ensure a continuous supply of fuel. Besides from the obvious advantage of being CO_2-neutral, firing biomass instead of landfilling it prevents formation of another greenhouse gas, CH_4, which is even more potent than CO_2. Other advantages of using biomass as fuel include lower SO_2 emissions due to inherently low S content and reduction of NO formation during combustion (both in comparison with fossil fuels) as well as prevention of contamination associated with landfilling of biomass [12].

MSW is by definition an even more broad term than biomass: The U.S. Environmental Protection Agency classifies garbage, sludge, materials resulting from industrial and commercial operations as well as from community activities, among others, as MSW [13]. Due to this, MSW consists of all kinds of wastes which makes the chemical content extremely varied and complex. Table 2 below displays the average composition of Swedish MSW and some types of biomass, data from [14-16]. As can be seen in Table 2, the composition of MSW and different kinds of biomass differs slightly. Because biomass composition varies with its type, averages for four different kinds of biomass have been added to the table for the sake of comparison: Wood, agricultural residue, grass and straw. To account for more kinds of biomass, an average for a broad spectrum of analysed biomasses has also been added to the table. It is important to note that Cl, which has been widely accepted to play a large role in boiler corrosion, is always present. Furthermore, the alkali content in both MSW and biomass is fairly high.

Table 2: Elemental composition of MSW and various kinds of biomass.

	MSW, wt% in dry fuel	**Biomass, dry and ash-free, Cl content listed as additional content**				
Fuel / **Species**	Waste	Wood	Agricultural residue	Grasses	Straws	All varieties (average)
Ash	19,2	n.a.	n.a.	n.a.	n.a.	n.a.
C	46,4	52,1	49,9	49,2	49,4	51,3
H	6,2	6,2	6,2	6,1	6,1	6,3
S	0,2	0,08	0,15	0,13	0,15	0,19
N	1,3	0,4	1,2	0,9	1,2	1,2
O	26	41,2	42,6	43,7	43,2	41
Cl	0,7	0,02	0,2	0,21	0,41	0,17
Metals	mg/kg dry fuel	Approximate alkali metal content				
Al	10920					
Ca	27516					
Cu	220					
Fe	5082					
K	4333	Medium	High	High	High	No data
Na	9217	Medium	High	No data	No data	No data
Pb	54					
Zn	452					

Even though waste prevention, reuse and recycling are more desired pathways to deal with waste, incineration is preferred over landfilling [6, 17]. As this might be seen as a blessing for the energy industry, it comes with a cost; some of the different characteristic chemical compounds in biomass and MSW can be linked to accelerated high temperature corrosion in boilers where these kinds of materials are incinerated. A challenge thus arises for the industry to meet the growing energy demands while at the same time coping with the environmental and political pressure to increase the use of biomass.

2.4 Impact on corrosion in boilers

The main problem with the accelerated high temperature corrosion in boilers is that steam temperature and pressure must be significantly reduced in order to prevent severe damage to different parts of the boiler. This however limits the efficiency of the plant by lowering the electrical output from the steam turbine, as well as the overall heat output of the plant. In addition to decreased efficiency, the corrosion creates the need for costly maintenance shutdowns in order to prevent damage to the boiler.. The main parts that are affected by the increased corrosion are most importantly the various heat exchangers, namely the water wall tubes, superheaters, the economizer and the preheater but also other metallic components that are in contact with the flue gas.

In the initial stage of the corrosion process on the heat exchanging surfaces, inorganic vapours and small fly ash particles combine to form an even, sticky deposit all over the surface. In the second stage, larger fly ash particles adhere to this first layer, thus effectively building up a second deposit. In addition to the ash, inorganic salts may stick to this second layer through condensation of salt vapours, which acts as a binder for the ash particles. In this way, a continuously thicker deposit consisting of ash and various condensed salts is formed. This second layer is mainly present on the windward side of the affected surfaces, which can lead to an uneven deposit distribution, depending on the geometry of the affected surface [12]. The deposit is schematically illustrated in Figure 3 below (adapted from [12]).

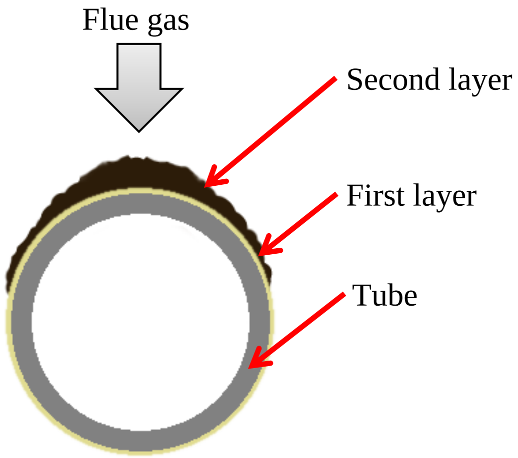

Figure 3: Cross section of a typical waterwall tube with deposit.

Due to the wide range of inorganic compounds that are present during the combustion process, a wide range of salt mixtures may condense on to the deposit and form low melting point *eutectic systems*. A eutectic system is a system whose constituent components have limited solubilities in each other while in the solid state. A specific composition, the *eutectic composition*, is characterized by having the lowest melting temperature of all possible mixtures that form a homogeneous melt consisting of all the constituent components in the system. This temperature is known as the *eutectic temperature*, and if the liquid solution is slowly cooled from this temperature, a solid solution of the components is formed [18]. These low melting point eutectics are suspected to be linked to accelerated high temperature corrosion through mechanisms that will be described later in this work. Some common eutectic systems and their respective melting points relevant in this work that can be present in boilers are presented in Table 3 [19-21] below:

Table 3: Melting points of some salts and eutectic systems normally found in biomass and MSW fired boilers.

System	Melting/eutectic temperature (°C)
NaCl	801
KCl	772
$ZnCl_2$	318
$FeCl_2$	677
$FeCl_3$	303
NaCl-KCl	657
NaCl-$FeCl_2$	370-374
NaCl-$FeCl_3$	151
NaCl-$ZnCl_2$	262
KCl-$FeCl_2$	340-393
KCl-$FeCl_3$	202
KCl-$ZnCl_2$	230
$ZnCl_2$-$FeCl_3$	200

Two of the eutectic systems presented in Table 3 are of special interest in this work, namely NaCl-$ZnCl_2$ and KCl-$ZnCl_2$. The reason for this is that the alkali, zinc and chlorine are present in moderate to high concentrations in MSW and biomass as can be seen in Table 2. Formation of the systems containing $FeCl_2$ and $FeCl_3$ is also possible, however the Fe chlorides are very volatile and thus the $ZnCl_2$-containing systems take precedence in this work as these are more stable. The phase diagrams of the systems NaCl-$ZnCl_2$ and KCl-$ZnCl_2$ are presented in Figure 4 and Figure 5 below.

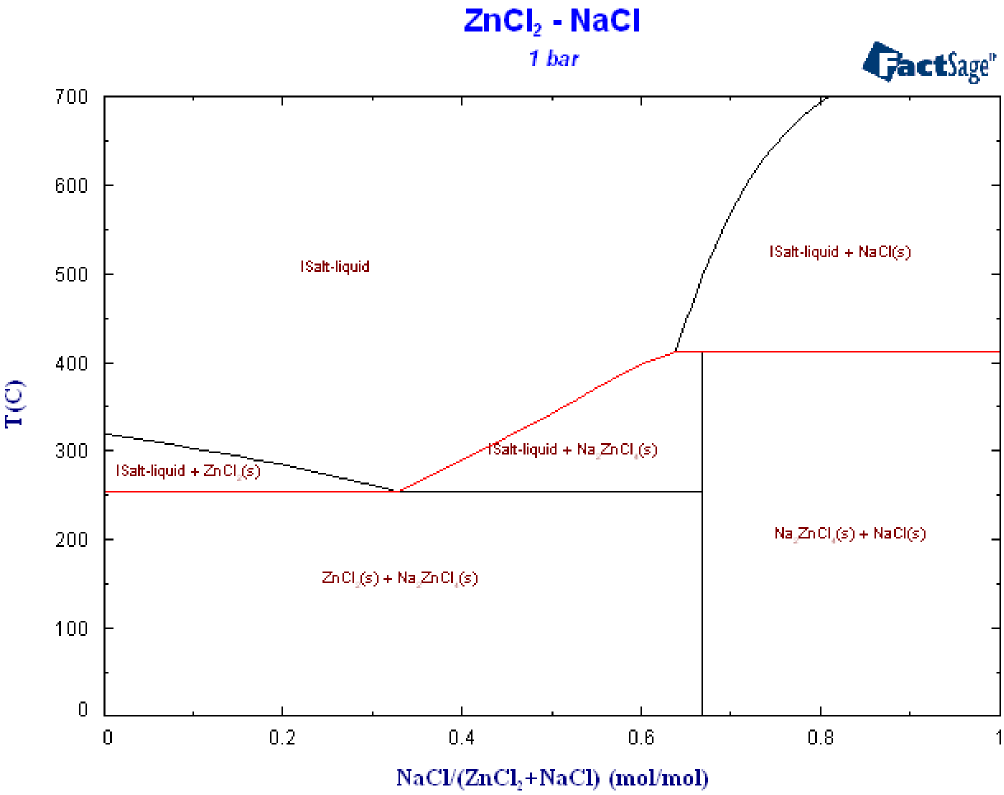

Figure 4: Phase diagram for the system NaCl-$ZnCl_2$ at 1 bar.

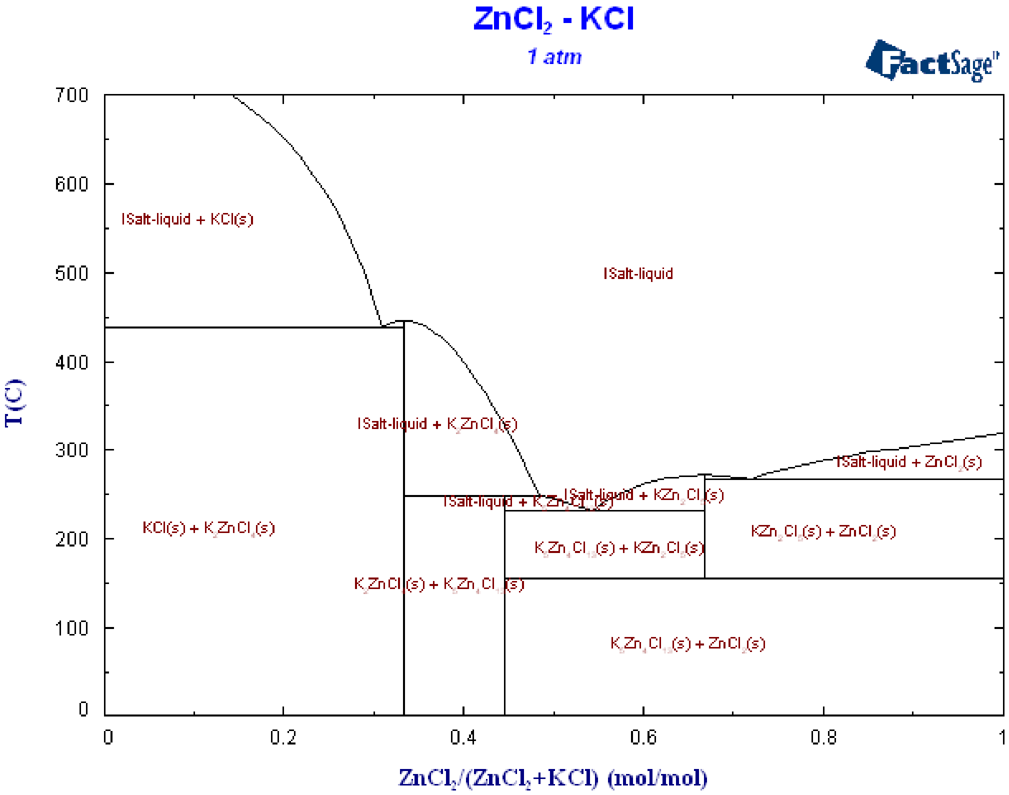

Figure 5: Phase diagram for the system KCl-$ZnCl_2$ at 1 atm.

As can be observed in Figure 4 and Figure 5, the melting point of the eutectic mixture is highly dependent on its composition, which is important to take into consideration when comparing different mixtures from a corrosion point of view. This is mainly due to that the mechanisms of high temperature corrosion are dependent on which state the corrosive species are in, which will be further explained later in this work. When examining the phase diagrams, three types of areas are visible: A salt-liquid which consists of a homogeneous melt, a salt-liquid together with a solid solution, and finally a solid solution together with either a pure salt or another solid solution. Evidently, salt melts can exist both as homogeneous melts as well as partial melts together with a solid phase present.

Today, alkali chloride induced high temperature corrosion can be mitigated in several ways in biomass and MSW fired boilers, other than decreasing the steam temperature. Various additives, such as ammonium sulphate, can be employed in order to affect the physical and chemical factors accelerating the corrosion such as raising melting temperatures and preventing corrosive species to form. Co-firing with coal or peat is also an alternative way to decrease the extent of the corrosion. Use of alloys and coatings with increased corrosion resistance are additional ways to deal with corrosion, but may however be costly to implement [12, 22].

2.5 Steel grades

As the composition of a steel has a direct effect on its chemical and physical properties, it is important to be aware of how the different alloying elements affect the steel in order to pick the right material for a certain application. Since the environment in a biomass and waste fired boiler can be fairly corrosive as can be seen in Table 2, a high corrosion resistance is required in certain parts of the boiler. The furnace, empty pass and the superheaters all have relatively high tube surface temperatures as can be seen in Table 1 which places a demand on the tube steel properties in those components. Usually, an *austenitic* (face centered cubic crystalline structured) stainless steel or a high alloyed iron based steel is used for those applications. These more resilient steels are however expensive and still suffer from corrosion attacks despite their higher corrosion resistance. Much scientific effort has therefore been made to see if less expensive low-alloyed steels can be used instead while keeping the corrosion rate at the same levels as for the more expensive steels.

The main alloying component that provides corrosion protection in most steels where Fe is the major component is usually Cr. By forming a thin, adherent and continuous oxide, Cr_2O_3, at the metal surface the oxidation of Fe can be avoided. For steels with Cr content below 3%, no protective Cr_2O_3 can form in sufficient amounts. These steels are known as *low alloyed* steels and the main protective phase that is formed on these steels is Fe_2O_3. Three different low alloyed steels are presented in Table 4 as well as one austenitic stainless steel and one high alloyed stainless steel for comparison [23-27].

Table 4: Composition of some low alloyed, austenitic and high alloyed Fe based steels, wt%.

	Low alloyed			Austenitic stainless	High alloyed Fe based
Element	**T22**	**16Mo3**	**13CrMo44**	**304L**	**Sanicro 28**
C	≤ 0,15	0,12 – 0,2	0,14	≤0,03	≤0,020
Cr	1,90–2,60	0,3	0,98	18,0-20,0	27
Mo	0,87–1,13	0,25 – 0,35	0,6	-	3,5
Mn	0,30–0,60	0,4 – 0,9	0,55	≤2,00	≤2,0
Si	≤ 0,50	0,35	≤0,4	≤0,75	≤0,6
P	-	0,025	-	≤0,045	≤0,025
S	-	0,01	-	≤0,030	≤0,015
Ni	-	0,3	-	8,0-12,0	31
Cu	-	0,3	≤0,3	-	1,0
Fe	Balance	Balance	Balance	Balance	Balance

In this work, the steel investigated is T22. This steel, also known as 2¼Cr-1Mo or 10CrMo9-10, is a low-alloyed carbon steel which is fairly cheap in comparison to the austenitic stainless and high alloyed Fe based steels. It is thought that T22 could replace some of the more expensive steels used in biomass and waste fired boilers, like 304L or Sanicro 28 for instance, if the extent of corrosion by chlorinated species would turn out to be in the same magnitude.

As a good rule of thumb for corrosion resistance in steels states that a higher Cr/Fe ratio gives better resistance, the T22 steel is obviously not as good as 304L or Sanicro 28 when comparing the Cr-content in Table 4 [14]. Therefore, the Fe_2O_3 layer that forms on T22 needs to have a number of features which are shared among the good, protective oxides. These characteristics and how they affect the oxidation of the metal are presented in the next section.

3 Metal oxidation theory

3.1 The metal oxidation process

The process of high temperature oxidation by oxygen on a metal begins with an initial adsorption of oxygen on to the surface. High temperature oxidation involving water or carbon dioxide is also possible; however emphasis will be put on oxygen in this section for the sake of relevancy. Once adsorbed, the oxygen reacts with the metal, resulting in the formation of a metal oxide [28]. This process can in general be described with the following chemical reaction with the basis of one mole oxygen:

$$\left(\frac{2x}{y}\right) M + O_2 \rightarrow \left(\frac{2}{y}\right) M_x O_y \qquad (1)$$

This reaction does not take place uniformly across the metal surface, but occurs spotwise followed by oxide nucleation and lateral growth until an oxide film that covers the entire metal surface has been formed. Once formed, the oxide film can be either protective or nonprotective depending on its stability. In general, in order to minimize the oxidation rate, the oxide film should have the following properties [28]:

- High adherence
- High melting point
- Low vapour pressure
- Low difference in coefficient of thermal expansion between metal and oxide
- High temperature plasticity
- Low electrical conductivity
- Low diffusion coefficients

High adherence prevents breakaway of the oxide film and a high melting point prevents the film to melt and become more reactive. Low vapour pressure ensures that the film does not evaporate and a small difference in coefficient of thermal expansion between the parent metal and the oxide avoids mechanical stress in the oxide film. Low electrical conductivity and diffusion coefficients for metal and oxide ions lowers the reaction rates of the chemical processes involved in the corrosion [28].

Evidently, a nonprotective film should lack these characteristics, which explains the case where the corrosion continues: After formation of an oxide film, the film grows either outwards through diffusion of metal ions via the film to the oxide/gas interface or inwards through diffusion of oxide ions across the oxide to the metal/oxide interface. The reactions associated with corrosion occur at these interfaces, which causes the oxide layer to grow. Low adherence, high vapour pressure, large difference in coefficient of thermal expansion and low temperature plasticity can cause various defects such as microcracks, pores and cavities to form, further facilitating the growth of the oxide layer. As the nonprotective oxide layer grows, the microcracks formed also grow into macrocracks, thus opening up new pathways for oxygen diffusion through the oxide, which increases the oxidation rate [28]. This growth may also increase the mechanical stresses in the oxide to the point that the oxide layer begins to fall off; this process is known as *spallation*. The oxidation process is summarized graphically in Figure 6, as adapted from [28].

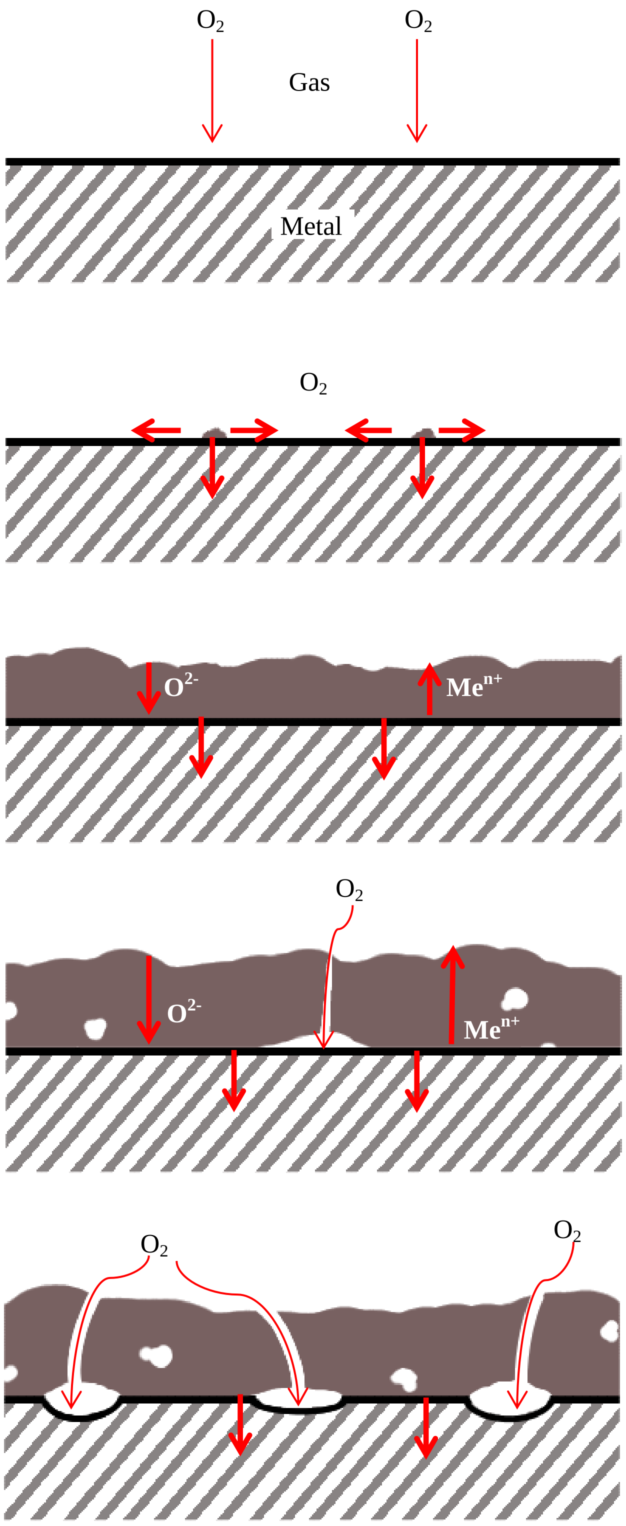

Adsorption of O_2 at metal surface and

Oxide nucleation and

Oxide film inward and outward growth

Formation of microcracks and cavities

Formation of macrocracks

Figure 6: The various stages of metal oxidation: Oxygen adsorption at the metal surface promotes growth of oxide particles followed by nucleation. As the oxide particles nucleate, they finally form a continuous oxide film which continues to grow. Microcracks and cavities are eventually formed, which finally lead to formation of macrocracks.

3.2 Thermodynamics of oxidation

In order to predict whether the chemical reactions that are associated with the corrosion are possible, thermodynamic calculations can be performed on the systems of interest. Since a spontaneous chemical reaction has a negative change in Gibbs free energy, $\Delta G°$, the changes in enthalpy and entropy coupled with knowledge of the temperature can easily predict whether a corrosive chemical reaction is spontaneously possible to occur [28]:

$$\Delta G° = \Delta H° - T\Delta S° \tag{2}$$

Another expression for $\Delta G°$ can be derived by examining the case when reaction (1) is at equilibrium [29]: The equilibrium constant K_a in a mixture of compounds is defined as

$$K_a = \prod \left[\frac{\hat{f}_i}{f°_i}\right]^{v_i} \tag{3}$$

where $\hat{f}_i$ is the fugacity of component i in the mixture, $f°_i$ is the fugacity of component i in the standard state and v_i the reaction coordinate of component i [30]. If the standard state is chosen as an ideal gas at 1 atm, $f°$ will become equal to the pressure P of the system i.e. unity. The fugacities of the solid components M and M_xO_y will also by definition become unity, since the activity of a pure, solid component is always 1 [30]. Since the only gas participating in reaction (2) is oxygen, the pressure of the system will be equal to the partial pressure of oxygen, P_{O_2}. This simplifies equation (3) for reaction (1) to

$$K_a = \frac{1}{P_{O_2}} \tag{4}$$

The Gibbs free energy of reaction for reaction (1) at constant pressure will therefore become

$$\Delta G_r = \Delta G° + RTln\, K_a = \Delta G° + RTln \frac{1}{P_{O_2}} \tag{5}$$

where R is the ideal gas constant and T is the temperature in Kelvin. Since ΔG_r is zero at equilibrium, this yields

$$\Delta G° = RT \ln P_{O_2} \tag{6}$$

As the enthalpy $\Delta H°$ and entropy $\Delta S°$ in equation both are constant, a plot of equation (2) with $\Delta G°$ versus T gives a straight line with a specific slope that alters when a phase change is encountered. If equations (2) and (4) are combined, a so called *Ellingham diagram* which couples temperature, gas pressure and Gibbs free energy to specific reactions can be plotted [29]. As stated in the beginning of this section, high temperature corrosion in steam and CO_2 is also possible, and a similar derivation for these gases can be performed in order to express the Gibbs free energy as a function of temperature and pressure. Combination of diagrams for oxygen, steam and carbon dioxide yields the classical Ellingham diagram, which has an axis with partial pressure of oxygen as well as axes with CO/CO_2 and H_2/H_2O ratios [28]. The Ellingham diagram can be used to predict how an alloy will corrode in a specific environment and can be seen in Figure 7 below as adapted from [14].

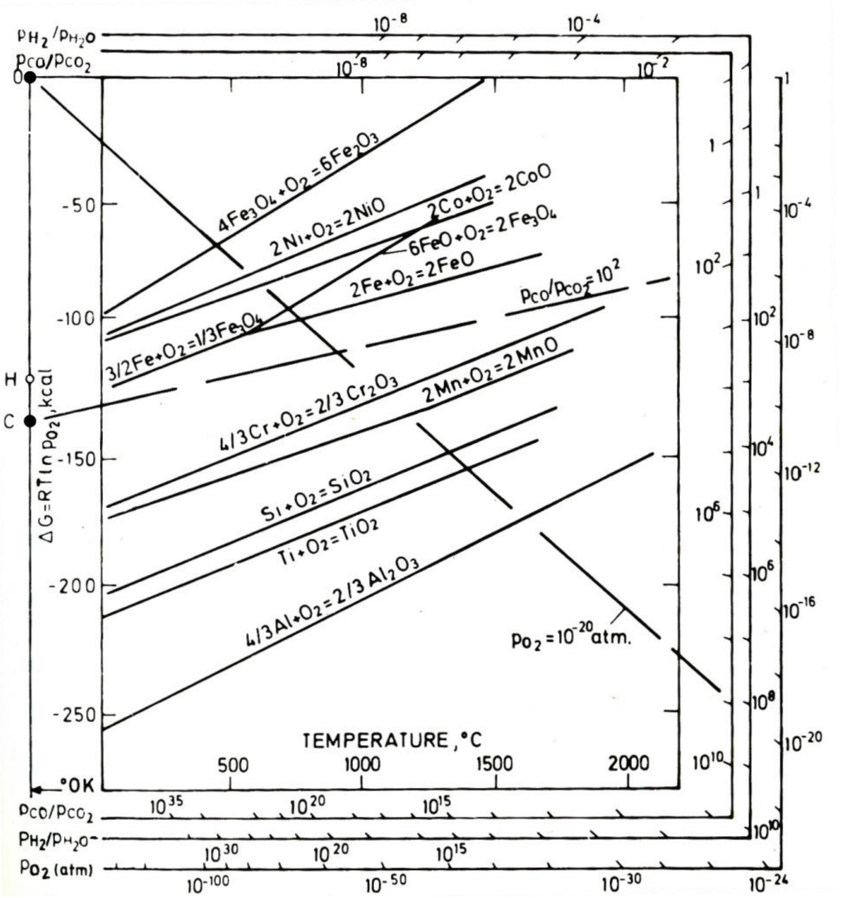

Figure 7: A typical Ellingham diagram for some various metals.

A large advantage with the Ellingham diagram is that determination of oxide stability in an alloy quickly can be determined. Since a lower $\Delta G°$ for a reaction tells that the product is more stable than a product of a reaction with higher $\Delta G°$, the lower a plot of $\Delta G°$ versus T is located in the diagram, the more thermodynamically stable the corresponding oxide is [29]. However, as with thermodynamics in general, neither the Ellingham diagram nor the underlying thermodynamic equations can predict the rate of corrosion. A review of the kinetic aspects of high temperature corrosion is therefore crucial.

3.3 Kinetics of oxidation

One of the major factors that decide whether a metal oxidation is corrosive or not is the rate of oxide formation: Depending of the rate, the properties of the oxide can range from nonprotective, temporarily protective to protective, where the kinetics of its formation can be described with a rate law. The most common way to determine the rate law of an oxidative process is to plot the mass gained through oxidation versus exposure time, usually referred to as a *mass gain curve*. The oxidative rate laws that are most often encountered are named after their appearance in the mass gain diagram: Parabolic, logarithmic and linear [28].

In many cases of metal oxidation, the parabolic rate law describes the kinetics of oxide growth in an accurate way. The parabolic rate law states that the square of the oxide thickness is proportional to the exposure time:

$$x^2 = k_p t \qquad (7)$$

where x is the oxide thickness, k_p is the parabolic rate constant and t the exposure time [28]. The rate constant k_p is like all other chemical rate constants affected by the temperature according to the Arrhenius law:

$$k_p = k_o e^{-Ea/RT} \qquad (8)$$

where k_o is a constant, E_a the activation energy, R is the gas constant and T is the temperature. To be more precise, k_o is dependent on the gas pressure in different ways depending on the metal oxide in question and on the composition of the oxide itself [29]. Furthermore, k_p is also directly dependent on the partial pressure of oxygen [28]. The parabolic rate law describes the oxide growth to be fast in the beginning of the oxidation, followed by a decrease in oxidation rate as the exposure time increases. This decrease in oxidation rate with time can be attributed to an increased difficulty for ions and molecules to move through the oxide layer as it grows thicker, thereby making the oxidation reaction diffusion controlled.

For oxidation of thin films at temperatures below 300-400°C, the logarithmic rate law is generally obeyed:

$$x = k_a \log(k_b t + 1) \qquad (9)$$

where k_a and k_b are integration constants. Due to its logarithmic nature, oxidation kinetics following this rate law have a high initial rate which levels of quickly as the oxidation proceeds. As the oxide is comprised of a thin film, diffusion of oxygen is not a rate controlling factor; instead, cation migration and tunnelling or thermal emission of electrons have all been suggested to control the rate. None of these theories have however been definitely accepted as an adequate explanation for what controls the rate of logarithmic oxidation [28].

For conditions where the oxidative power is low i.e. low partial pressures of oxygen and in CO/CO_2- mixtures, the oxidation may be illustrated with the linear rate law:

$$x = k_l t \qquad (10)$$

where k_l is the linear rate constant. Not surprisingly, the linear rate law will yield a straight slope in the mass gain diagram, which has a stark contrast to the parabolic and logarithmic rate law curves, as it does not level off with time [28]. This suggests that no protective scale forms as the oxidation continues, and even that the oxide becomes highly porous, melts, spalls or evaporates [29]. As the oxide that is formed is nonprotective, diffusion through the oxide layer is no longer hindered, and the oxidation rate becomes controlled by the reaction rate at the phase boundary between an inner, protective oxide with constant thickness and an outer, nonprotective oxide that continuously grows [28]. To visualize the difference in mass gain versus time the parabolic, logarithmic and linear rate laws yield, the three rate laws are plotted in Figure 8 below.

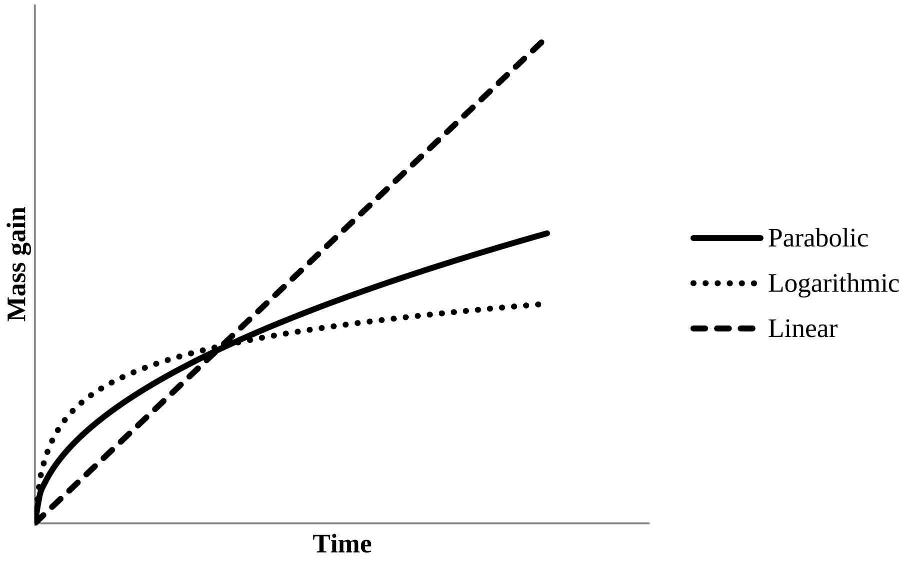

Figure 8: Visualization of the parabolic, logarithmic and linear rate laws in a single mass gain diagram.

In certain environments, combinations of the rate laws may arise. One such instance is when a parabolic oxidation transforms to a linear oxidation which occurs when the oxide layer suddenly becomes increasingly permeable for various species, and thus increases the diffusion rate [28]. When this ensues, the parabolic mass gain curve suddenly begins to follow the linear rate law which makes the mass gain take off and increase very rapidly. This phenomenon is visualised in the mass gain diagram in Figure 9 below.

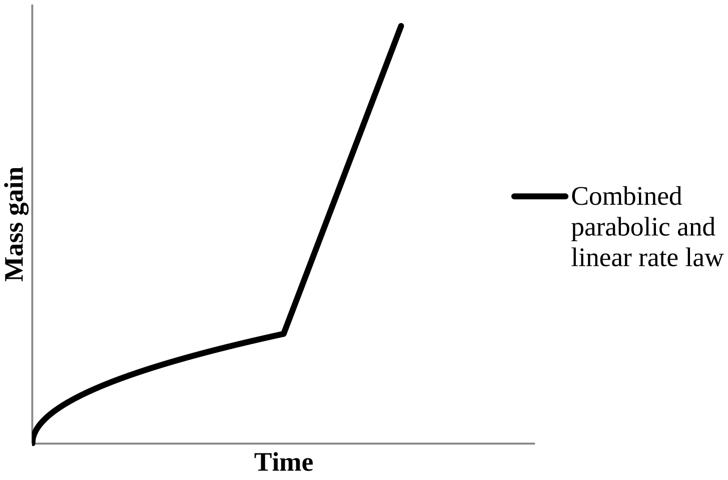

Figure 9: Typical transition from parabolic to linear kinetics.

A phenomenon known as *breakaway* may happen when a protective oxide fails at an accelerating number of sites. As the number of sites grows the kinetics change and may even transition into a cubic rate law, which has the exponent 3 instead of 2 as in the parabolic rate law. As time passes, several such rate law transitions may occur, leading to an increasingly linear appearance of the mass gain curve [28]. This phenomenon is illustrated in the mass gain plot in Figure 10 below:

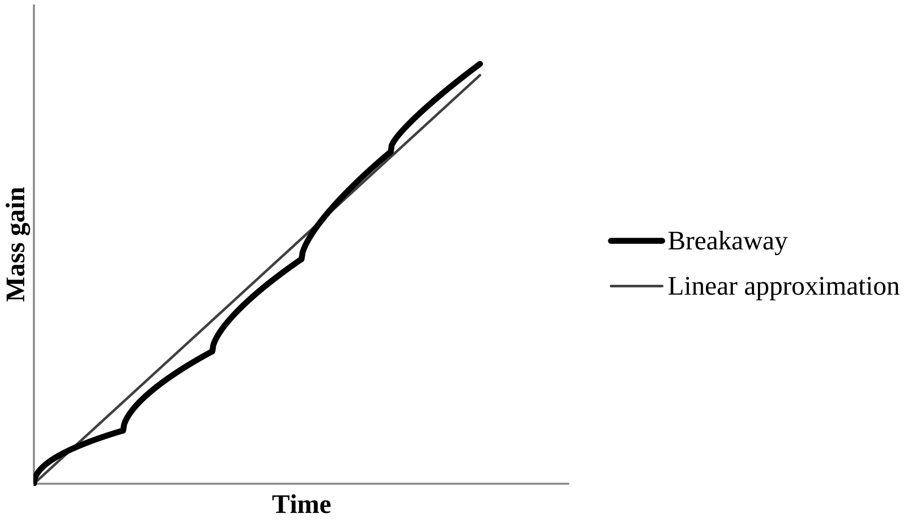

Figure 10: Breakaway corrosion depicted in a mass gain diagram; a series of parabolic curves can eventually be approximated with a linear rate law.

4 Chlorine induced corrosion

The relatively large amount of chloride salts present in biomass fired boilers enable various ways in which the corrosion can occur. The main issue with these salts are that they degrade the steel by facilitating the formation of a porous, nonprotective metal oxide layer [20]. This corrosion process is still not yet fully understood, however three different possible theories have been considered in this work: Corrosion induced by Cl_2 penetration into the steel (theory A) [20], oxide layer fluxing by low melting point chloride salt eutectics (theory B) [20, 31] and finally ionic diffusion in steel grain boundaries (theory C) [19].

Theory A, commonly referred to as *active oxidation*, suggests that Cl_2 diffuse through the protective oxide layer to the metal oxide-metal boundary, where they react with the alloying metals in the steel to form metal chlorides [32]. The Cl_2 is formed by reaction of chloride salts with either SO_2 or oxides in the metal scale, or by reaction of HCl with O_2. Apart from Cl_2, HCl can directly diffuse to the oxide-metal interface and also form metal chlorides in a similar fashion. As the metal chlorides form, their volatility makes them diffuse outward through the oxide layer towards the oxide-gas interface, a process that is further favoured by the high concentration of metal chloride at the metal oxide-metal interface [20, 33]. As the metal chlorides are stable in the absence of O_2, they continue to diffuse outward through the scale until the partial pressure of O_2 becomes higher near the surface. As O_2 becomes more abundant closer to the surface, the diffusing metal chlorides oxidise to form a porous, nonprotective metal oxide layer. This process releases Cl_2 that can diffuse back towards the metal oxide-metal interface through the newly formed loose oxide layer where it again reacts with the metal, thus creating a cycle [20, 33]. The active oxidation steps can be summarized with the following reactions:

$$M(s) + Cl_2(g) \rightarrow MCl_2(s)$$

$$MCl_2(s) \rightarrow MCl_2(g)$$

$$2MCl_2(g) + \frac{3}{2}O_2(g) \rightarrow M_2O_3(s) + 2Cl_2(g)$$

If the conditions are reducing, then the metal oxide covering the steel will be less prominent than in an oxidizing environment. In that case, the metal chlorides that are formed do not convert into oxides, but instead evaporate. Since the corrosion rate is largely dependent on evaporation rate, which in turn is affected by temperature and the gas flow rate, the evaporation of the metal chlorides will become increasingly destructive as the temperature rises and gas flow increases [20]. A drawback with theory A is that it does not explain why diffusion of Cl_2 through the scale is favoured while diffusion O_2 is not. This is remarkable since the molecular radius of Cl_2 is larger than that of O_2.

Theory B, on the other hand, proposes that certain chloride salts form low melting point eutectics which basically leach the Fe from the steel and subsequently facilitate its oxidation. These chloride salts are directly deposited on the scale, and may originate from the fuel being incinerated in the boiler. These chlorides form low melting point eutectics in the deposits, thus creating a liquid phase during heating that is in contact with the oxide layer of the steel [20, 31]. The presence of a liquid phase facilitates the degradation of the protective oxide layer by increasing the rate of the different processes associated with corrosion through an increase in ionic mobility. The considerably higher mobility of ions in the eutectic salt melt dramatically enhances the corrosion, which attains the characteristics of corrosion in the aqueous phase due to the high diffusivity in the salt melt. Further, dissolution of the protective oxides in the salt melt and reprecipitation at the gas-oxide interface also contributes to a higher corrosion rate [20, 29]. Notably for low alloyed steels, the conversion of protective Fe oxides to $FeCl_2$ in the oxide scale in the presence of molten salts is a key process that leads to enhanced corrosion [20, 31, 34]. This $FeCl_2$ can also form eutectics that have even lower melting points together with other chloride salts, most notably KCl or NaCl, and thus further accelerate the corrosion [34]. According to Viklund et al. metal chlorides are frequently encountered in the metal oxide-metal interface, and thus promoting diffusion of chlorides away from the interface due to concentration gradients [35]. As the partial pressure of O_2 increases closer to the surface, the $FeCl_2$ is oxidized to Fe oxides that form a porous, nonprotective scale on the steel just as described in theory A [31, 34].

For some salts however, there seems to be no need to form the low melting point eutectics due to their inherently low melting temperature in order to enable salt melt corrosion. $ZnCl_2$ is a good example which has been suspected by Bankiewicz et al. to cause melt-induced corrosion without other salts present in temperatures as low as 318°C [36]. It is however important to note that the presence of a salt melt does not rule out other corrosion mechanisms that may attack the steel simultaneously with the salt melt. For instance, other corrosive species like HCl may form, thus facilitating the corrosion. As many different salts can be present in their molten states during salt melt corrosion, the reactions governing the corrosion are not only to a large extent affected by the temperature, but also by the solubilities of the salts and the kind of metal oxides present on the steel [35].

Theory C is relatively young in comparison with theory A in particular, but gives a possible explanation to how chlorine can cause corrosion with an electrochemical mechanism. Initially, HCl and O_2 adsorb on to the steel oxide surface, followed by a dissociation of HCl into H^+ and Cl^- as well as a simultaneous reduction of O_2 into O^{2-}. Following this, the O^{2-} ions then react with the newly formed H^+, thus forming H_2O which evaporates. This reaction creates a negative charge deficit at the surface that is compensated by through migration of electrons from the steel surface to the oxide surface. These electrons are released through oxidation of the metals in the steel, effectively creating metal cations at the metal-oxide interface [19]. Due to high solubility and mobility in the oxide grain boundaries, the Cl^- ions migrate down through the oxide grain boundaries and form metal chlorides with metal ions encountered on the way. Apart from the Cl^- ions, the metal cations migrate through the grain boundaries as well, but this migration is instead directed outwards, in the opposite direction as the Cl^- ions. The rate of migration for the different ions varies, which results in that metal chlorides form at various depths in the oxide layer. As the metal chlorides that are formed are unstable in higher partial pressures of O_2, the metal chlorides close to the oxide-gas interface become oxidised into metal oxide and Cl_2, just as in theory A and B [19].

Accelerated corrosion attack around slag inclusions in the steel has been proposed to occur via the electrochemical mechanism presented in theory C, as the absence of oxide above slag inclusions at the steel surface provide easier access for the Cl^- ions along the slag inclusion rim. The accelerated corrosion rate produces nodular surface structures consisting of metal oxides and chlorides that completely cover the slag inclusions [19].

5 Analysis methods

5.1 SEM

The scanning electron microscope (SEM) is a common instrument used to examine the surface topography in the nanometre scale. Since the resolving power of a microscope is dependent on the wavelength of the electromagnetic radiation that is used to visualize an object, a shorter wavelength enables resolution of smaller objects. As the name implies, the electromagnetic radiation used in a SEM consists of electrons, which have a wavelength of 1-3 pm. As this wavelength is much smaller than that of visible light (400-700 nm), the SEM can reach magnification levels that are impossible to achieve with regular optical microscopy. This fact is widely exploited in various fields of science, where high temperature corrosion is one where it plays a very important role. The two main disadvantages with the SEM are that the specimen must be conducting in order to prevent local buildup of electrical charges and that the sample must be able to withstand very low pressures [37].

The SEM instrument consists of four major parts: An electron gun, a series of magnetic lenses, a detector and a vacuum system. The electron gun emits primary electrons (PE) towards the sample that is to be studied. In order to obtain good results, the electron beam should be as monochromatic as possible and the energy distribution of the electrons in the beam should be fairly even. As the beam propagates towards the sample, it is accelerated in an electric field applied by the instrument and focused by the series of magnetic lenses onto the section to be examined. As the electrons hit the sample, they penetrate the surface and lose some of their kinetic energy in the process. This energy is transferred to the outer shell electrons in the sample, and the gain is sufficient enough to allow some of them to be ejected from the sample, thus producing secondary electrons (SE) [37]. Furthermore, when some of the incoming primary electrons collide elastically with the sample atoms, they get scattered backwards toward the detector, yielding what is not surprisingly called backscattered electrons (BSE) [38]. The total volume of the sample that is affected by the primary electron beam is called the *interaction volume*, and has a pear-like shape as illustrated in Figure 11 below. The dimensions of the interaction volume depend on the acceleration voltage and on the material studied: A typical horizontal diameter at its widest cross section when studying steel is approximately 1 µm at an acceleration voltage of 20 kV. As shown in the figure, different kinds of information are gathered from different depths, which is important to remember when performing microscopy.

As the SE and BSE have different origins (the sample and the electron gun, respectively) and thus history of interaction with the sample, different information can be obtained by changing the detection mode for the detector. Since the SE are produced at the surface of the sample, they give information about the surface topography, while the BSE yield information about the composition of the sample due to their origin from scattering of PE below the sample surface [37]. The relative composition of the sample is possible to deduce due to the fact that the BSE scatter differently depending on the mass of the atom the electrons interact with, where a stronger backscattering is observed for heavy atoms. This enables the BSE detector to distinguish between areas of different chemical composition, which in practice means that the brighter an area is, the more heavy elements are present there [39].The interaction volume and some of the types of radiation produced in its different zones is illustrated in Figure 11 below as adapted from [19].

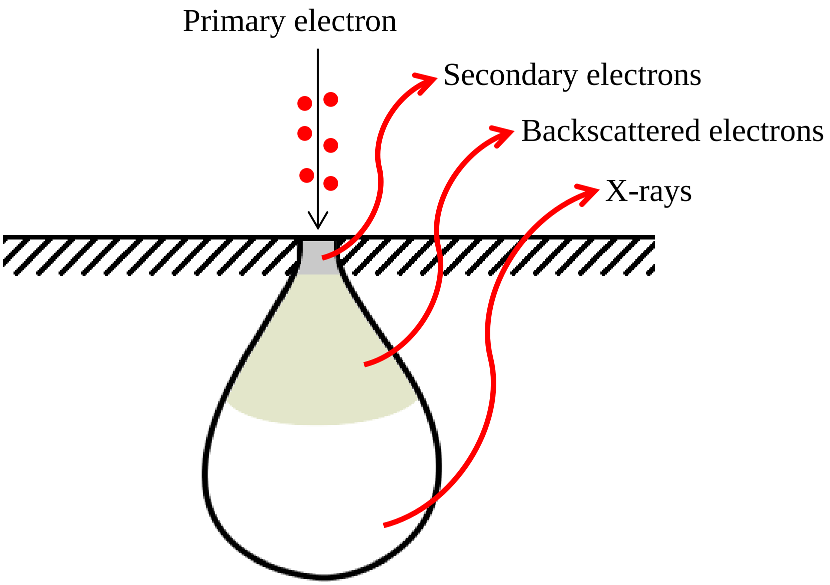

Figure 11: Schematic of the interaction volume and which kind of information is obtained from its various zones.

In order to prevent the electron beam from interacting with any atoms in the air, which would interfere with the imaging, the analysis must be performed in vacuum. Therefore, a sophisticated vacuum system is used in order to ensure as low pressures as possible during regular SEM operation [37]. However, in recent decades, environmental SEM (ESEM) has emerged as a new, useful technique for studies of specimens in atmosphere. With this technique, the requirement for high vacuum is no longer an issue, and pressures as high as 20 Torr can be present during analysis [39]. This feature enables the electronic microscopist to study living biological systems, vacuum-sensitive materials and, most importantly for the corrosion scientist, *in situ* chemical reactions [39].

5.2 EDX

By measuring emission of element-characteristic X-rays, the atomic composition of a sample can be determined. Energy Dispersive X-ray (EDX) is a technique that often accompanies SEM instruments due to several similarities in setup. The working principle of the EDX is that high-energy primary electrons strike the sample and eject previously unexcited electrons from the inner shells of the atoms in the specimen. This creates vacancies that are filled by electron transitions from shells with higher energy, which emits X-rays in the process. As the energy differences between different electron shells are unique from element to element, the X-rays formed are characteristic for every atomic structure. Thus, by scanning and measuring the emitted X-rays over the whole sample, an elemental map of the specimen can be obtained [37]. The process is illustrated schematically in Figure 12, as adapted from [19].

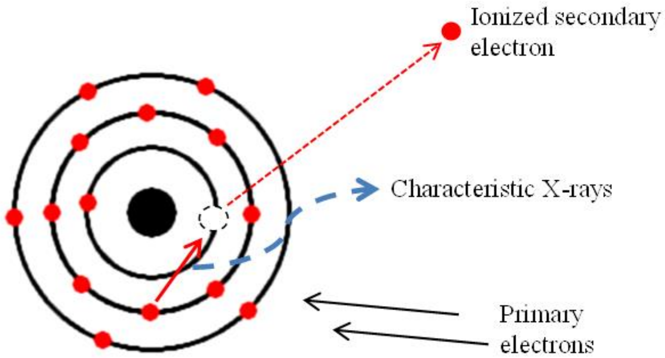

Figure 12: Emission of characteristic X-rays occurs when an inner shell electron is ejected due to bombardment of the atom by primary electrons and an outer shell electron transitions to the lower energy level in order to fill the empty gap.

5.3 XRD

Every material scatters electromagnetic radiation differently. In order for diffraction to occur in a crystalline solid, the distance between the lattice points has to be in the same order of magnitude as the wavelength of the incident electromagnetic radiation [40]. As X-rays have wavelengths in between 0,1-100 Å which is similar to the interatomic distance in a solid, this enables crystalline solids to diffract the X-rays in a specific manner, unique to the compound being studied [41]. The technique exploiting this scattering phenomenon is called X-ray diffraction (XRD), and is a common analysis method in the field of solid state chemistry. There are different types of X-ray diffractometers, but for the corrosion scientist, the powder diffractometer is especially useful because of the physical nature of the thin, often mixed oxide films covering an oxidized substrate. Thus, even though some parts of the following information can apply to other types of the instrument, emphasis will be put on powder XRD.

The powder XRD instrument consists of three general parts: An X-ray source, a sample holder and a detector [41]. The X-rays are generated in either an X-ray tube, a rotating metal anode or in a synchrotron. The generated radiation contains a whole spectrum, called *bremsstrahlung*, of X-rays with certain distinct peaks, called K_α and K_β, which can always be easily observed. These peaks have a specific wavelength that is unique and characteristic to the anode material, a phenomenon that is highly useful due to that monochromatic radiation is desired in the analysis. It is highly important that the incident radiation is monochromatic since the diffraction of the X-rays should produce an interference pattern [40]. In the most common case, the K_α-wavelength is selected for the X-rays [41]. When the X-rays irradiate the sample, the beam is diffracted through interaction with crystallites in the specimen, and the intensity of the diffracted beam is measured in the detector. In order to maximize the number of planar reflections from the sample, the sample holder may be rotated in order to irradiate the sample thoroughly. The X-ray source and detector need not to be fixed and may be mounted in a moveable way, so that they can move with respect to each other in order to enable irradiation of the sample at different incident angles during the analysis [40].

As the diffraction pattern that is generated upon irradiation of the sample by X-rays is produced through interference, the allowed reflections that arise from constructive interference are governed by a set of rules unique to every crystal system. The Bragg equation predicts at which angles the reflections from the different crystal planes produce constructive interference, and thus give rise to a response in the detector [41]:

$$n\lambda = 2d_{hkl}\sin\theta \tag{11}$$

where n is the order of diffraction, λ the wavelength of the incident radiation, d_{hkl} the interplanar spacing (d-spacing) between two neighbouring, parallel crystal planes and θ the angle between the incident X-rays and the crystal planes [41]. The diffraction of the X-rays by the atoms in the lattice is illustrated in Figure 13 below as adapted from [19]:

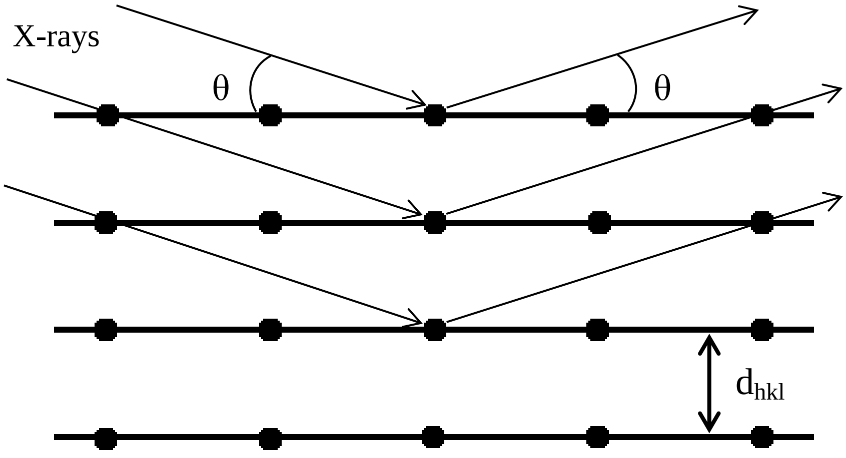

Figure 13: Diffraction of X-rays by the atomic lattice.

By varying θ, the penetration depth of the X-rays can be modified: A small θ gives greater surface sensitivity making it possible to probe the very top of the sample surface. This technique is commonly called grazing angle XRD and is highly useful in the cases where a thin surface film is to be analysed [42].

Since different crystal planes give rise to different reflections, identification of the structure of the unit cell becomes possible by associating each reflection to a set of Miller indices. Moreover, as translational symmetry elements such as screw axes and glide planes contribute to the systematic absences, the knowledge of which reflections that are allowed for more complex crystal systems further facilitate the calculation of the unit cell, and thus the identification of the sample contents [41].

The XRD analysis yields a plot where the reflection intensity is plotted as a function of the incident angle of the X-rays. This plot is called a diffractogram and is characteristic for every type of crystal structure and mixtures of these. As a sample may consist of multiple crystalline phases, the diffractogram can become complicated due to peak overlap which makes it difficult to calculate the unit cell [41]. Since an extensive database of reference diffractograms is available, identification of crystalline phases is instead done through fitting the plot obtained in the analysis with reference diffractograms from the database. This requires some prior knowledge or at least presumption of which elements might be present in the sample in order to obtain a limited selection of reference diffractograms to match with the one obtained in the analysis.

5.4 Ion chromatography

Even though EDX is qualitative in the sense that areas of samples can be analysed in terms of composition, performing EDX on the whole sample is time wise unrealistic. Coupled with the fact that XRD is mostly considered a qualitative technique even though it can be used as quantitatively, the three analytical techniques presented above are all employed for qualitative analysis in this work [43]. As a compliment, ion chromatography (IC) can successfully be used for quantification of various ionic species associated with high temperature corrosion.

The principle behind IC is that separation of different chemical species in a sample occurs through ion exchange followed by detection of each individual type of ion. In brief, a mobile phase carrying the sample and solvent moves through a stationary phase whilst both chemical and physical equilibrium processes occur which govern the retention times for the different ionic species in the sample. The mobile phase is washed through the stationary phase by the *eluent*, which consists of the solvent. This process is known as the *elution*. After passing through the stationary phase, the *eluate* that is consisting of the sample and eluent passes through a detector that quantifies the species in the sample. The retention time in the stationary phase, which in practise correlates to the extent of separation, is controlled by several factors, which range from the type of stationary phase used to the composition of the eluent, for instance [44].

A generic chromatography system consists of four main parts: Column, injection valve, pump and detector. Separation of the different sample species occurs in the column, which contains the stationary phase. This stationary phase interacts with the sample species, retarding their migration through the column to different extents. The nature of this interaction varies between different chromatography techniques. In ion chromatography, the stationary phase consists of a resin that is functionalised with charged groups that interact electrostatically with the ionic species in the sample. In order for the elution to continue, the column is washed with eluent, which washes the ionic species in the injected sample through the column. During this process, the eluent competes with the sample contents in terms of electrostatic interaction with the resin. Thus, species with low affinity for the stationary phase are eluted first, followed by species with increasingly higher affinity as more eluent is added to the column [44].

In order to ensure that the volume injected into the column is exact, an injection valve which has a fixed volume sample loop is necessary. Apart from ensuring that the concentration in the sample is correctly calculated, the fixed volume loop also guarantees reproducibility in between sample runs. The pump, which presses the mobile phase through the column, also plays a role in ensuring a high level of reproducibility by making sure that the pressure and therefore flow stays constant without any fluctuations [44].

After the different species in the sample have moved down the column and become separated into discrete bands, the flow directs the bands, one at a time, through a detector. In ion chromatography, the detector measures the conductivity of the eluate, which correlates to the concentration of ions. As the eluent has to have a higher ionic strength than the species in the sample in order to be able to wash the sample through the column, the high conductivity of the eluent can obstruct the sample signal in the detector. This can be remedied by attaching a suppressor column after the regular separator column that converts the species in the eluent to electrically neutral ones, such as pure H_2O, through ion exchange [44]. These converted species do not interfere with the conductivity detector and therefore allow the sample contents to be quantified.

In order to directly calculate the concentrations in the sample, a calibration curve must be constructed by using standard solutions with known concentrations of the species of interest. The obtained calibration curve then enables the computer to correlate the detector response to a concentration. Although the discrete bands that travel through the column contain just one species and eluent, they are not ideal in terms of distribution. Differences in path length through the ion-exchange resin, equilibration time and diffusion all contribute to band spreading, which makes the detector response look like a bell shaped peak instead of a discrete pulse [44]. In order to correctly determine the detector response, the area below each individual peak must be measured. To determine the order in which the sample species are eluted, the computer compares the sample chromatogram with the one obtained in the calibration run, where the elution times of the different ions are known. For the final quantification of the species in the sample, the computer compares the peak areas for each species in between the calibration curve and the sample run, and then calculates the concentration in the solution that was injected into the column.

6 Experimental

6.1 Sample preparation

The steel plate was cut into squares with approximate dimensions of 15x15x2 mm and a small hole (⌀: 1,5 mm) was drilled near one of the flat edges in order to facilitate easier handling. The sides of the samples were ground even with #1000 grit SiC paper to ensure a clean and facet-free surface. To polish the faces of the samples, the samples were mounted on a sample holder using pieces of self-adhesive discs and double-adhesive tape and first ground with #320 followed by #1000 grit SiC paper respectively. Following the grinding, the samples were polished with 9, 3 and 1 µm diamond size polishing paper. In between every grinding and polishing stage, the samples were rinsed with ethanol (99,5%). After grinding and polishing both faces, any glue residue on the sample was removed using cotton pads and acetone, followed by cleaning in an ultrasonic bath with acetone and ethanol respectively. Finally, the samples were checked for imperfections, weighed and stored in a desiccator.

6.2 Salt coating

To coat the sample faces with salt, solutions containing specific salts in a mixture of water and ethanol were prepared. As the concentration of salt in the solutions was known (0,05 mol/dm^3 with respect to Cl$^-$, 50/50 molar alkali/Zn ratio for mixtures), a micropipette was used to deposit the desired amount of solution, 50 µL, on to the each of the sample faces while simultaneously using a heat gun to evaporate the solvent. This yielded a salt deposit with a specific amount of salt. After coating, the samples were weighed to determine the exact amount of deposited salt and stored in resealable plastic bags in a desiccator.

6.3 Exposure

The samples were exposed in an electrically heated tube furnace in an environment with known gas composition. The furnace system consisted of a gas inlet, heater, borosilicate glass tube, gas humidifier and a bubble flask; the experimental setup is illustrated in Figure 14 below, as illustrated in [14]. The gas humidifier consisted of a water filled round-bottom flask connected to the gas inlet with a condenser attached on top. The condenser was connected to the gas outlet from the humidifier, and thus directly connected to the borosilicate glass tube. The bottom of the flask was placed in an electrically heated mantle. The temperature of the heating mantle was controlled with a temperature regulator connected to a thermocouple that was placed inside the round-bottom flask.

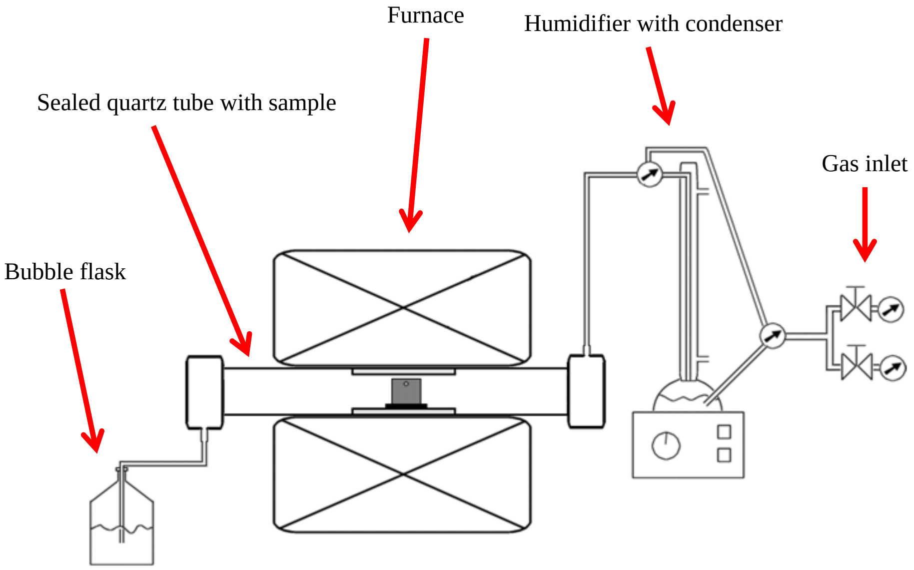

Figure 14: Schematic illustration of the furnace system used for the exposures.

Prior to exposure, the heater was set to the desired exposure temperature. When the temperature had stabilized, the gas flow was measured with a gas flow meter and adjusted to the desired levels, and the temperature in the exposure zone inside the borosilicate glass tube was measured using a thermocouple. The gas humidifier was then activated and set to provide a temperature of 76,2°C in the condenser.

The exposure conditions were as follows:

- Exposure temperature: 400°C
- Exposure time:
  - 1 hours: NaCl, NaCl/$ZnCl_2$ and KCl/$ZnCl_2$ systems respectively
  - 24 hours: All systems
  - 168 hours: NaCl, NaCl/$ZnCl_2$ and KCl/$ZnCl_2$ systems respectively
- Fixed 1000 mL/min gas flow:
  - 55% N_2
  - 40% H_2O
  - 5% O_2
- Mass salt/mixture per sample area: 0,1 mg/cm^2

The borosilicate tube was opened, and the samples to be exposed were mounted in alumina crucibles which were subsequently placed in the heating zone of the furnace. The glass tube was then closed and the samples were allowed to sit for five minutes to reach exposure temperature before the gas was allowed to pass through the tube, which also marked the start of the exposure. After the samples had been exposed for the desired period of time, the gas flow was closed and the samples were removed from the glass tube and placed in a desiccator to cool down. When the samples had cooled down, they were weighed and stored in resealable plastic bags.

7 Results and discussion

7.1 Gravimetry

The weight change of the samples after exposure was recorded and compared with existing references. The results from this gravimetric analysis are presented in Figure 15 below.

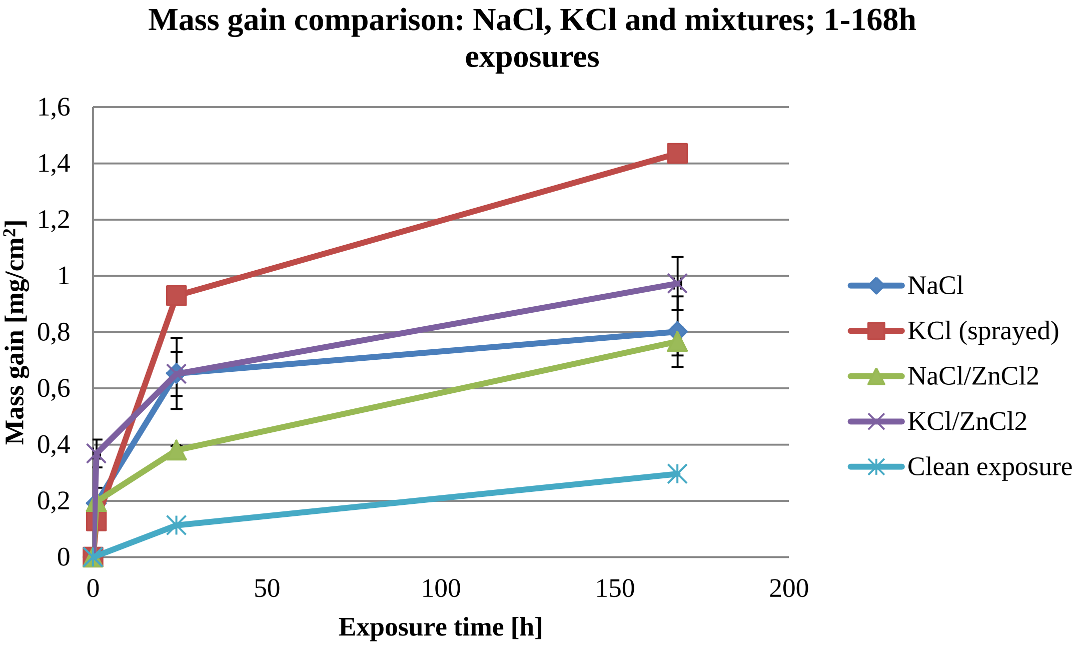

Figure 15: Mass gain curves for T22 exposed with NaCl, KCl, NaCl/ZnCl$_2$ and KCl/ZnCl$_2$ coatings respectively, as well as for clean exposures without salt.

When comparing the mass gains for the different systems in Figure 15, both salt mixtures exhibit smaller mass gains after 24 hours of exposure than their respective pure alkali salts after the same exposure times. While the NaCl/ZnCl$_2$ mixture gives approximately the same mass gain as pure NaCl after 168 hours of exposure time, this behaviour is not observed when considering the KCl/ZnCl$_2$ mixture and the pure KCl: The KCl/ZnCl$_2$ mixture has a considerably lower mass gain than the corresponding KCl exposure.

Results from the gravimetric analysis on all samples exposed for 24 hours at 400°C are presented in Figure 16 below.

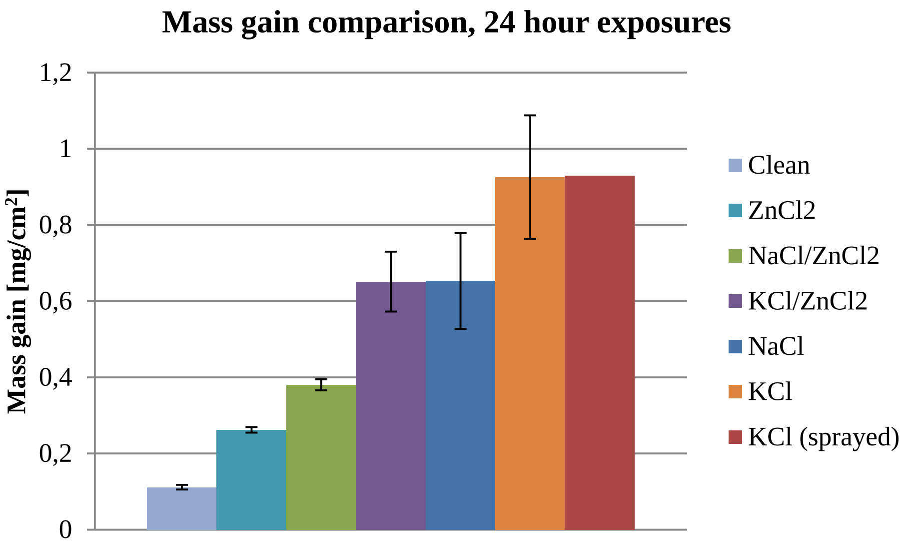

Figure 16: Summary and comparison of the 24 hour exposures.

As seen in Figure 16, the mass gains for the different exposed systems vary considerably. The mass gains for the pure alkali salts are higher than for their respective mixtures with $ZnCl_2$, while pure $ZnCl_2$ yields a lower mass gain than any of the other salts and mixtures. It is however important to stress that $ZnCl_2$ has earlier been reported to exhibit high evaporation rates during exposure, which in turn could lower the mass gain [36]. For the alkali salts, KCl yields a higher mass gain than NaCl. Additionally, the salt application method does not affect the mass gain, as KCl applied through spraying yields the same mass gain as KCl applied with pipette.

7.2 XRD

All systems were analysed with XRD to identify phases on the surfaces of the exposed samples. The results are summarized in Table 5:

Table 5: Summary of the XRD analyses performed on the different studied systems. S, M and W denote diffraction peak strength; S: Strong, M: Medium, W: Weak.

System Phase	**Clean 24h**	**NaCl 1h**	**NaCl 24h**	**NaCl 168h**	**$ZnCl_2$ 24h**	**KCl 24h**	**NaCl/$ZnCl_2$ 1h**	**NaCl/$ZnCl_2$ 24h**	**NaCl/$ZnCl_2$ 168h**	**KCl/$ZnCl_2$ 1h**	**KCl/$ZnCl_2$ 24h**	**KCl/$ZnCl_2$ 168h**
Fe_2O_3	S	W	S	S	M	S	S	S	M	M	S	S
Spinel oxide	S	S	S	S	S	S	S	S	S	S	M	S
KCl						M				M	W	M
NaCl		S	M	S			M	W	W			
ZnO								W				
$ZnCl_2$					W		W	W			W	

According to Table 5, Fe_2O_3 and spinel oxide forms in every system. Whereas the intensity of the Fe_2O_3 phase varies from weak to strong, the spinel oxide almost exclusively gives rise to strong diffraction peaks. This indicates that spinel oxide formation is favoured in the examined systems. As the Fe in Fe_2O_3 is more oxidised (Fe(III)) than the Fe in the spinel oxide (two Fe(III) and one Fe(II)), the Fe_2O_3 should be the outermost formed Fe oxide on T22 due to that the partial pressure of O_2 is in the gas phase. The NaCl systems give rise to medium to strong NaCl peaks, indicating that much NaCl still remain after exposure. The $ZnCl_2$ exposure displays a weak $ZnCl_2$ peak, suggesting a loss of detectable salt. A medium intensity peak is observed for the 24 hour KCl exposure, indicating that some unreacted KCl remains on the sample post exposure. After exposure as a part of a mixture the alkali salts remain detectable, however in smaller extents than for the pure alkali systems. $ZnCl_2$ yields diffraction peaks after 24 hours of exposure but not after being exposed with alkali chloride for 168 hours. ZnO is only present after 24 hours of exposure with $NaCl/ZnCl_2$.

7.3 Ion chromatography

All systems were analysed with IC. One sample from every exposure was leached and analysed. The results are presented in the table below.

Table 6: The results from the IC analysis, reported in mole% left on the samples after exposure in comparison to the amount applied with the salt coating prior exposure.

System	Mole% Cl^- left after exposure
NaCl 1 hours	78
NaCl 24 hours	65
NaCl 168 hours	77
$ZnCl_2$ 24 hours	23
KCl 24 hours	57
$NaCl/ZnCl_2$ 1 hours	40
$NaCl/ZnCl_2$ 24 hours	25
$NaCl/ZnCl_2$ 168 hours	14
$KCl/ZnCl_2$ 1 hours	51
$KCl/ZnCl_2$ 24 hours	20
$KCl/ZnCl_2$ 168 hours	9

For the NaCl system it is evident that most of the detectable Cl^- remains on the samples after exposure, nearly 75% on average as can be seen in Table 6. For the $ZnCl_2$ system after 24 hours of exposure on the other hand, the remaining amount of Cl^- is slightly less than 25%. The KCl system retains almost 60% of the applied Cl^- after 24 hours of exposure. Both the $NaCl/ZnCl_2$ as well as the $KCl/ZnCl_2$ mixtures exhibit a decrease in Cl^-. While the Cl^- content post exposure in the NaCl system does not vary more than ±5% around its average for the three different exposure times, both mixtures show a decrease in Cl^- post exposure which becomes increasingly pronounced with longer exposures. The amount Cl^- that could be detected decreased with around 40% for the $NaCl/ZnCl_2$ mixture and more than 50% for the $KCl/ZnCl_2$ mixture in between the three exposure times (1, 24 and 168 hours respectively). The evaporation of $ZnCl_2$ mentioned earlier could only partially explain the much lower Cl^- content for the samples exposed with $ZnCl_2$, $NaCl/ZnCl_2$, and $KCl/ZnCl_2$ respectively in comparison with the pure NaCl and KCl exposures, as seen in Table 6. Sole evaporation of $ZnCl_2$ cannot however account for the total loss of Cl^- as will be shown later. In some cases, the loss of Cl^- could possibly be caused by spallation of oxide post exposure.

7.4 SEM/EDX

The samples from all exposed systems were analysed with a SEM in high vacuum mode. The results of the analysis are presented in the following subsections.

7.4.1 Exposure without salt

To verify that the exposure setup was working properly, a clean unsalted 24 hour exposure was performed and compared with reference exposures. The clean exposure had a similar mass gain as the reference, and by examining Figure 17 and Table 5, it is evident that only a smooth iron oxide layer formed during exposure.

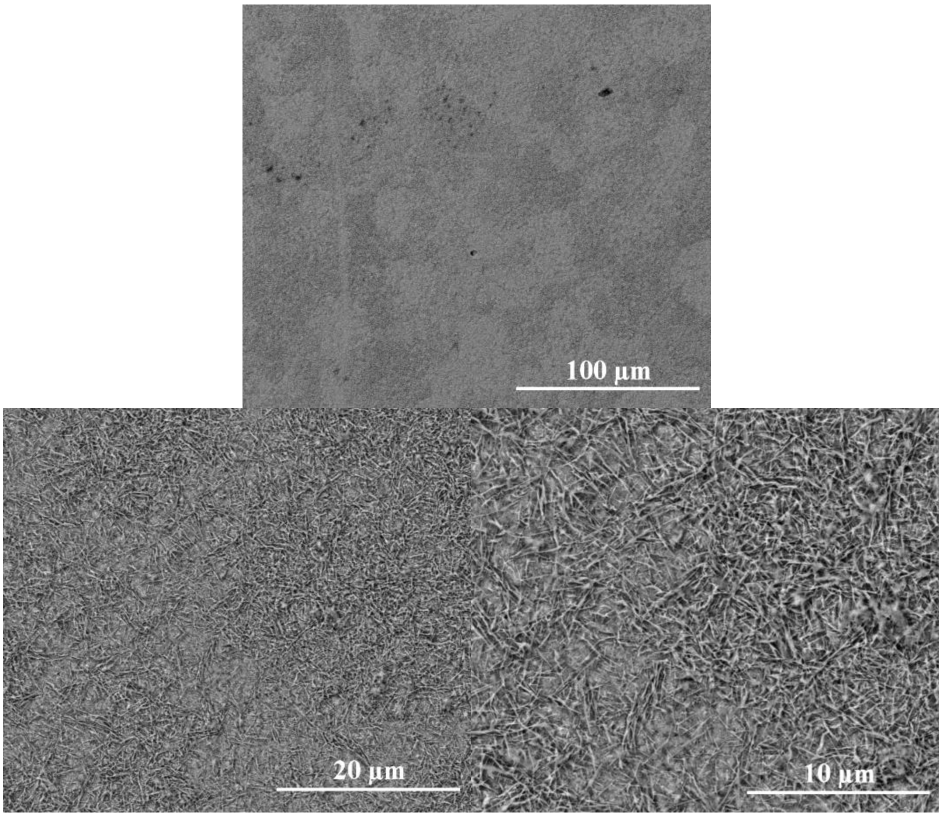

Figure 17: BSE images of sample exposed in 5% O_2 + 40% H_2O for 24 hours at 400°C. Surface is chemically homogeneous.

7.4.2 NaCl unexposed sample

The NaCl crystal size on the samples prior exposure was studied in the SEM. Two different areas were seen on the sample where NaCl had been applied, as presented in Figure 18.

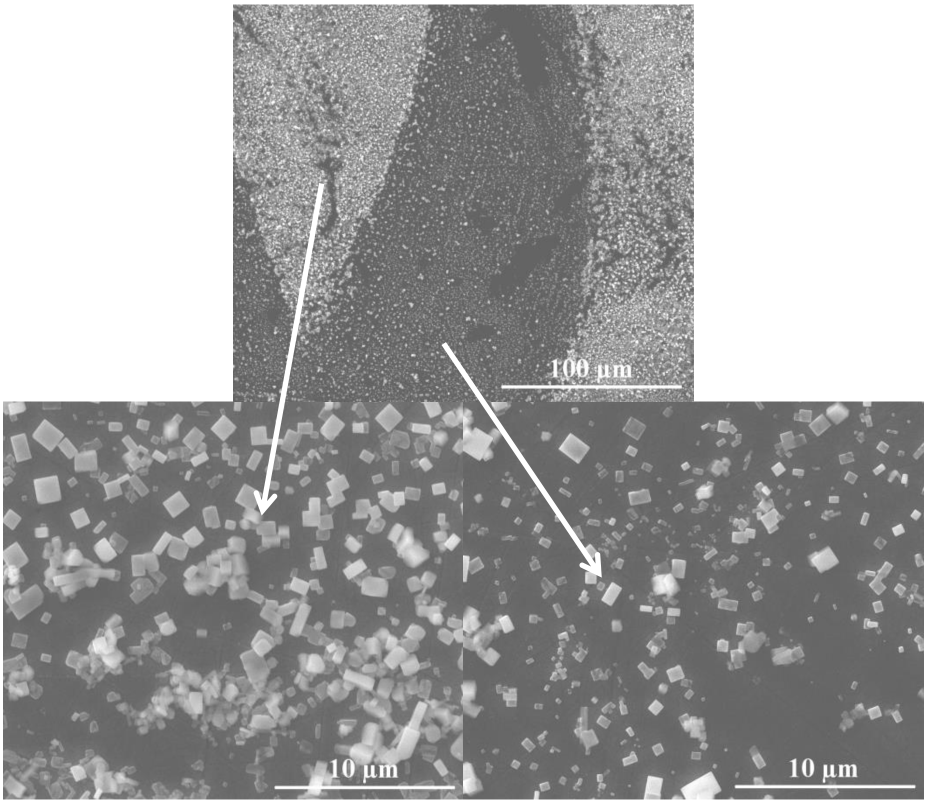

Figure 18: SEM SE images of unexposed sample coated with NaCl. Top: SE image in low magnification showing two different kinds of coated areas. Bottom: The distribution of the NaCl crystals in the two areas.

7.4.3 NaCl 1 hour exposure

The 1 hour NaCl exposure results in a mostly even oxide layer. Larger as well as smaller NaCl crystals were present on the surface after exposure, with only some areas lacking intact NaCl crystals, as can be seen in Figure 19. The crystal size increased when comparing the images taken of a salted non-exposed sample, Figure 18, and the images depicting another NaCl-covered sample that was exposed for 1 hour, Figure 19.

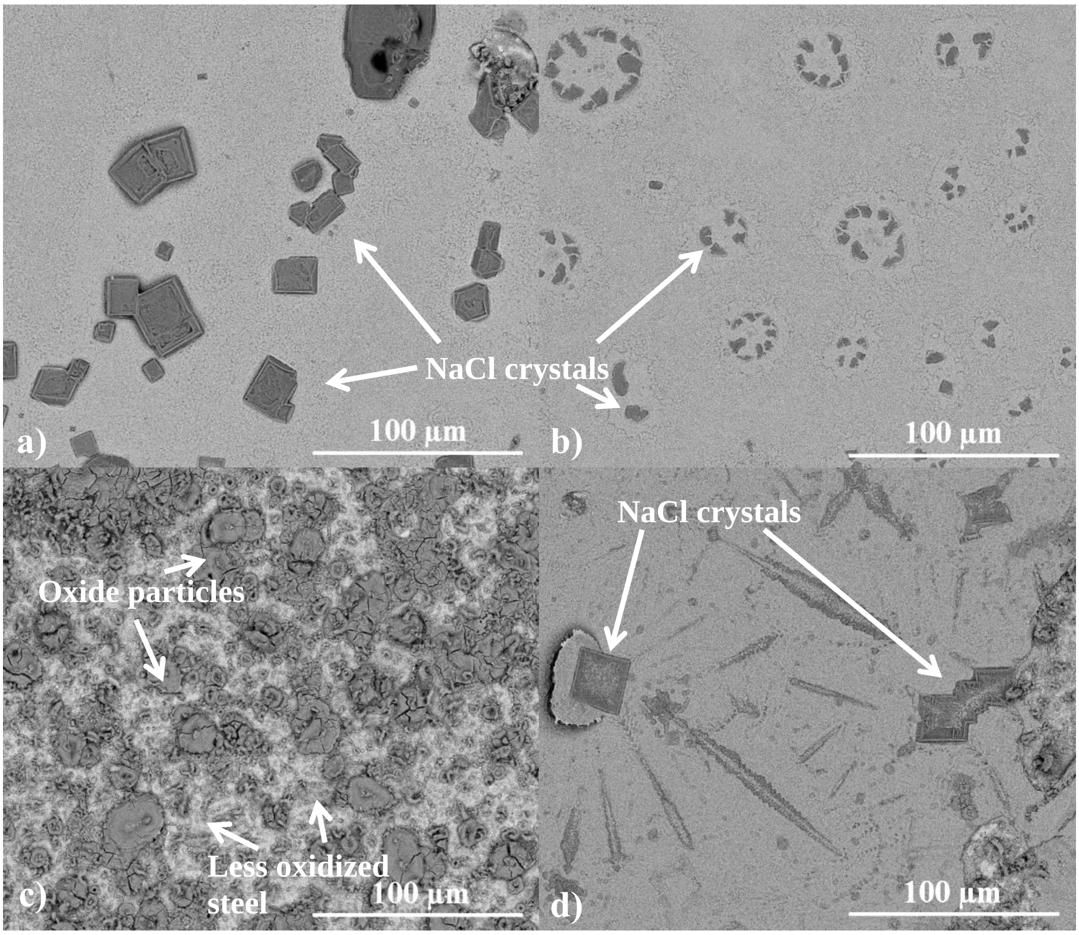

Figure 19: BSE images of sample coated with NaCl and exposed in 5% O_2 + 40% H_2O for 1 hours at 400°C. Four areas were visible (a, b, c and d).

7.4.4 NaCl 24 hour exposure

The 24 hour NaCl exposure exhibited an increasingly rougher oxide, less NaCl crystals present after exposure as well as some cracks, suggesting a thick oxide layer as seen in Figure 20.

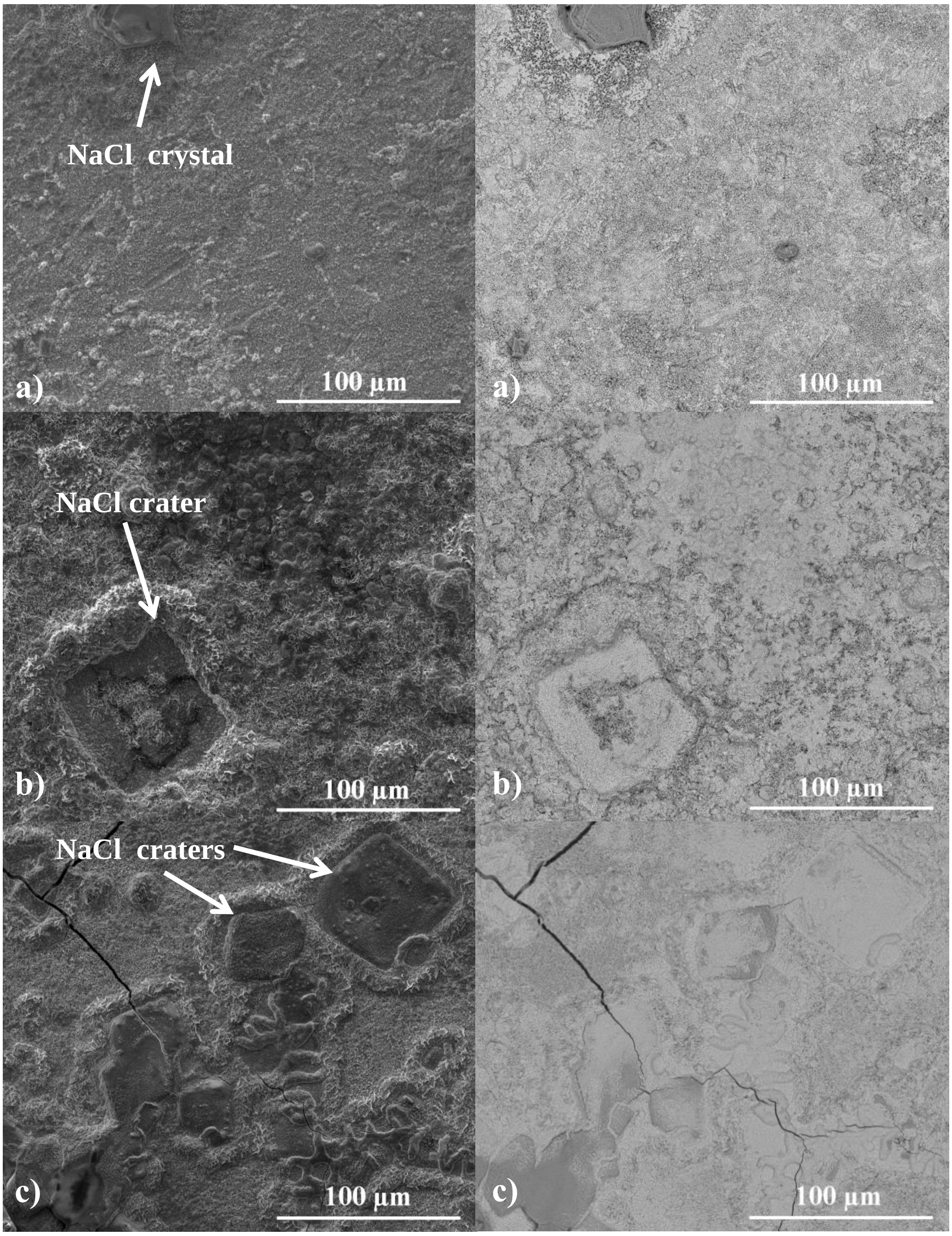

Figure 20: SE (right) and BSE (left) images of sample coated with NaCl and exposed in 5% O_2 + 40% H_2O for 24 hours at 400°C. On the previously coated surfaces three areas were visible (a, b and c). Area a) contained intact NaCl crystals while areas b) and c) contained empty voids where NaCl had been located. Furthermore, areas b) and c) exhibited a rougher oxide and area also c) had large cracks.

Empty craters/voids are visible as seen in Figure 21, and EDX analysis points to that NaCl crystals have been situated there, as evident from Table 7.

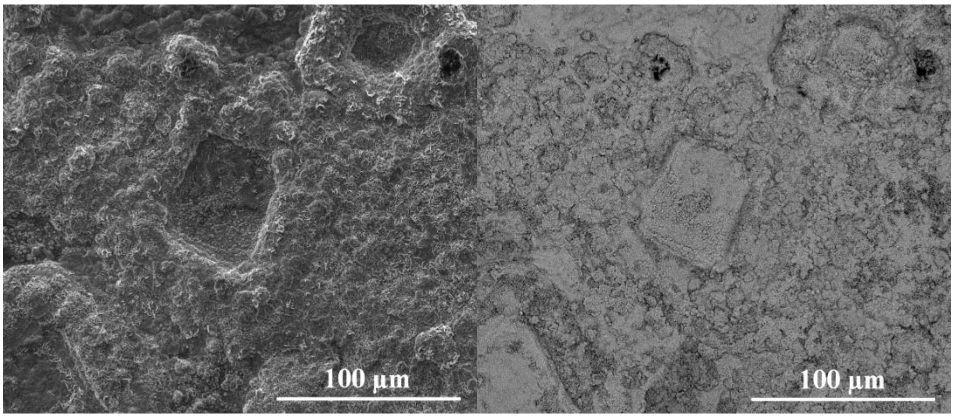

Figure 21: SE (left) and BSE (right) images showing another one of the common NaCl craters on the 24 hour exposed NaCl coated sample.

EDX point analysis was performed on the crater in Figure 21. Here, the bottom of one such crater was analysed. Results of the analysis are presented in Figure 22 and Table 7.

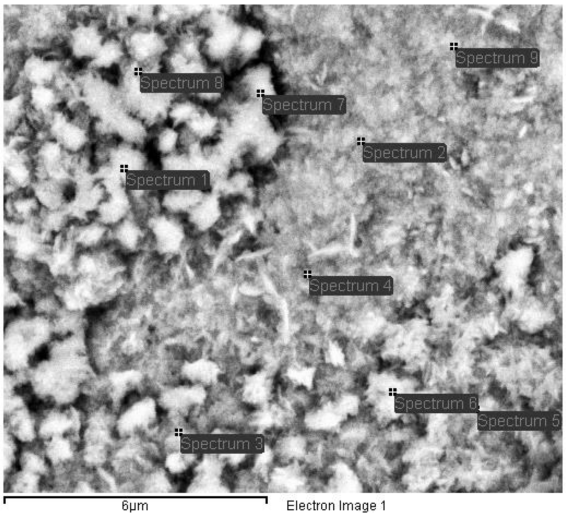

Figure 22: BSE image of the bottom of the crater that was analysed.

Table 7: Results from the EDX analysis from the area presented in the image above (atomic%). *=Trace elements.

Spectrum	**O**	**Na**	**Cl***	**Fe**	**Cu***
Spectrum 1	69	5	0,2	25	0,4
Spectrum 2	61	2	0,1	37	0,0
Spectrum 3	69	4	0,3	27	0,1
Spectrum 4	57	3	0,1	40	0,1
Spectrum 5	66	3	0,4	30	0,8
Spectrum 6	67	3	0,3	30	0,3
Spectrum 7	70	4	0,2	25	0,4
Spectrum 8	67	3	0,3	30	0,3
Spectrum 9	64	2	0,0	33	0,1
Mean	66	3	0,2	31	0,3

According to Table 7, the area analysed has a Cl deficit. As all Cl in the system initially should be associated with Na, this suggests that the Na has reacted with Fe and O, forming some type of Na-Fe-spinel. The Cu content detected is probably due to contamination, as no Cu has been added to the system by purpose.

7.4.5 NaCl 168 hour exposure

The samples exposed for 168 hours with NaCl still showed remaining NaCl crystals, both intact and half depleted, along with empty craters as can be seen in Figure 24. The increasingly rougher oxide visible in Figure 23 can be coupled with the increasingly higher mass gain as is illustrated in Figure 15, suggesting a thicker oxide for longer exposure times.

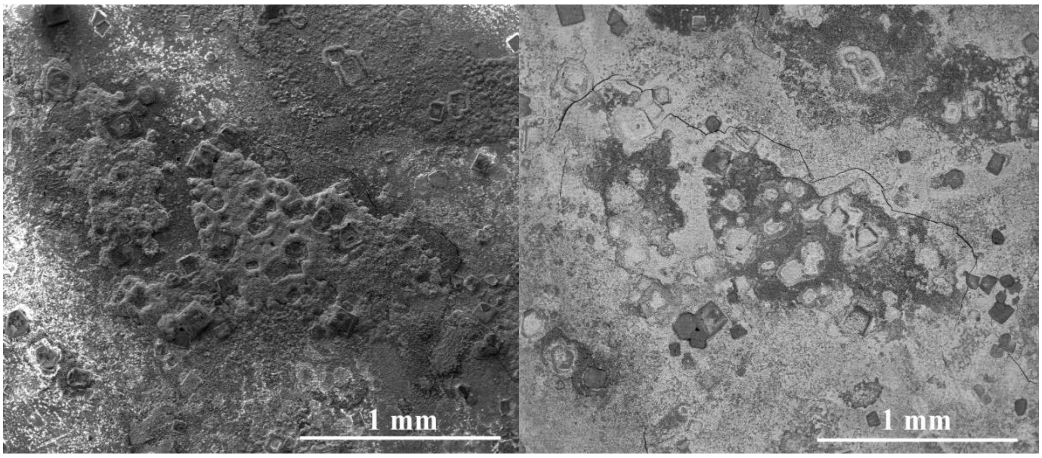

Figure 23: Overview SE (left) and BSE (right) images of a sample coated with NaCl and exposed in 5% O_2 + 40% H_2O for 168 hours at 400°C. The sample surface was rough.

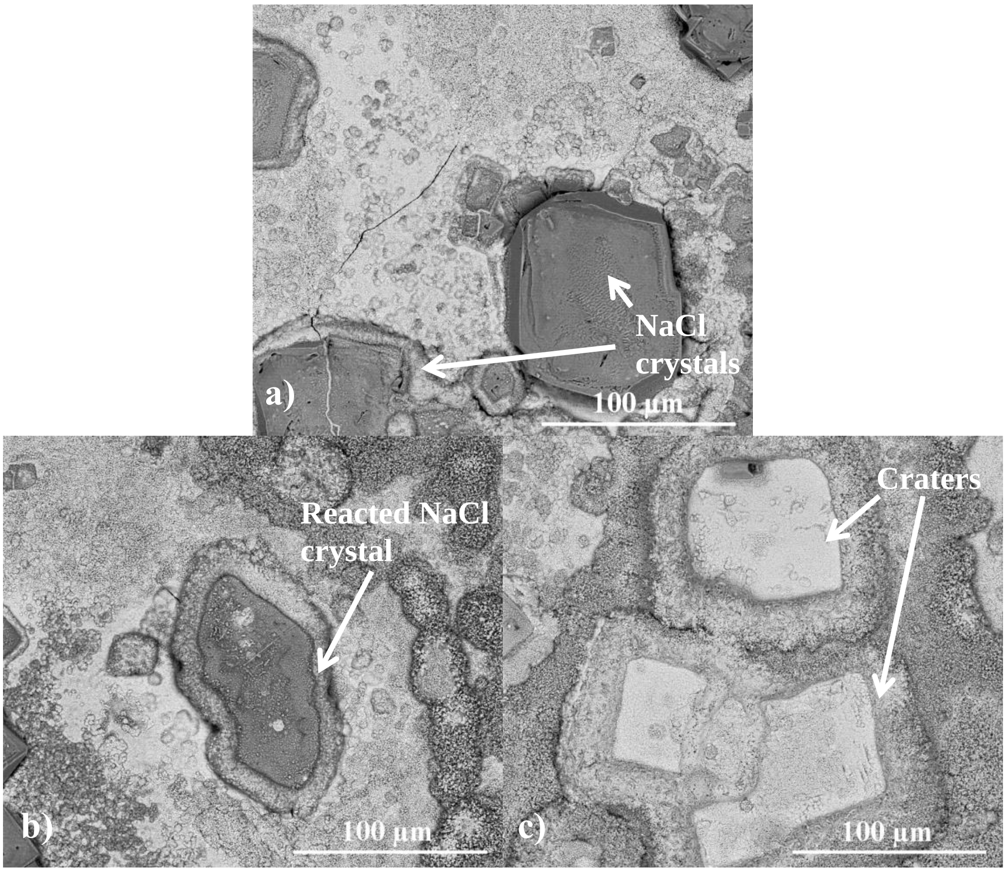

Figure 24: BSE images of sample coated with NaCl and exposed in 5% O_2 + 40% H_2O for 168 hours at 400°C. Three kinds of surface structures were present; a), b) and c), all related to the NaCl crystals that the sample had been coated with: Intact NaCl crystals as in image a), half-depleted NaCl as in image b) and craters/voids as in image c).

7.4.6 $ZnCl_2$ unexposed sample

The $ZnCl_2$ distribution on the samples prior exposure was studied in the SEM. Two different areas were seen on the sample where $ZnCl_2$ had been applied, as presented in Figure 25.

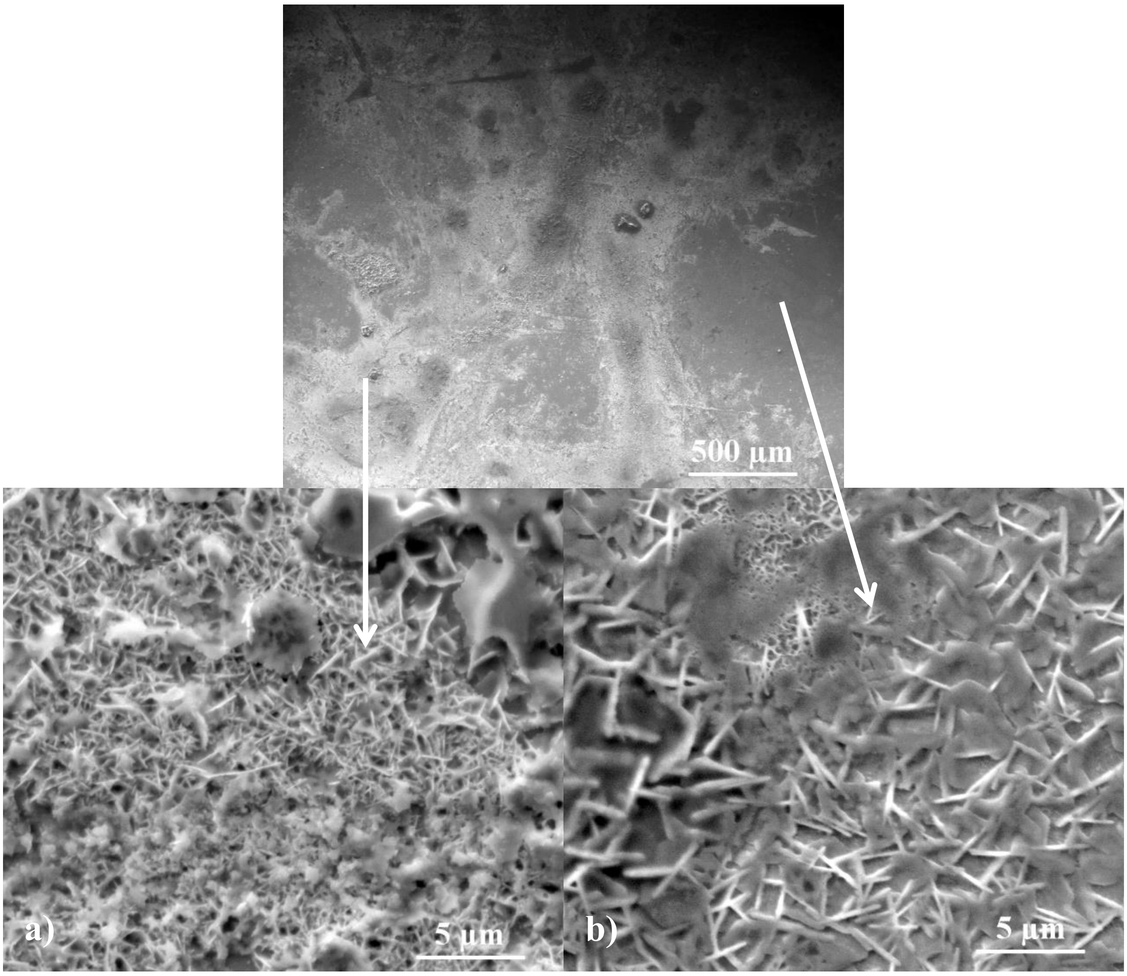

Figure 25: SE images of unexposed sample coated with $ZnCl_2$. Top: Low magnification overview of two kinds of coated areas (a and b). Bottom: The distribution and size of the $ZnCl_2$ crystals in the different areas. The brighter areas a) consist of a network of small crystals while the darker regions b) are covered with crystals of larger size.

Compared to the unexposed NaCl covered sample, Figure 18, the $ZnCl_2$ covers the sample surface in a continuous way. As for the NaCl system, the crystal size is not uniform but varies in between different regions on the sample.

7.4.7 $ZnCl_2$ 24 hour exposure

The samples exposed with $ZnCl_2$ exhibited two kinds of areas, see Figure 26. The darker parts of the image contained only traces of Zn, Table 8, while the brighter areas were slightly enriched in Zn as is evident from Table 9. The oxide was fairly smooth in the darker regions according to Figure 27, while the brighter areas suffered from cracks and spallation, Figure 30. No $ZnCl_2$ crystals could be seen post exposure although they were clearly visible prior the exposure, as is seen when comparing Figure 25, Figure 28 and Figure 29.

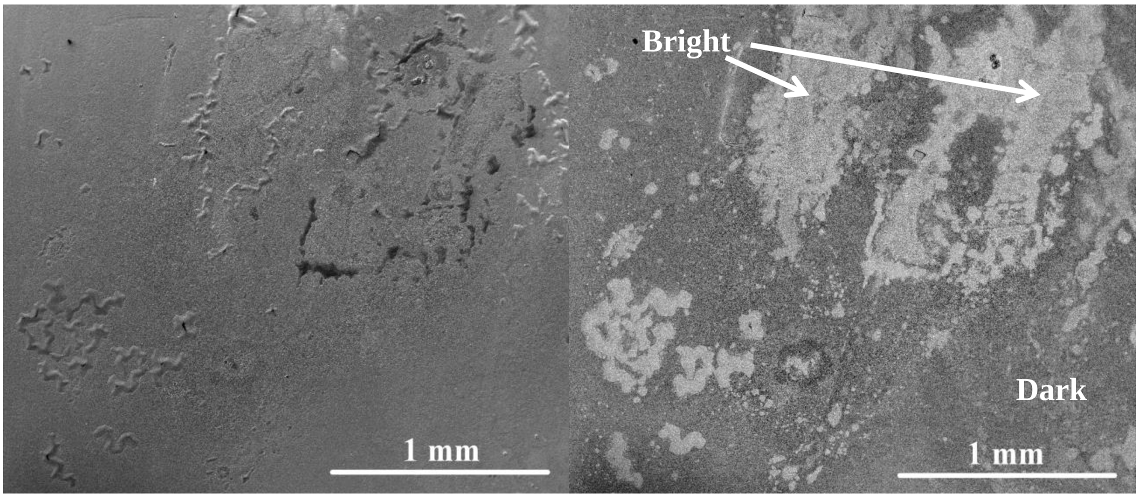

Figure 26: SE (left) and BSE (right) images of a sample coated with $ZnCl_2$ and exposed in 5% O_2 + 40% H_2O for 24 hours at 400°C. Two areas are visible in the BSE image: Brighter and darker regions.

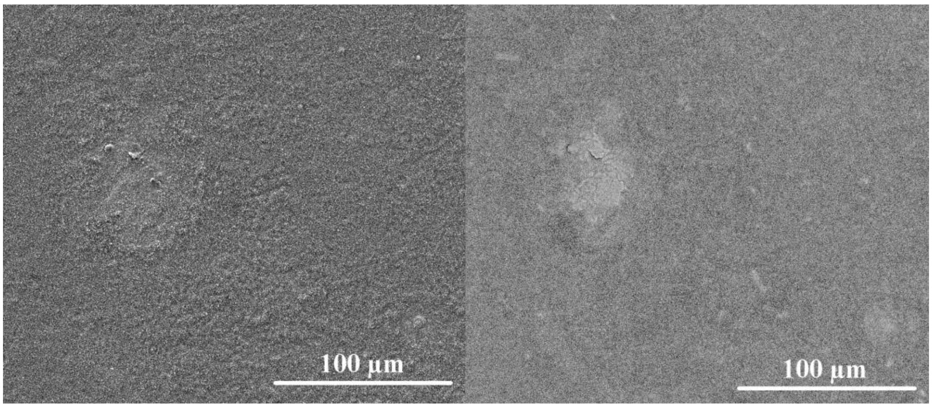

Figure 27: SE (left) and BSE (right) images of sample coated with $ZnCl_2$ and exposed in 5% O_2 + 40% H_2O for 24 hours at 400°C. The images are taken from the darker regions of the BSE image in Figure 26.

EDX analysis was performed on the darker region in the BSE image in Figure 26 above. The results of the EDX analysis are presented below.

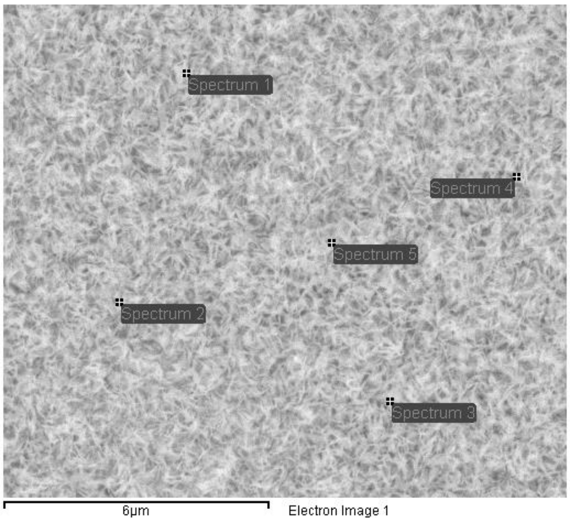

Figure 28: BSE image of an area in the darker region in Figure 26 that was analysed with EDX.

Table 8: Results from the EDX analysis of the area in Figure 28 (atomic%). *=Trace elements.

Spectrum	**O**	**Cl***	**Cr***	**Fe**	**Zn***
Spectrum 1	68	0,0	0,2	31	0,2
Spectrum 2	64	0,1	0,3	35	0,3
Spectrum 3	65	0,0	0,2	34	0,2
Spectrum 4	60	0,1	0,3	39	0,3
Spectrum 5	69	0,0	0,2	31	0,1
Mean	65	0,0	0,2	34	0,2

According to Table 8, the dark regions consist of Fe oxide, likely Fe_2O_3, with traces of Zn.

EDX analysis was performed on the brighter region in the BSE image in Figure 26 above. The results of the EDX analysis are presented below.

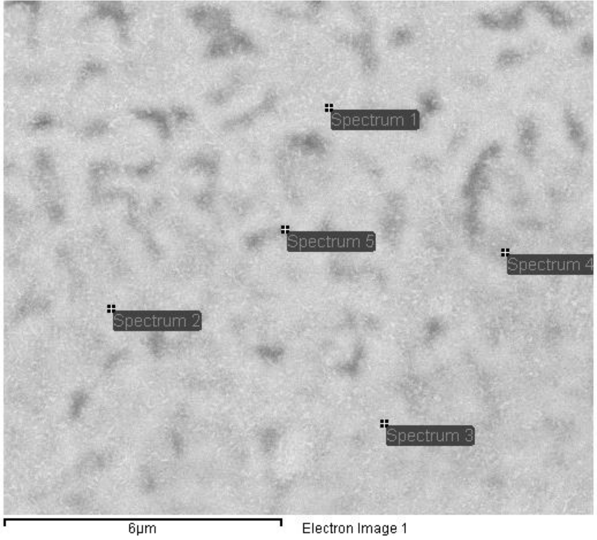

Figure 29: BSE image of an area in the brighter region in Figure 26 that was analysed with EDX.

Table 9: Table. Results from the EDX analysis of the area in Figure 29 (atomic%). The brighter regions are more Zn-rich than the darker areas. Traces of Cl can be observed. *=Trace elements.

Spectrum	**O**	**Cl***	**Cr***	**Fe**	**Zn***
Spectrum 1	65	0,1	0,3	33	1,6
Spectrum 2	66	0,1	0,2	33	1,4
Spectrum 3	67	0,1	0,2	31	1,6
Spectrum 4	63	0,1	0,4	36	1,4
Spectrum 5	62	0,1	0,3	36	1,4
Mean	65	0,1	0,3	34	1,5

The area in Figure 29 consisted mostly of Fe oxide, likely Fe_2O_3. The additional Zn content could be present as a part of some Zn-Fe-oxide due to a Cl deficit which is clearly seen in Table 9.

The brighter areas in Figure 26 contained some structures on the surface as presented in Figure 30 below. Furthermore, the oxide was cracked in several places and signs of spallation could be observed.

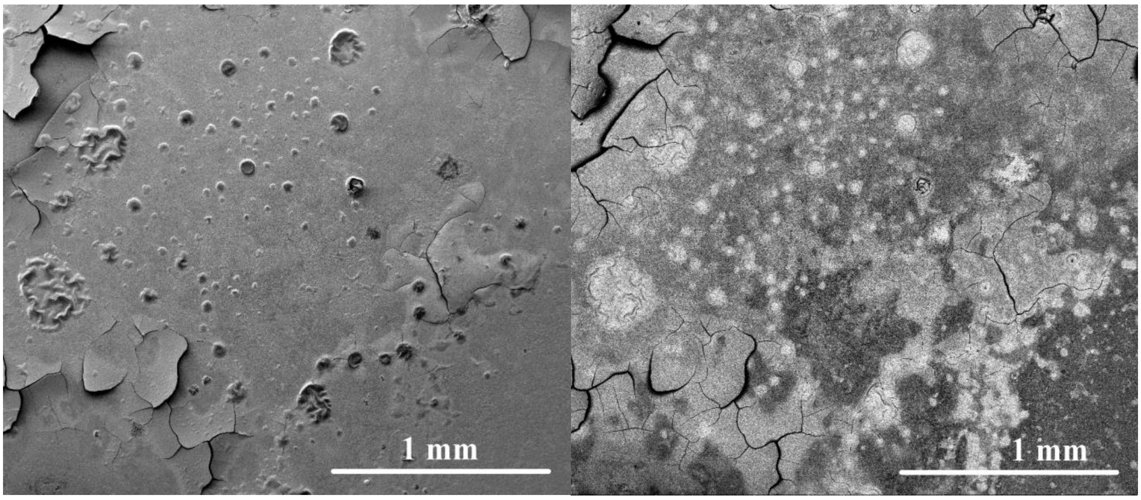

Figure 30: SE (left) and BSE (right) images of sample coated with $ZnCl_2$ and exposed in 5% O_2 + 40% H_2O for 24 hours at 400°C. The brighter areas in the BSE images are associated with the structures that are present in clusters on the surface. Large cracks and signs of spallation can be observed.

The brighter Zn-containing areas have structures such as the one visible in Figure 31. These structures have ridges and valleys, the former containing slightly more Zn than the latter as is clearly seen when comparing Table 10 and Table 11.

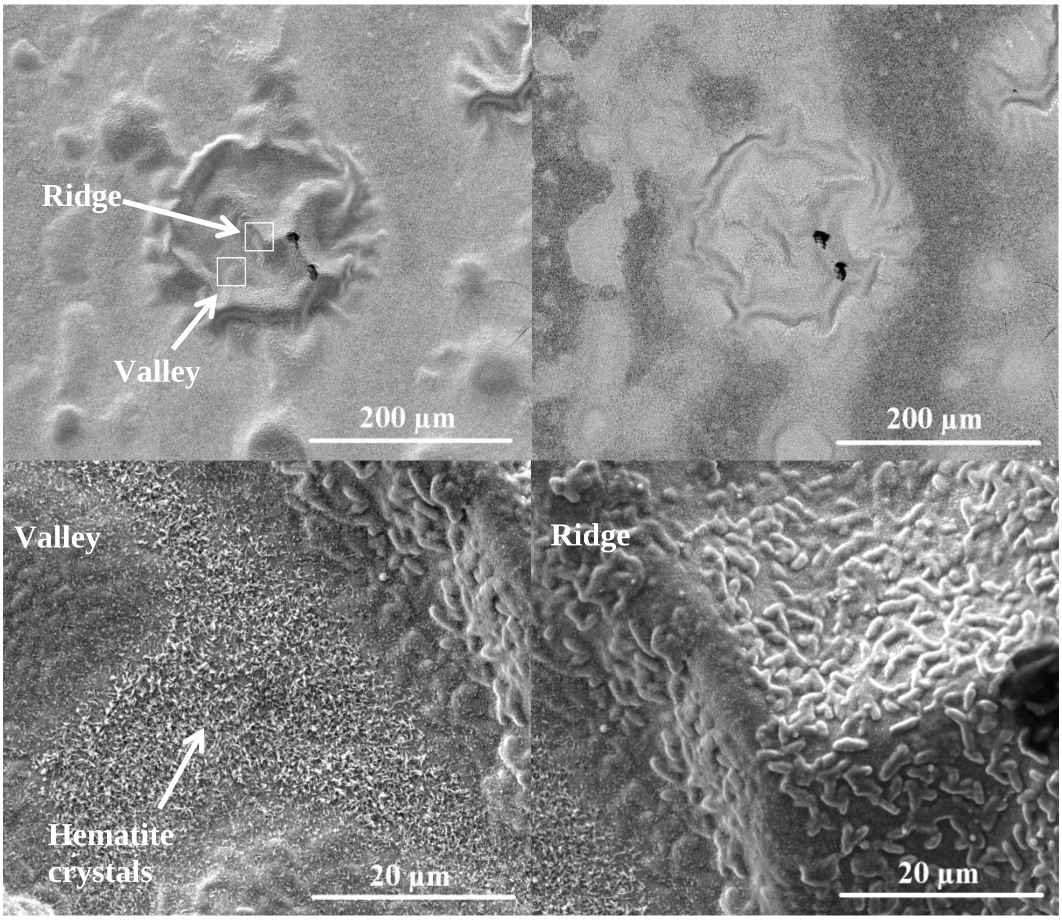

Figure 31: SEM images of sample coated with $ZnCl_2$ and exposed in 5% O_2 + 40% H_2O for 24 hours at 400°C showing a typical surface structure. Top row: SE (right) and BSE (left) images illustrating the morphology and chemical homogeneity of a typical structure. Bottom row: SE images depicting the surface morphology of a valley (left) and a ridge (right) in the structure. Hematite can be seen in the valley regions.

Despite the lower mass gain in the $ZnCl_2$ exposures in comparison with the other exposed systems, $ZnCl_2$ reportedly still causes corrosion to a significant extent as cross-sectional analysis has showed in earlier works [36]. The structures visible in Figure 30 and Figure 31 are signs of buckling, which combined with the major cracks in the brighter Zn-containing areas coupled with the spallation visible in Figure 30 indeed advocate that the extent of corrosion caused by $ZnCl_2$ might be larger than the mass gain would suggest.

EDX analysis was performed on the valley region of the structure in Figure 31 above. The results from the analysis are presented in the table below.

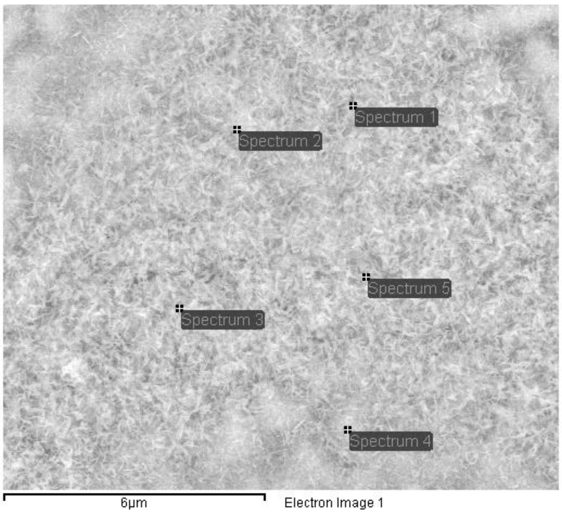

Figure 32: BSE image of the valley region in Figure 31 that was analysed with EDX.

Table 10: Results from the EDX analysis of the structure valley (atomic%). *=Trace elements.

Spectrum	**O**	**Cl***	**Cr***	**Fe**	**Zn***
Spectrum 1	65	0,1	0,3	33	1,0
Spectrum 2	66	0,1	0,2	32	1,3
Spectrum 3	66	0,1	0,3	33	1,5
Spectrum 4	68	0,2	0,2	30	1,6
Spectrum 5	65	0,0	0,2	34	1,5
Mean	66	0,1	0,3	32	1,4

The area in Figure 32 was chemically similar to the area in Figure 29. It consisted mostly of iron oxide, with a small amount of Zn. This Fe oxide was likely Fe_2O_3. The additional Zn content could be present as a part of a Zn-Fe-oxide due to a Cl deficit, just like in the area in Figure 29.

EDX analysis was performed on the ridge of the structure in Figure 31. The results of from the analysis are presented below.

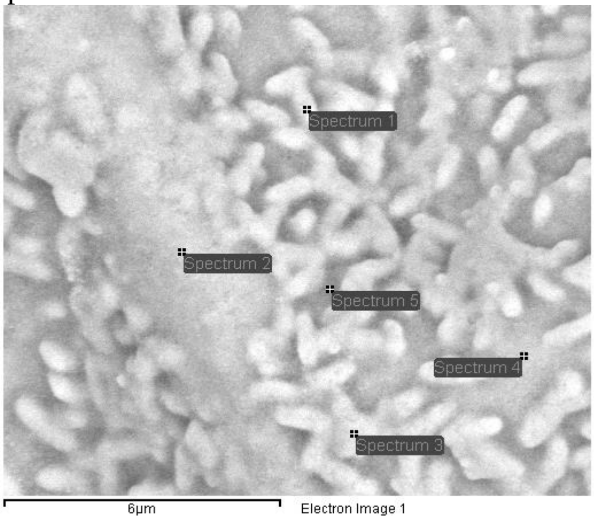

Figure 33: BSE image of the ridge region in Figure 31 that was analysed with EDX.

Table 11: Results from the EDX analysis of the structure ridge in Figure 33 (atomic%). The ridges contain more Zn than the valley regions. *=Trace elements.

Spectrum	**O**	**Cl***	**Cr***	**Fe**	**Zn**
Spectrum 1	74	0,1	0,2	24	2
Spectrum 2	65	0,1	0,2	33	2
Spectrum 3	64	0,1	0,3	33	3
Spectrum 4	64	0,1	0,3	33	2
Spectrum 5	65	0,1	0,3	33	2
Mean	66	0,1	0,3	31	2

7.4.8 KCl unexposed sample

The KCl crystal size on the samples prior exposure was studied in the SEM. Two different areas were seen on the sample where KCl had been applied, as presented in Figure 34. The crystals that form are of approximately the same size as for the NaCl system, Figure 18. The crystal size distribution was broader in area a) in Figure 34 and much narrower in area b). Furthermore, the spacing in between the crystals was larger in area b) compared to area a).

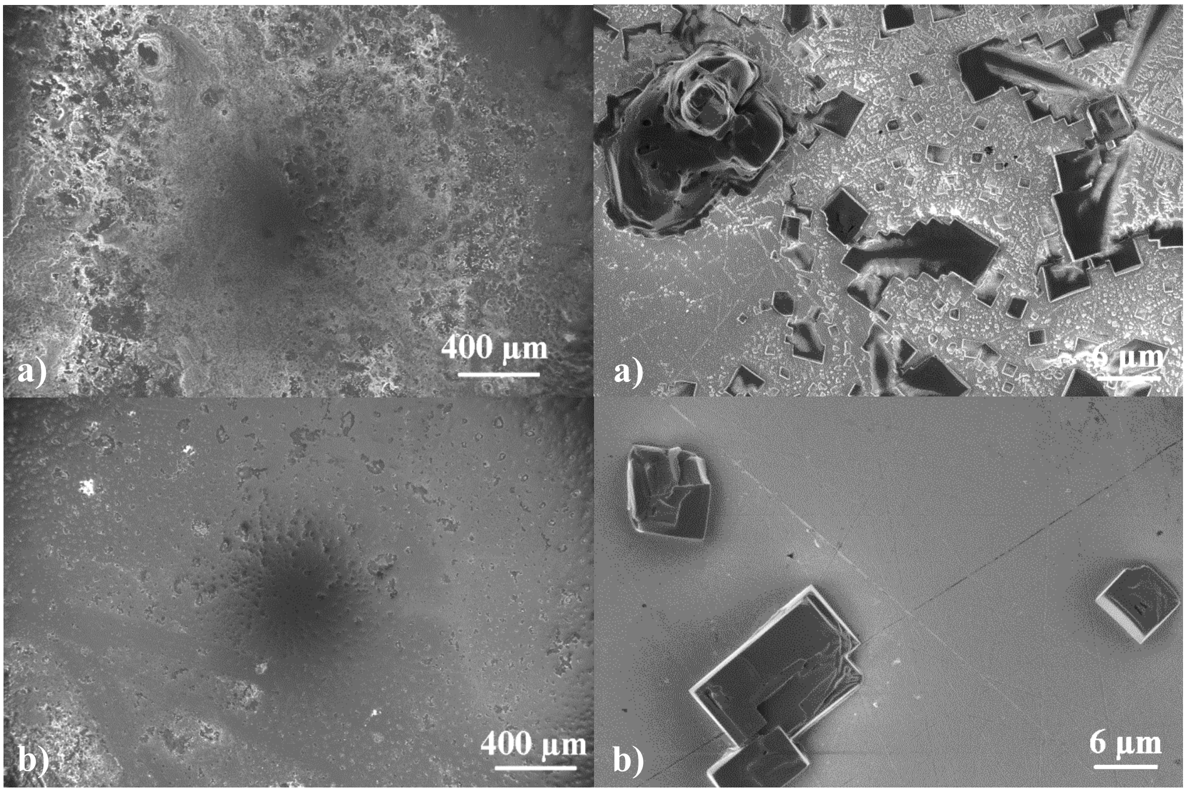

Figure 34: SE images of unexposed sample coated with KCl. Two kinds of coated areas were visible, where the size and distribution of the KCl crystals varied. Top row images show a region with larger crystals surrounded by many small ones; the crystal size distribution was broad. Bottom row images display a different area where the size distribution was narrow, where only larger crystals could be observed with no smaller crystals in between.

7.4.9 KCl 24 hour exposure

Some of the KCl crystals were still present as small clusters after 24 hours of exposure, Figure 37. The structures visible on the surface however, such as the one visible in area a) in Figure 35, did not contain so much KCl according to the EDX analysis presented in

Table 12. The oxide layer covering the surface was fairly rough with occasional cracks which suggest a thicker oxide. This general morphology is shown in the images in Figure 35. A thicker oxide would be in good agreement with the high mass gain for the KCl exposure presented in Figure 16 as well as for the reference KCl exposures in Figure 15.

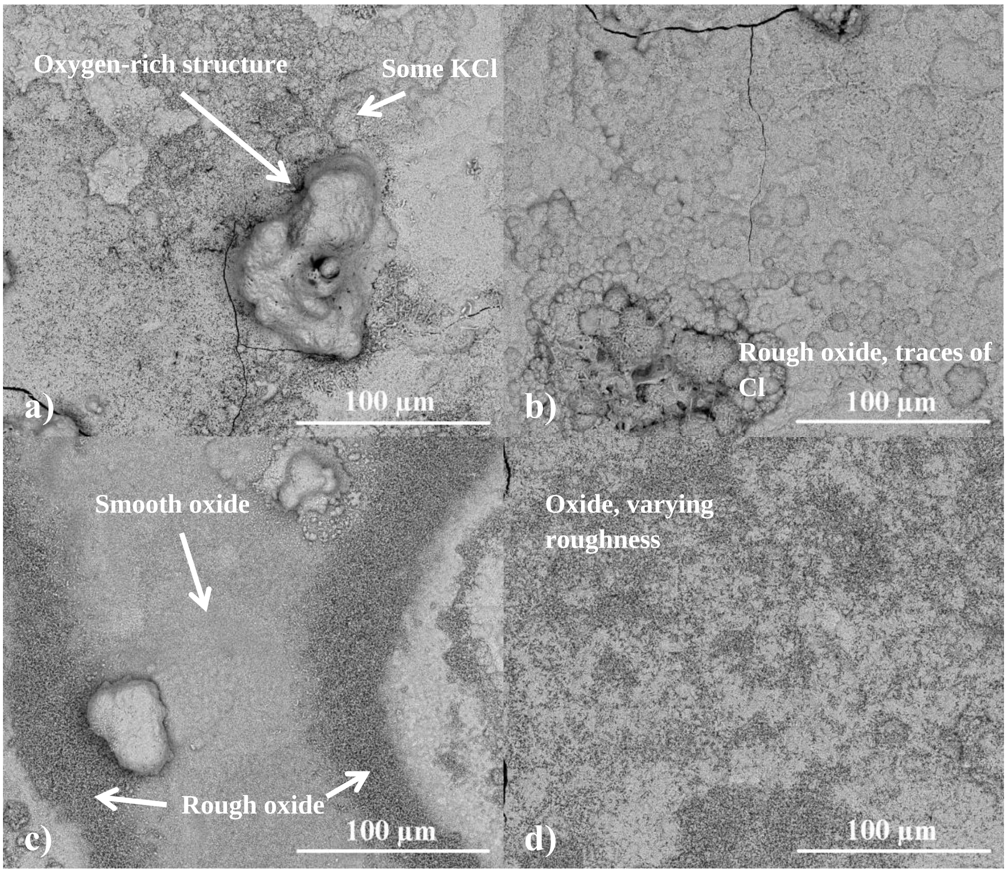

Figure 35: BSE images of sample coated with KCl and exposed in 5% O_2 + 40% H_2O for 24 hours at 400°C. Four areas were visible (a, b, c and d).

EDX analysis was performed on a magnified portion in area a) in Figure 35. The results are presented below.

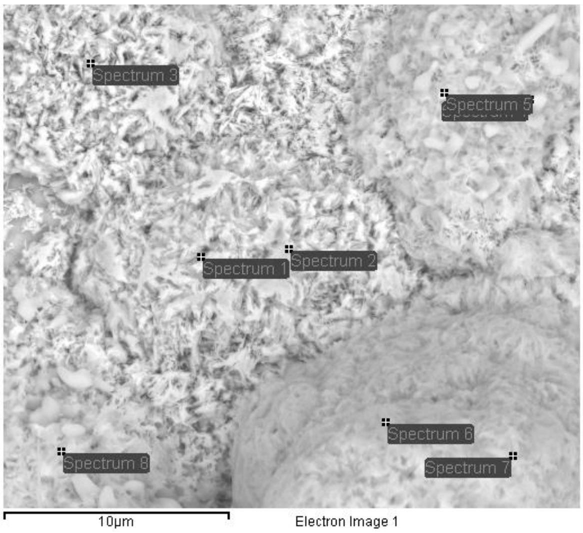

Figure 36: The area in image a) in Figure 35 that was analysed with EDX.

Table 12: Table. The results of the EDX analysis of the region in Figure 36 (atomic%). *=Trace elements.

Spectrum	**O**	**Cl***	**K**	**Cr***	**Fe**
Spectrum 1	68	0,0	0	0,0	32
Spectrum 2	68	0,0	1	0,1	31
Spectrum 3	57	0,0	1	0,2	42
Spectrum 4	53	12,5	12	0,0	22
Spectrum 5	60	4,2	5	0,1	31
Spectrum 6	74	0,0	0	0,0	26
Spectrum 7	74	0,0	0	0,1	25
Spectrum 8	68	0,3	1	0,0	30
Mean	65	2,1	3	0,1	30

According to Table 12, the area in Figure 36 consisted mainly of Fe oxide, most likely Fe_2O_3. Spectrum 4 and 5 exhibits higher Cl and K content, indicating that unreacted KCl remains on the sample after the exposure.

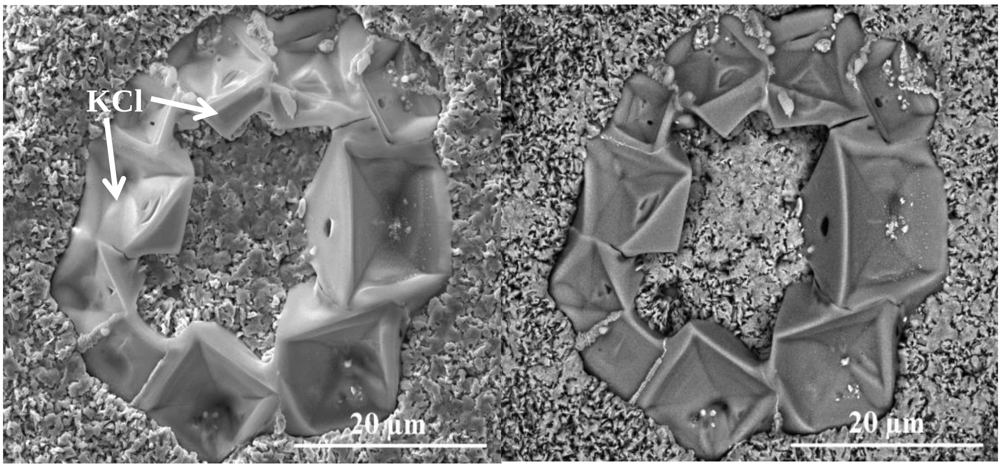

Figure 37: SE (left) and BSE (right) images depicting one of the numerous salt KCl particles littering the sample surface.

EDX analysis was performed on the area surrounding the KCl crystals visible in Figure 37. The results of the analysis are presented below.

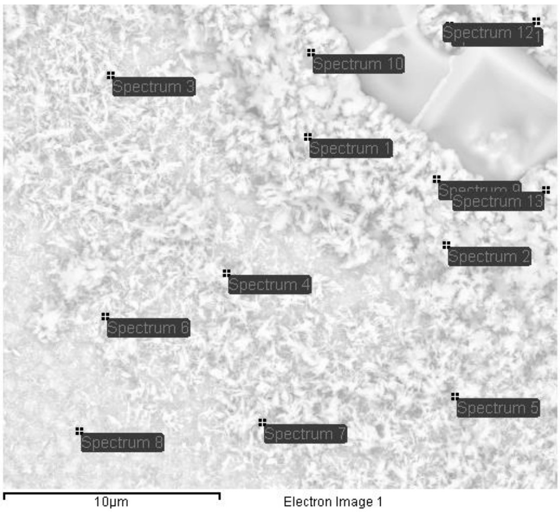

Figure 38: The area next to the KCl crystals in Figure 37 that was analysed with EDX.

Table 13: Results from the EDX analysis of the area surrounding the KCl crystals in Figure 37 (atomic%). *=Trace elements.

Spectrum	**O**	**Cl***	**K***	**Cr***	**Fe**
Spectrum 1	75	0,4	0,4	0,1	24
Spectrum 2	72	0,2	0,2	0,2	28
Spectrum 3	70	0,0	0,3	0,2	30
Spectrum 4	74	0,3	0,4	0,1	25
Spectrum 5	67	0,0	0,4	0,2	32
Spectrum 6	55	0,0	0,0	0,3	45
Spectrum 7	55	0,0	0,2	0,3	45
Spectrum 8	60	0,0	0,2	0,3	39
Spectrum 9	66	0,3	0,4	0,0	33
Spectrum 10	63	0,0	0,3	0,2	37
Spectrum 11	68	1,1	0,9	0,1	30
Spectrum 12	71	0,9	0,7	0,2	27
Spectrum 13	60	0,8	0,7	0,2	37
Mean	66	0,3	0,4	0,2	33

According to Table 13, the area in Figure 38 consisted mostly of Fe oxide, likely Fe_2O_3, along with traces of KCl that remained on the sample after exposure.

7.4.10 NaCl/$ZnCl_2$ mixture unexposed sample

The NaCl and $ZnCl_2$ crystal size on the samples prior exposure was studied in the SEM. Differently sized salt crystal clusters were seen, Figure 40, and the distribution of these clusters was even, Figure 39. The NaCl rested on top of a $ZnCl_2$ layer that covers the sample, which is easier seen when looking at areas with less NaCl present as in Figure 41. When compared to the unexposed sample that was covered with NaCl, Figure 18, the NaCl clustering for the NaCl/$ZnCl_2$ mixture was extensive, producing large agglomerates instead of the single, evenly dispersed crystals seen in the NaCl system. The $ZnCl_2$ in the NaCl/$ZnCl_2$ mixture on the other hand obtained a similar appearance and degree of surface coverage as the $ZnCl_2$ crystals in the pure $ZnCl_2$ system, Figure 25.

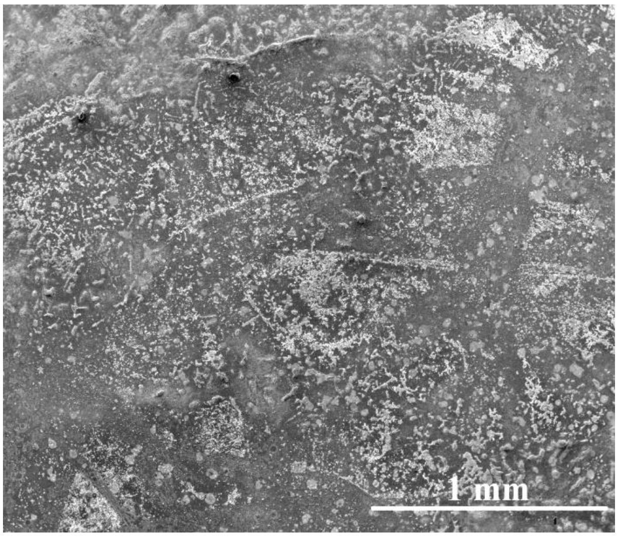

Figure 39: Overview SE image of the surface of a sample coated with the NaCl/ZnCl$_2$ mixture.

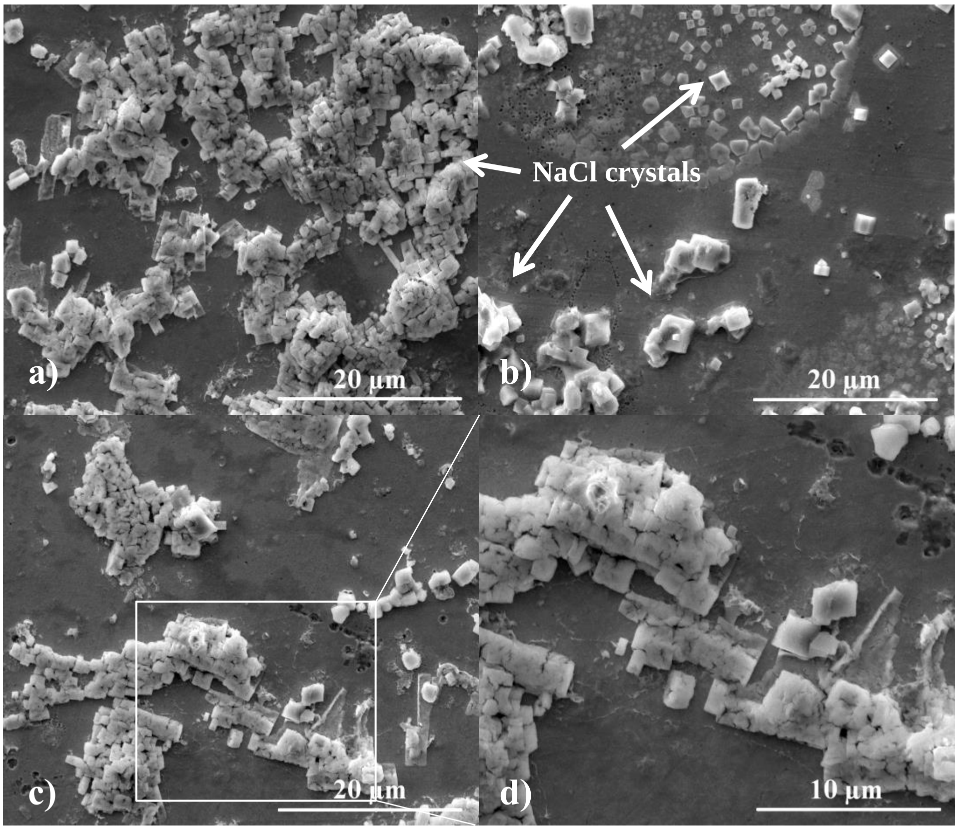

Figure 40: SE images of magnified areas on the NaCl/ZnCl$_2$ coated sample that were rich in NaCl clusters (a, b and c). Area c) was magnified and shown in d) to show the small crystals making up the NaCl cluster.

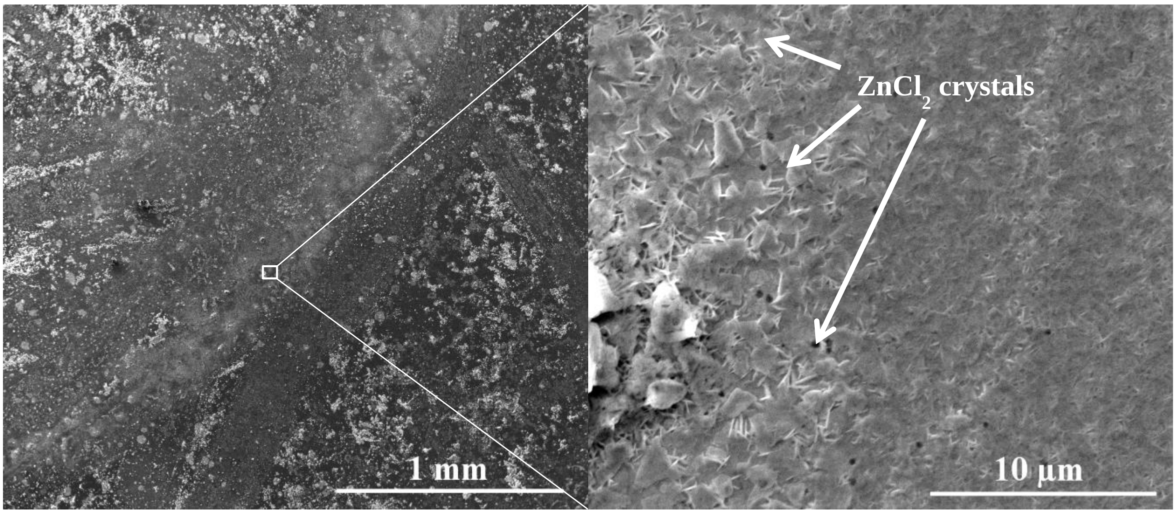

Figure 41: SE images of another area on the NaCl/ZnCl$_2$ coated sample. The region depicted contained less NaCl but was rich in ZnCl$_2$.

7.4.11 NaCl/$ZnCl_2$ 24 hour exposure

The NaCl/$ZnCl_2$ mixture yielded a mixture of separated areas with rough and smooth oxide after 24 hours of exposure, as visible in Figure 42. The space in between these structures did only contain traces of salt, as can be seen in Table 17. Cracks were visible in certain areas, Figure 42, which would suggest a thick oxide. The mass gain was however lower than for pure NaCl as presented in Figure 16, which is slightly contradictory since a thicker oxide should yield a higher mass gain. Spallation might be a possible cause of this inconsistency.

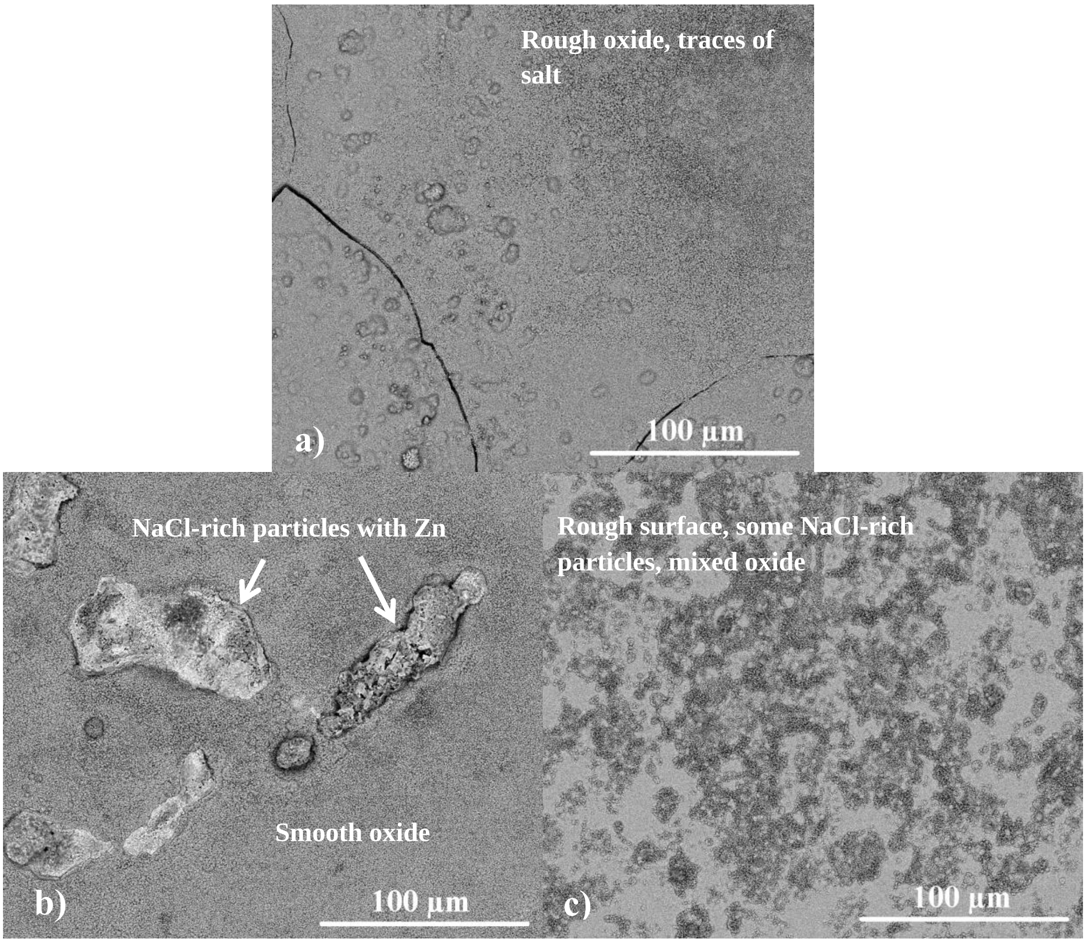

Figure 42: BSE images of sample coated with a NaCl/$ZnCl_2$-mixture and exposed in 5% O_2 + 40% H_2O for 24 hours at 400°C. Three areas were visible where coating had been applied (a, b and c).

EDX analysis was performed on a magnified portion in area a) in Figure 42. The results are presented below.

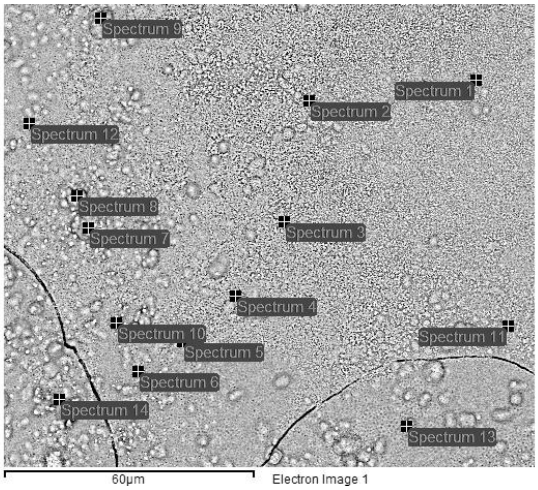

Figure 43: The area in image a) in Figure 42 that was analysed with EDX.

Table 14: The results of the EDX analysis of the area in Figure 43 (atomic%). *=Trace elements.

Spectrum	**O**	**Na**	**Cl***	**Cr***	**Mn***	**Fe**	**Cu***	**Zn***
Spectrum 1	67	1	0,1	0,2	0,2	32	0,0	0,1
Spectrum 2	72	1	0,0	0,2	0,2	27	0,1	0,1
Spectrum 3	63	0	0,0	0,2	0,2	36	0,2	0,1
Spectrum 4	63	0	0,0	0,2	0,1	37	0,2	0,1
Spectrum 5	63	0	0,1	0,2	0,1	36	0,1	0,2
Spectrum 6	65	0	0,1	0,2	0,2	34	0,0	0,1
Spectrum 7	70	1	0,1	0,1	0,2	29	0,2	0,2
Spectrum 8	58	10	4,0	0,1	1,1	19	1,3	6,6
Spectrum 9	66	1	0,1	0,1	0,3	33	0,2	0,3
Spectrum 10	66	1	0,0	0,2	0,3	32	0,1	0,6
Spectrum 11	66	0	0,1	0,2	0,1	33	0,0	0,1
Spectrum 12	66	0	0,0	0,2	0,1	33	0,1	0,1
Spectrum 13	54	0	0,2	0,3	0,3	44	0,0	0,9
Spectrum 14	68	0	0,0	0,3	0,1	31	0,1	0,2
Mean	65	1	0,3	0,2	0,3	32	0,2	0,7

Table 14 shows that the area in Figure 43 mainly contained of Fe and O, probably as Fe_2O_3. Spectrum 8 exhibited a higher Na, Cl, Mc, Cu and Zn content. The lower Fe and O content in the same spectrum suggests that some unreacted salts may be present. Trace amounts of Mn and Cu could be a result of contamination. Presence of Cl, Cr and Zn on the other hand is plausible as T22 contains low amounts of Cr, Table 4, while Zn and Cl have been applied prior exposure as parts of salts.

EDX analysis was performed on a magnified portion in area b) in Figure 42. The results are presented below.

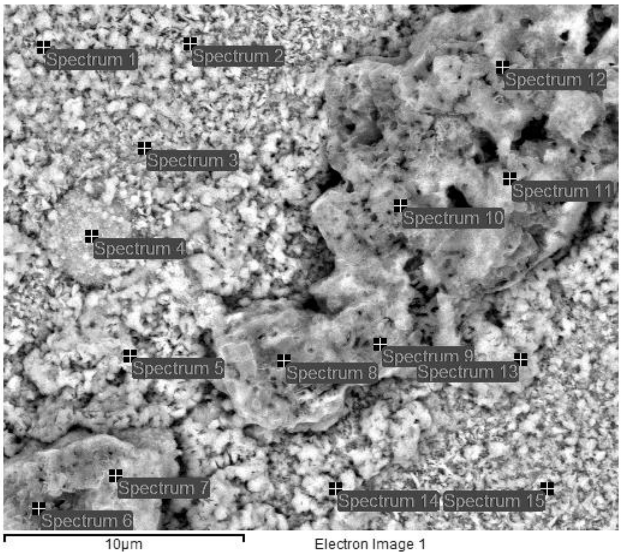

Figure 44: A magnification of area b) in Figure 42 that was analysed with EDX.

Table 15: The results of the EDX analysis of the area in Figure 44 (atomic%). *=Trace elements.

Spectrum	**O**	**Na**	**Cl**	**Cr***	**Mn***	**Fe**	**Cu***	**Zn**
Spectrum 1	62	1	0	0,1	0,1	36	0,1	0
Spectrum 2	68	1	0	0,1	0,3	30	0,1	0
Spectrum 3	58	1	0	0,2	0,1	40	0,1	0
Spectrum 4	60	9	7	0,1	0,5	14	2,7	8
Spectrum 5	68	1	1	0,1	0,2	27	0,6	1
Spectrum 6	18	37	34	0,0	0,2	2	0,1	8
Spectrum 7	36	32	19	0,0	0,3	2	0,5	10
Spectrum 8	21	38	24	0,1	0,1	9	0,2	8
Spectrum 9	16	41	31	0,1	0,1	5	0,2	7
Spectrum 10	19	41	32	0,0	0,0	2	0,0	6
Spectrum 11	23	38	30	0,0	0,0	2	0,1	6
Spectrum 12	27	39	27	0,0	0,0	2	0,0	6
Spectrum 13	67	2	1	0,1	0,4	26	0,3	3
Spectrum 14	67	2	0	0,1	0,1	29	0,2	1
Spectrum 15	69	1	0	0,2	0,2	29	0,1	0
Mean	45	19	14	0,1	0,2	17	0,4	4

Spectrums 6-12 contained high amounts of Na, Cl and Zn, suggesting that unreacted salts were still present after exposure. Spectrums 7 and 8 had a Cl deficit. The structure on the sample surface analysed in spectrums 6-12 contains high amounts of NaCl and some $ZnCl_2$. Trace amounts of Mn and Cu could be a result of contamination. No salt crystals are visible after exposure, but instead structures similar to the ones shown in image b) in Figure 42 and Figure 45 are visible. These structures contain high amounts of Na and Cl as well as some Zn as is shown in Table 16 and Table 15.

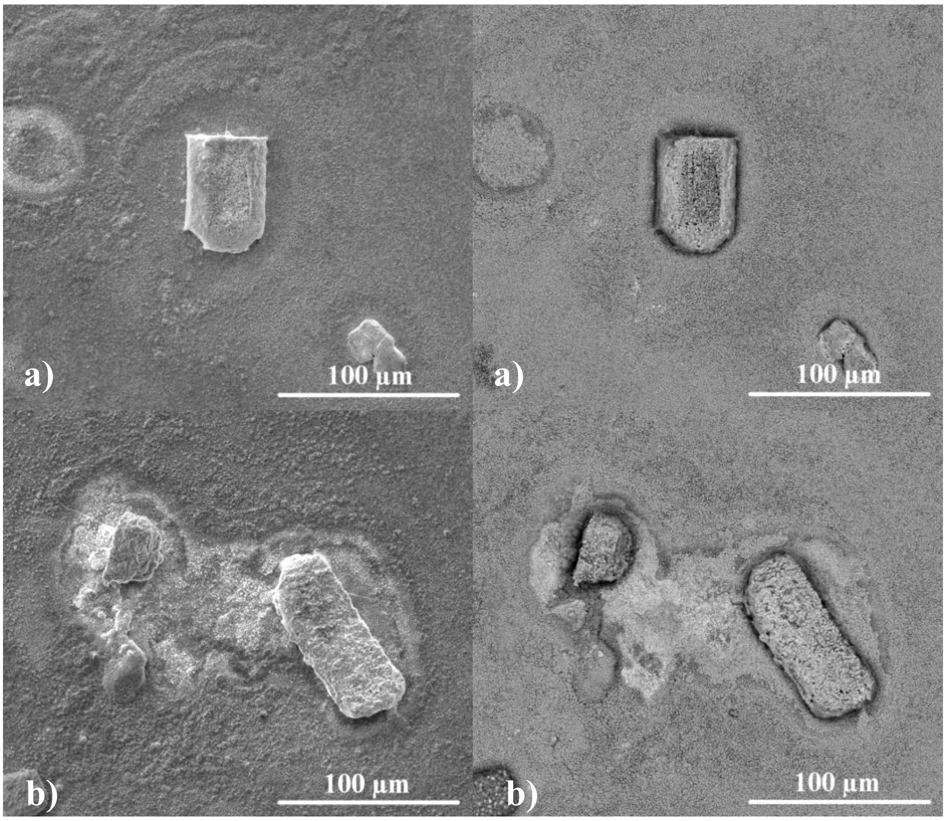

Figure 45: SE (left) and BSE (right) images displaying a common type of structure present at the surface of a sample coated with a NaCl/$ZnCl_2$-mixture and exposed in 5% O_2 + 40% H_2O for 24 hours at 400°C. Two areas with these structures are presented (a and b)

EDX analysis was performed on a magnified portion of the structure in area a) in Figure 45. The results are presented below.

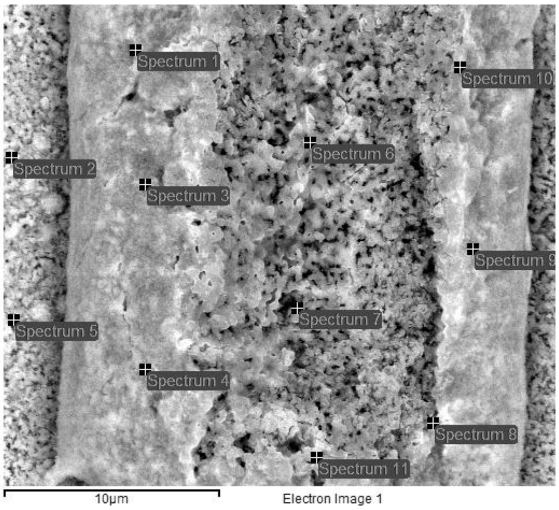

Figure 46: The magnified portion of area a) in Figure 45 that was analysed with EDX.

Table 16: The results of the EDX analysis of the region in Figure 46 (atomic%). The high content of Na, Cl and Zn suggests that the surface structures contain unreacted salt from the NaCl/$ZnCl_2$ coating applied prior exposure. *=Trace elements.

Spectrum	**O**	**Na**	**Cl**	**Cr***	**Mn***	**Fe**	**Cu***	**Zn**
Spectrum 1	36	20	24	0,0	0,1	4	0,1	16
Spectrum 2	16	1	1	0,4	0,6	80	0,3	2
Spectrum 3	38	21	26	0,0	0,0	3	0,1	12
Spectrum 4	22	20	38	0,1	0,1	4	0,1	16
Spectrum 5	11	1	1	0,4	0,5	83	0,5	3
Spectrum 6	19	38	37	0,0	0,0	1	0,0	5
Spectrum 7	20	38	34	0,0	0,0	1	0,0	6
Spectrum 8	25	34	30	0,0	0,1	2	0,1	10
Spectrum 9	32	33	28	0,0	0,0	2	0,1	5
Spectrum 10	33	33	27	0,0	0,0	2	0,0	6
Spectrum 11	23	37	32	0,0	0,0	1	0,0	6
Mean	25	25	25	0,1	0,2	17	0,1	8

According to Table 16 the O content is relatively low, suggesting strong presence of unreacted salts. This is supported by the low Fe content. In spectrums 2 and 5 however the Fe content is very high, suggesting a thin oxide layer as well as only low amounts of unreacted salt. This is confirmed by the low Na, Cl and Zn content in these points.

EDX analysis was performed on an area close to a zoomed out portion of the structure in area a) in Figure 45. The results are presented below.

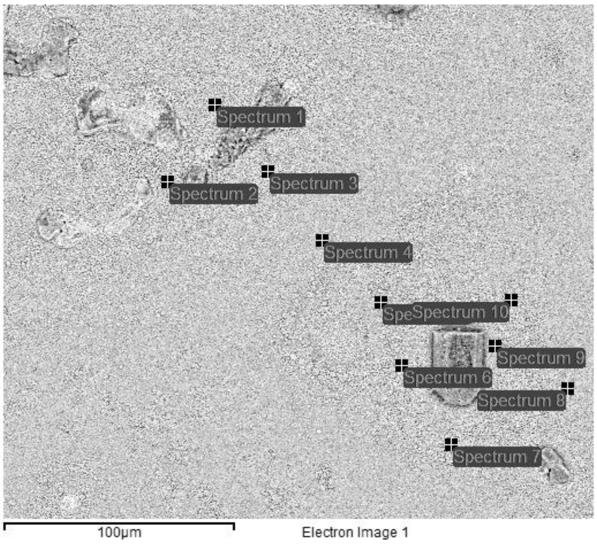

Figure 47: The zoomed out part of area a) in Figure 45 that was analysed with EDX.

Table 17: The results of the EDX analysis of the area in Figure 47 (atomic%). *=Trace elements.

Spectrum	**O**	**Na**	**Cl***	**Cr***	**Mn***	**Fe**	**Cu***	**Zn***
Spectrum 1	69	2	0,1	0,2	0,3	27	0,2	1,8
Spectrum 2	59	1	0,1	0,2	0,2	39	0,2	0,5
Spectrum 3	61	0	0,1	0,2	0,2	38	0,1	0,2
Spectrum 4	62	1	0,0	0,2	0,1	37	0,1	0,2
Spectrum 5	65	1	0,1	0,1	0,2	33	0,1	0,4
Spectrum 6	67	2	0,1	0,1	0,4	28	0,2	2,3
Spectrum 7	64	1	0,2	0,2	0,2	33	0,3	1,1
Spectrum 8	66	1	0,0	0,2	0,1	33	0,0	0,1
Spectrum 9	58	1	0,2	0,2	0,2	40	0,0	0,3
Spectrum 10	58	1	1,1	0,2	0,3	38	0,4	1,.0
Mean	63	1	0,2	0,2	0,2	35	0,2	0,8

7.4.12 KCl/ZnCl$_2$ unexposed sample

The KCl/ZnCl$_2$ crystal size and distribution on the samples prior exposure was studied in the SEM. As in the NaCl/ZnCl$_2$ system in Figure 40, the alkali chloride was present in the form of clusters with varying sizes and surface distributions on top of a continuous ZnCl$_2$ layer, as visible in Figure 48, Figure 49, Figure 50 and Figure 51. When compared to the unexposed sample that was covered with KCl, Figure 34, the KCl agglomerated into clusters rather than be present as single crystals, just as NaCl did in the NaCl/ZnCl$_2$ mixture, Figure 40. The ZnCl$_2$ obtained a similar appearance and degree of surface coverage as the ZnCl$_2$ crystals in the pure ZnCl$_2$ system, Figure 25. This was also similar to the behaviour of the ZnCl$_2$ in the NaCl/ZnCl$_2$ mixture, Figure 41.

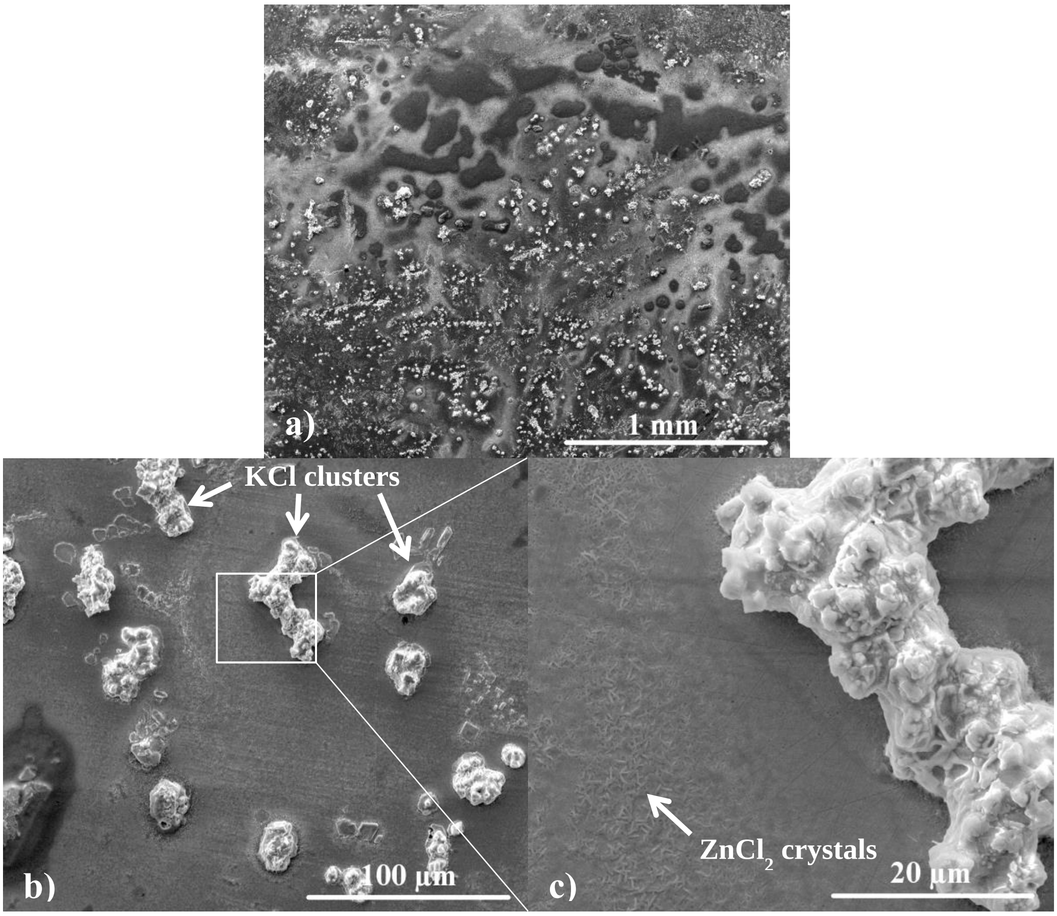

Figure 48: SE images showing that certain areas on the sample covered with KCl/$ZnCl_2$ contained KCl in the form of clusters that were sitting on top of a $ZnCl_2$ layer. Image a) shows an overview of such an area while image b), a magnified portion from the center of image a), shows the KCl clusters. Upon magnification, image c), $ZnCl_2$ crystals were visible.

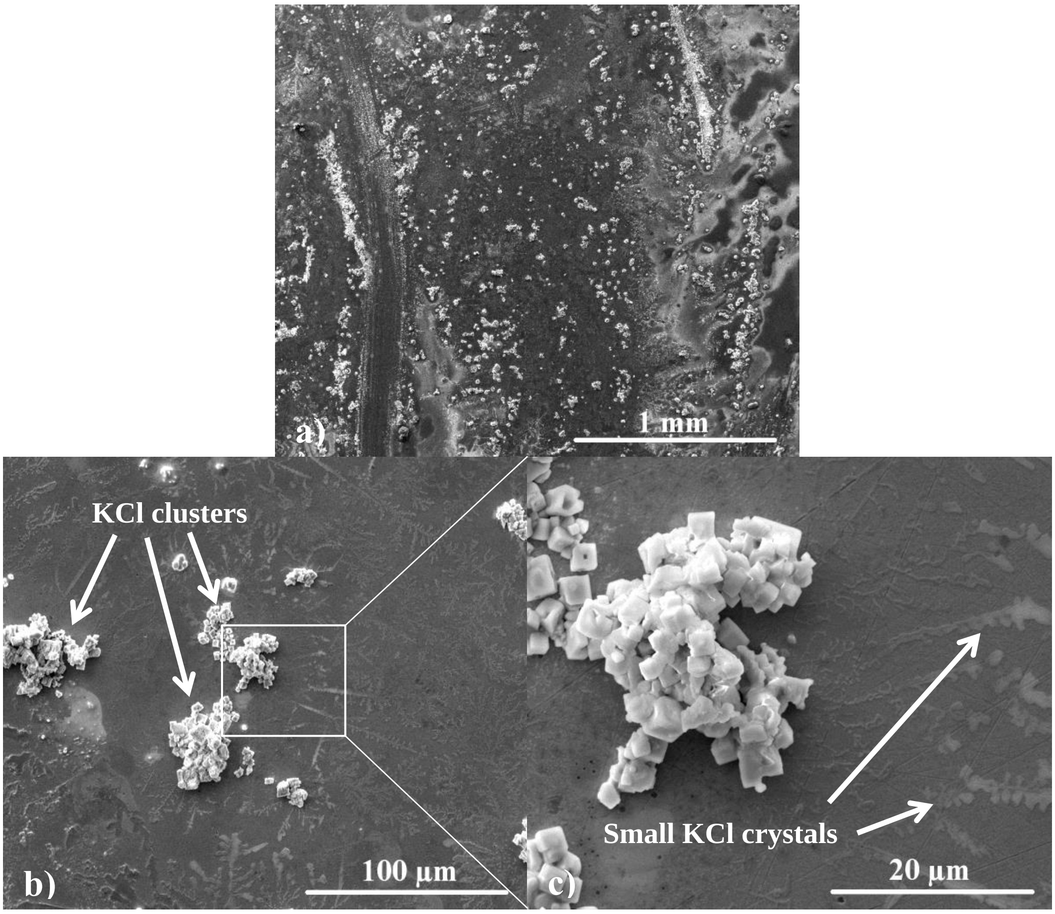

Figure 49: SE images showing an area on the KCl/ZnCl$_2$ coated sample that contained KCl clusters but no ZnCl$_2$ layer below. Image a) shows an overview while image b), a magnified portion from the center of image a), displays the KCl clusters. Upon magnification, image c), thin KCl crystals were visible.

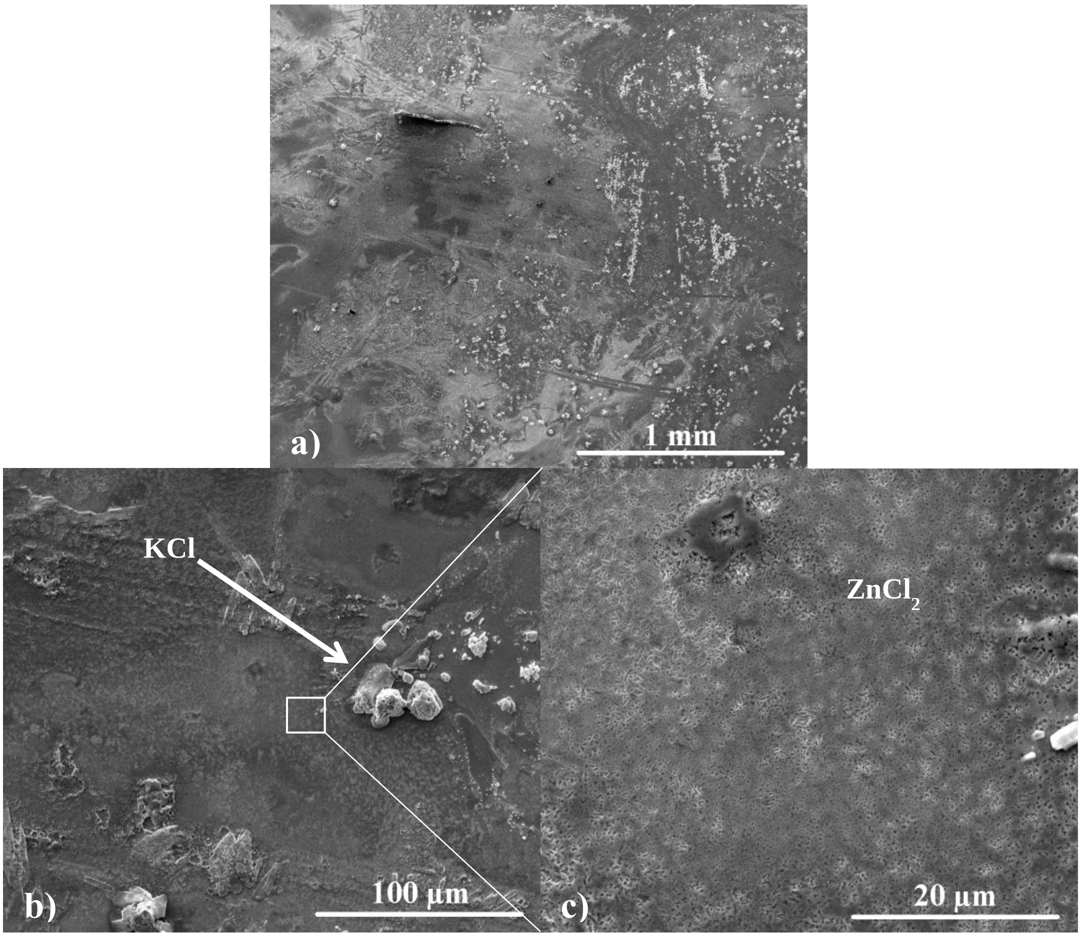

Figure 50: SE images showing that certain areas of the samples coated with KCl/$ZnCl_2$ had low amounts of KCl present. Image a) shows an overview while images b) and c) are magnifications. A layer of $ZnCl_2$ crystals is visible in image c).

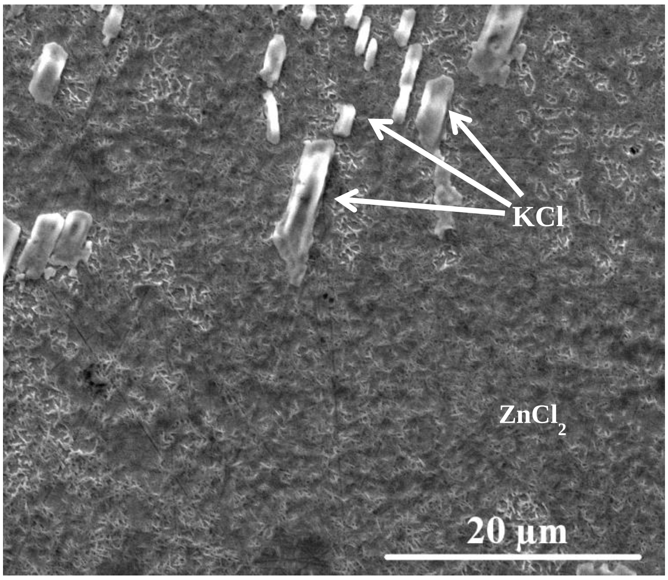

Figure 51: SE image showing that certain areas contained small KCl crystals on top of a $ZnCl_2$ layer.

7.4.13 KCl/ZnCl$_2$ 24 hour exposure

For the mixture consisting of KCl/ZnCl$_2$ the oxide was generally rough with traces of salt, as visible in Figure 52 and Table 18. Some areas had oxide nodules resting on top of a hematite layer as in area b) in Figure 52

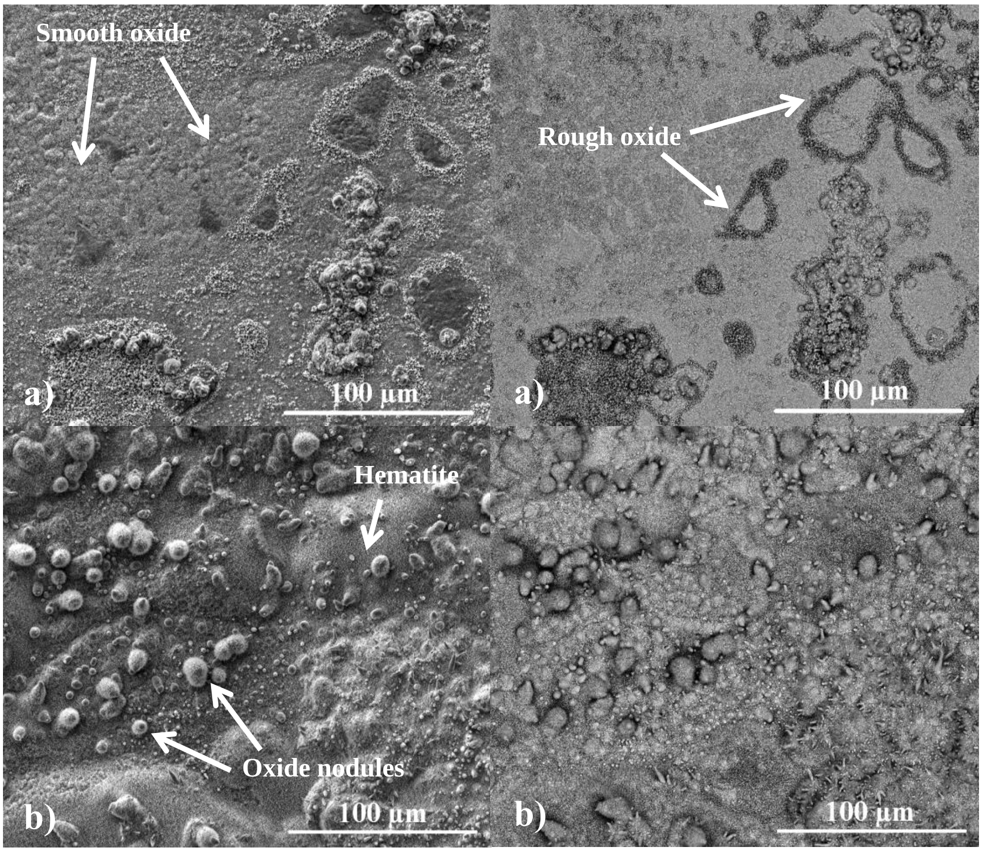

Figure 52: SE (left) and BSE (right) images of sample coated with a KCl/ZnCl$_2$-mixture and exposed in 5% O$_2$ + 40% H$_2$O for 24 hours at 400°C. Two areas were visible, a) and b).

EDX analysis was performed on a magnified portion of area a) in Figure 52 in the top left image. The results are presented below.

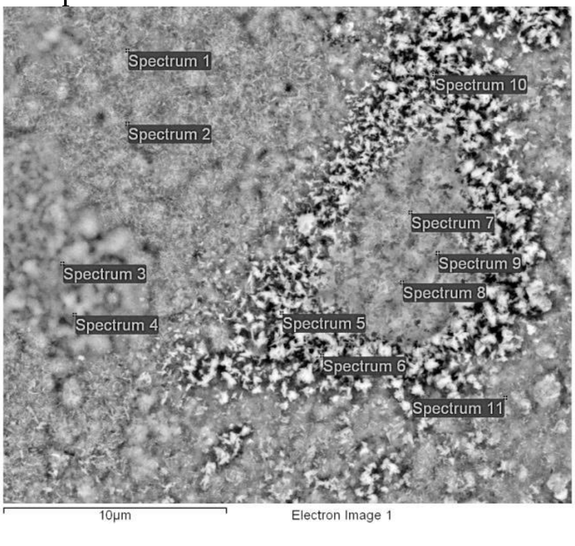

Figure 53: A magnified part of area a) in Figure 52 that was analysed with EDX.

Table 18: The results of the EDX analysis of the area in Figure 53 (atomic%). *=Trace elements.

Spectrum	**O**	**Cr***	**Fe**	**Zn***
Spectrum 1	68	0,0	32	0,0
Spectrum 2	71	0,2	28	0,4
Spectrum 3	73	0,1	26	0,0
Spectrum 4	73	0,1	27	0,0
Spectrum 5	67	0,2	33	0,0
Spectrum 6	37	0,4	63	0,0
Spectrum 7	71	0,1	28	0,6
Spectrum 8	59	0,2	41	0,0
Spectrum 9	21	0,4	78	0,0
Mean	60	0,2	40	0,1

EDX analysis was performed on a magnified portion of area b) in Figure 52. The results are presented below.

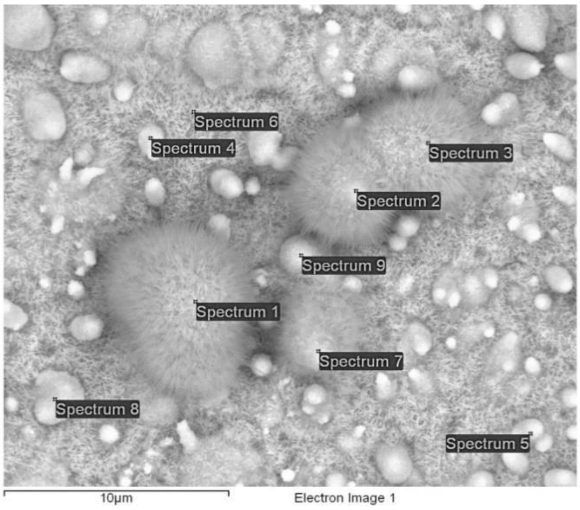

Figure 54: A magnified part of area b) in Figure 52 that was analysed with EDX.

Table 19: The results of the EDX analysis of the area in Figure 54 (atomic%). *=Trace elements.

Spectrum	**O**	**K***	**Cr***	**Fe**
Spectrum 1	70	0,0	0,3	30
Spectrum 2	61	0,0	0,5	39
Spectrum 3	65	0,0	0,5	34
Spectrum 4	63	0,0	0,6	36
Spectrum 5	74	0,2	0,2	26
Spectrum 6	70	0,2	0,2	30
Spectrum 7	71	0,3	0,3	29
Spectrum 8	67	0,3	0,4	32
Spectrum 9	67	0,3	0,4	32
Spectrum 10	66	0,2	0,4	34
Spectrum 11	64	0,0	0,5	36
Mean	67	0,1	0,4	33

Surface structures were visible on the exposed samples. Two examples are presented below.

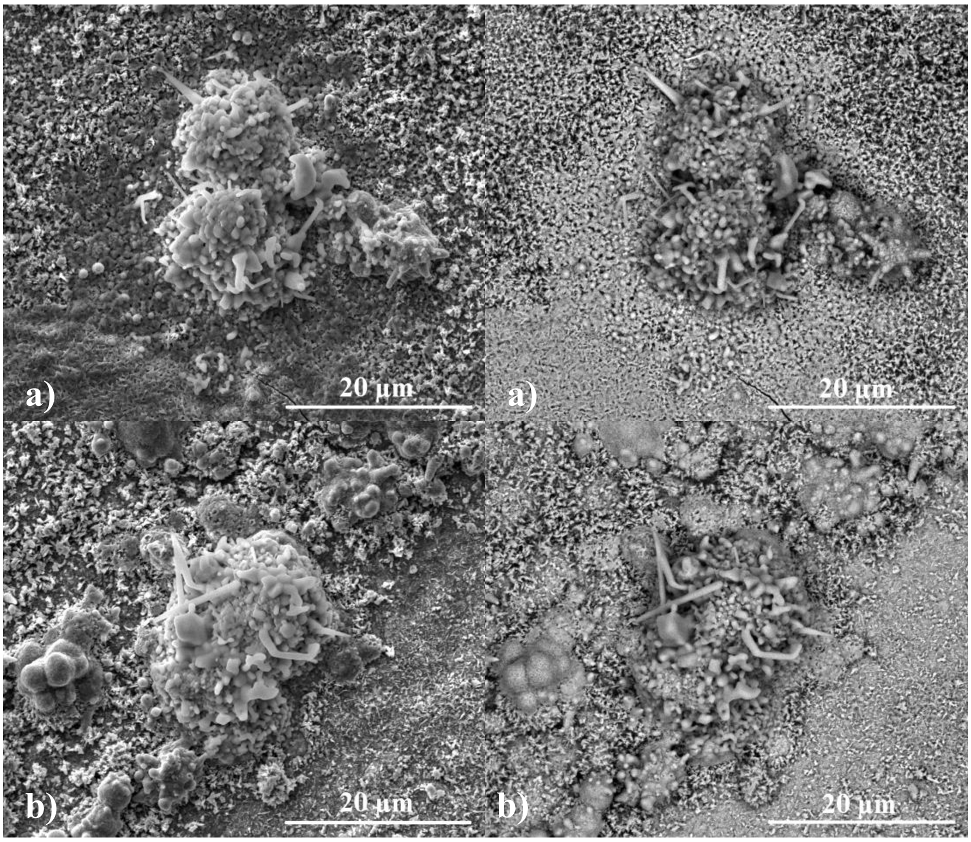

Figure 55: SE (left) and BSE (right) images showing a common type of structure present at different parts of the surface of a sample coated with a KCl/ZnCl2-mixture and exposed in 5% O_2 + 40% H_2O for 24 hours at 400°C (a and b).

EDX analysis was performed on the surface structure in area a) in Figure 55. The results are presented below.

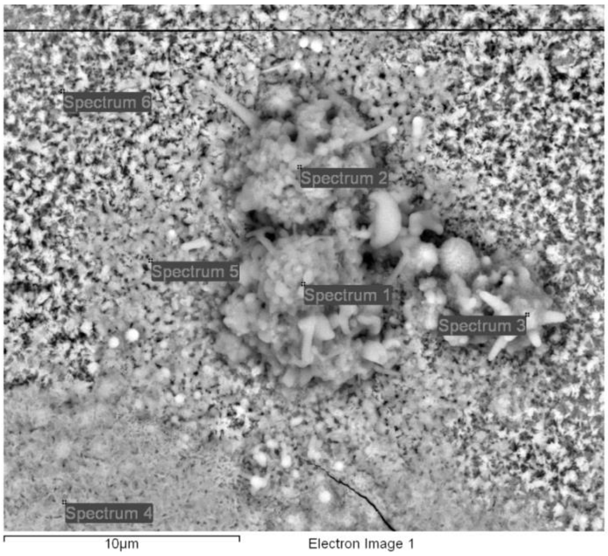

Figure 56: The structure in area a) in Figure 55 that was analysed with EDX.

Table 20: The results from the EDX analysis of the structure in Figure 56 (atomic%). *=Trace elements.

Spectrum	**O**	**Na***	**Cl**	**K**	**Cr***	**Fe**	**Cu***	**Zn***
Spectrum 1	27	0,0	27	25	0,0	18	0,5	1,4
Spectrum 2	40	0,0	20	19	0,2	20	0,0	1,2
Spectrum 3	72	0,0	1	1	0,1	25	0,0	0,6
Spectrum 4	70	0,0	0	1	0,3	29	0,0	0,0
Spectrum 5	60	0,6	0	0	0,5	39	0,0	0,0
Spectrum 6	58	0,0	0	0	0,6	42	0,0	0,0
Max.	55	0,1	8	8	0,3	29	0,1	0,5

As presented in Table 20, the relatively high K and Cl content as well as the minor Zn content in spectrum 1 and 2 suggests that the structure may be associated with the original KCl/$ZnCl_2$ salt coating. Trace amounts of Na and Cu could likely be a result of contamination. Another type of common structure was present at the exposed sample surface. It had a similar appearance as the structure in Figure 55 but a different composition:

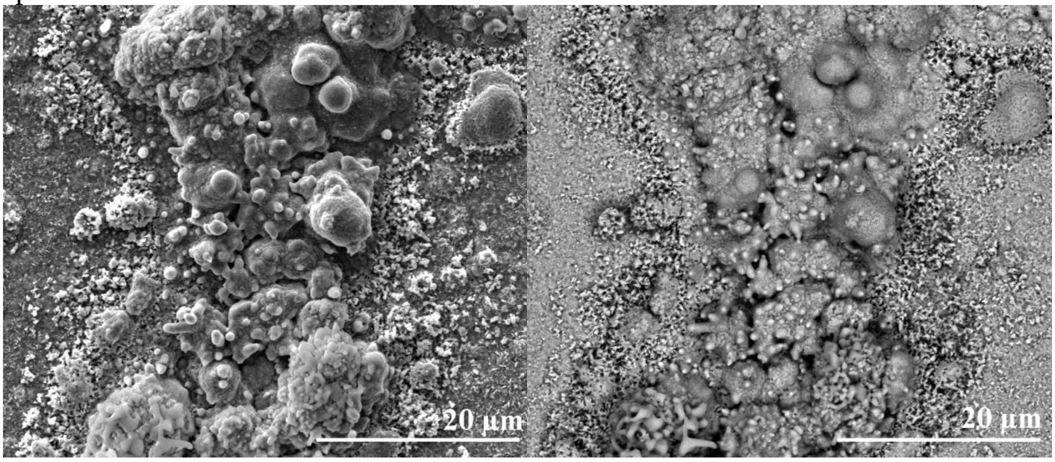

Figure 57: SE (right) and BSE (left) images showing another common type of structure present at the surface of a sample coated with a KCl/$ZnCl_2$-mixture and exposed in 5% O_2 + 40% H_2O for 24 hours at 400°C. The two images in Figure 57 are magnifications of the lower right part of area a) in Figure 52.

EDX analysis was performed on the common surface structure visible in Figure 57. The results of the analysis are presented below.

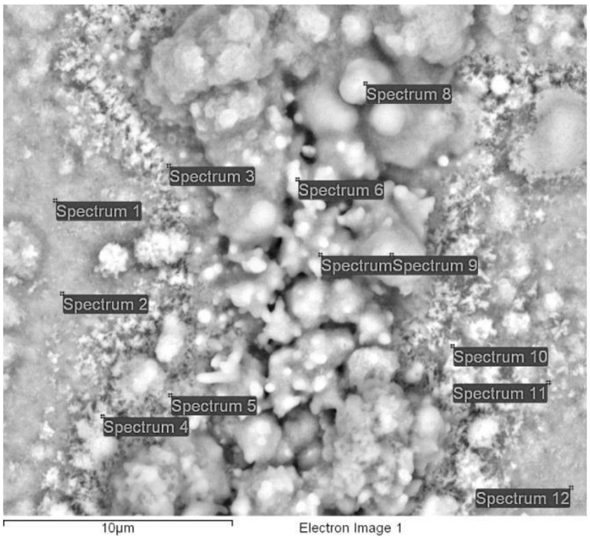

Figure 58: BSE image of the structure in Figure 57 that was analysed with EDX.

Table 21: The results of the EDX analysis of the structure in Figure 58 (atomic%). *=Trace elements.

Spectrum	**O**	**Cl***	**K***	**Cr***	**Fe**	**Zn***
Spectrum 1	60	0,2	0,1	0,9	39	0,0
Spectrum 2	63	0,0	0,0	1,0	36	0,0
Spectrum 3	34	0,2	0,5	1,2	64	0,0
Spectrum 4	73	0,2	0,2	0,3	26	0,6
Spectrum 5	69	0,2	0,4	0,4	30	0,3
Spectrum 6	76	0,3	0,7	0,2	23	0,2
Spectrum 7	67	0,3	0,8	0,2	32	0,3
Spectrum 8	75	0,4	0,7	0,2	23	0,3
Spectrum 9	73	0,9	1,0	0,2	24	0,4
Spectrum 10	71	0,2	0,2	0,4	28	0,3
Spectrum 11	56	0,1	0,2	1,2	43	0,0
Spectrum 12	62	0,2	0,1	0,8	37	0,0
Mean	65	0,3	0,4	0,6	34	0,2

As seen in Table 21, the area in Figure 58 mostly consisted of Fe oxide, likely Fe_2O_3. The composition of the surface structures is very different as is evident when comparing Table 20 and Table 21. The structure presented in area a) in Figure 55 is rich in K, Zn and Cl while the other type of structure as the one in Figure 57 only has traces of these elements.

The different salts and mixtures all had a visible effect on the surface morphology of the samples. A factor the different salts and mixtures had in common was that the oxide layer that formed was in many cases rough, non-adherent and damaged. To recapitulate, as explained in the section *The metal oxidation process* in order for an oxide to be protective, the oxide should among other criteria be well adherent and not be susceptible to mechanical stresses. When studying the SEM images for all systems, it is evident that the oxides formed do not fulfil these criteria, and that the oxides consequently should not be regarded as protective.

From Figure 15, it is clearly visible that the mass gains for the two salt mixtures are lower than for their two respective pure alkali salts. This is remarkable since the mixtures are thought to create eutectic melts during exposure which would increase the corrosion rate, as explained in the section *Chlorine induced corrosion*, which in turn would be indicated by an increased mass gain. This deviation might be explained by several theories discussed below.

One option is that the salt mixtures do not produce eutectic melts at all. Two causes are possible, where one does not rule out the other: The first explanation can be that the respective alkali chlorides are not mixed well enough with the $ZnCl_2$ when applied on to the sample surface. As has been presented in Figure 40, Figure 48 and Figure 49, the alkali chlorides do not precipitate onto the sample surface as discrete single crystals, but instead mainly as large clusters of many small crystals clustered together, forming a discontinuous alkali chloride coating. Even though small crystals can exist in the vicinity of certain KCl clusters as can be seen in Figure 49 c), the majority of the alkali chlorides seem to form large aggregates. This is in sharp contrast to how the evenly distributed pure NaCl and KCl crystals precipitate when applied as single salts, as is visible in Figure 18 and Figure 34. The $ZnCl_2$ on the other hand still seems to form a continuous layer as in the case with just pure $ZnCl_2$, which can be seen when comparing Figure 25, Figure 41 and Figure 48. This results in a fairly heterogeneous coating consisting of an even layer of $ZnCl_2$ covering the sample surface with large, more dispersed clusters of alkali chloride on top. As the only homogeneous mixture of the alkali and zinc chlorides becomes situated in the interface between the alkali chloride clusters and the underlying $ZnCl_2$, a eutectic melt that is formed may only be situated in these single, limited regions. Since much of the sample surface lacks this alkali chloride coating, the sample surface basically becomes covered in a two phase mixture that cannot create a eutectic melt at the exposure temperature that covers a substantial area of the samples. This can be justified by looking at Figure 4 and Figure 5, where a eutectic mixture is no longer possible when the alkali and zinc chlorides form two phase mixtures. It is however important to note that departure from the eutectic point does not prevent salt melt formation per se. Two-phase systems containing a solid solution and a salt melt are possible when examining Figure 4 and Figure 5. The corrosiveness of the actual salt melt in these systems should however be notably lower as a part of the system is in the solid state and does not partake in the oxide layer fluxing. Instead, the Cl content could cause corrosion via other mechanisms such as theories A and C presented in the section *Chlorine induced corrosion*.

Another possible explanation to why a eutectic melt cannot form is that the evaporation of $ZnCl_2$ affects the mixture composition, pushing it away from the eutectic point. Since the IC results in Table 6 show a high loss in Cl^- during exposure with pure $ZnCl_2$, this points towards a high loss of $ZnCl_2$ for the mixture exposures as well. Loss of $ZnCl_2$ is further indicated to be relatively high in comparison to the pure alkali chlorides when studying Table 5 for both the pure $ZnCl_2$ exposure as well as for the $NaCl/ZnCl_2$ and $KCl/ZnCl_2$ exposures: Only weak reflections for $ZnCl_2$ are seen after exposure for these three systems which points towards that only a small amount of $ZnCl_2$ is left on the sample surface after exposure while the alkali chlorides still give moderate to strong reflections. Furthermore, when studying Table 8, Table 9, Table 14 and Table 18 for the three Zn-containing systems post exposure only small amounts of Zn still seem to be present. As visible in Figure 4 and Figure 5, a loss of $ZnCl_2$ from the mixture would result in a shift in the melting temperature upwards for a homogeneous mixture. As more and more $ZnCl_2$ evaporates, the melting temperature of the mixture would become increasingly shifted towards that of pure alkali chloride, which at some point would make the presence of a eutectic melt impossible at the exposure temperature.

If the assumption that no melt forms is true, the lower mass gain for the mixtures would be a result of two things: Evaporation of $ZnCl_2$ and lower alkali chloride content on the sample prior exposure in comparison with the pure alkali chloride exposures. If the $ZnCl_2$ evaporates to a great extent, the remaining Cl^- available from the alkali choride would only be rougly half of the Cl^- available on the samples exposed with just pure alkali chloride. This is true because the same mass salt per sample area (0,1 mg/cm^2) was used for both the pure salts and the two mixtures. A 50/50 mixture would therefore yield 50% less alkali chloride in comparison with the pure alkali chloride systems, which in turn would result in a lower mass gain since the Cl^- is strongly associated with increased oxidation rate, as presented in the section *Chlorine induced corrosion*. This is consistent with the mass gains presented in Figure 15 and Figure 16.

Another theory that might explain why the salt mixtures yield a lower mass gain, while still causing a melt, is possible: Besides from the $ZnCl_2$ evaporation, alkali chlorides have also been shown to react into hydroxides and subsequently evaporate after desorption. For KCl, this process happens according to the following reaction [19]:

$$2KCl\,(s) + \frac{1}{2}O_2(g) + 2H_2O + 2e^- \rightarrow 2KOH(ads) + 2Cl^-(ads) \quad (12)$$

According to Folkeson, this evaporation is not negligible since the vapour pressure of KOH is higher than for KCl [19]. Taking this into consideration, the evaporation of $ZnCl_2$ combined with loss of KCl though evaporation of KOH would still allow for a homogeneous eutectic melt to be present. According to the reasoning above, where evaporation of $ZnCl_2$ shifts the mixture further away from the eutectic point as well as homogeneous melt regime, simultaneous evaporation of KCl would counteract this shift to at least some degree. Even though $ZnCl_2$ has a higher vapour pressure than KCl, the evaporation of $ZnCl_2$ could still be mitigated in some extent by the loss of KCl from the mixture, thus creating a smaller net shift from compositions with low melting temperature. The lower mass gain in comparison to the pure salt systems would in this case be attributed to the same factors as in the theory above: High loss of chloride salts through evaporation and less applied KCl on to the sample in comparison to the pure KCl exposures. For NaCl, the same reasoning can be made as the conversion of NaCl into NaOH followed by evaporation is possible. An indication of the presence of a melt might be seen in Figure 45 and Figure 55, where signs of a local attack are indicated in the form of a rougher oxide in the immediate vicinity of the salt-rich particles.

A noteworthy comment is that the salt melt induced corrosion may possibly not be as aggressive as other types of chlorine induced corrosion, when just using the mass gain as a measure for corrosion. According to Figure 16, the KCl system has the highest mass gain, followed by the two investigated mixtures and NaCl followed by $ZnCl_2$. As seen in Table 3, Figure 4 and Figure 5, KCl should be in the solid phase during exposure, while $ZnCl_2$, $NaCl/ZnCl_2$ and $KCl/ZnCl_2$ theoretically should be molten. Since the state of matter for the mixtures is uncertain due to the evaporation of salt discussed above, the mixtures are found in between KCl and $ZnCl_2$ in regards to state of aggregation. An inverse relationship then emerges, where the salt that should be molten, $ZnCl_2$, results in the lowest mass gain while the salt that exists in the solid state during the exposure, KCl, yields the highest mass gain. However, since the loss of $ZnCl_2$ is high due to evaporation, it is difficult to be certain that this is entirely true while also taking into account that the extent of corrosion cannot be judged by mass gain alone.

Another interesting observation regarding loss can be made when studying the results from the IC and XRD analyses. According to Table 6, the Cl^- loss for pure NaCl, KCl and $ZnCl_2$ after 24 hours is 35%; 43% and 77% respectively. When comparing these values with the Cl^- losses for the $NaCl/ZnCl_2$ and $KCl/ZnCl_2$ systems after 24 hours; 75% and 80% respectively, an increased loss of Cl^- is observed for the mixtures. If the Cl^- loss rate is assumed to be the same for the salt mixtures and that the mixture has a molar alkali chloride/zinc chloride ratio of exactly 50/50, the theoretical percentage Cl^- left should be given by the following formula:

$$\frac{50*\%Cl^-_{ZnCl_2}(left)+50*\%Cl^-_{AlkaliCl}(left)}{100} \qquad (13)$$

The theoretical values for $NaCl/ZnCl_2$ and $KCl/ZnCl_2$ according to equation (13) are 44% and 40% respectively when using the percentages from the 24 hour exposures. When comparing these theoretical numbers with the actual ones in Table 6 obtained in the IC analysis, it is obvious that the real values for the remaining Cl^- are approximately about half as high. This strongly indicates that the loss of Cl^- for the salt mixtures is greatly increased when compared to the corresponding values for the pure salts. For NaCl and $NaCl/ZnCl_2$, this is consistent with the XRD results shown in Table 5: While the NaCl reflections for the samples exposed with pure NaCl are strong to medium, the NaCl reflections for the samples exposed with the $NaCl/ZnCl_2$ mixture are medium to weak. This might be caused by three things: Less NaCl applied when part of a mixture, a higher rate of NaCl consumption when in a mixture with $ZnCl_2$ or a combination of the two. The higher rate of NaCl consumption would be consistent with the IC results, as the sole evaporation of $ZnCl_2$ cannot explain the higher loss of Cl^- according to the calculation above. The KCl does not follow the same pattern: While it is true that the IC results strongly indicate a higher Cl^- loss from the $KCl/ZnCl_2$ mixture when comparing the data in Table 6 with the calculated theoretical value obtained with equation (13), the XRD shows that the KCl reflection intensity is about the same when applied as a pure salt and as in part of a mixture, Table 5.

Another observation that supports the theory of an accelerated alkali chloride consumption is that no alkali chloride crystals are visible after exposure on the samples where mixtures had been applied. This is quite striking since alkali chloride crystals are visible for both the pure 24 hour NaCl and KCl systems respectively post exposure, as is evident in Figure 20 and Figure 37. Even when looking at the NaCl-covered sample exposed for 168 hours, Figure 24, NaCl crystals and craters post exposure are visible. The two mixtures on the other hand do not exhibit pure alkali chloride crystals, even though large clusters of NaCl and KCl respectively were seen prior exposure. Instead, porous surface structures containing a mixture of alkali, Cl, Zn, Fe and O is seen, and even though alkali and Cl are the major constituents, the structures do not consist of a single alkali chloride phase.

An explanation for the large difference in the corrosion, from a mass gain point of view, after exposure between the KCl and KCl/$ZnCl_2$ systems apart from $ZnCl_2$ evaporation can be that the KCl in the salt mixture forms agglomerates on top of the $ZnCl_2$ instead of single crystals. This can be seen when comparing Figure 16, Figure 34, Figure 48 and Figure 49, where the pure KCl coats the surface as discrete crystals, yielding the highest mass gain, while the KCl in the mixture forms larger agglomerates and therefore is less evenly distributed on the sample surface. The same theory might be applied to the NaCl/$ZnCl_2$-mixture as the NaCl does form clusters instead of small crystals that cover the sample surface evenly. The much larger clusters and therefore less evenly distributed crystals might cause the corrosion resulting from the alkali salts to reduce in extent and attain a much more local nature since the reactants are less dispersed and therefore not as available to participate in corrosive reactions.

While the sample coating in this work is performed with a pipette, the reference exposures for KCl have used salt spraying [19]. As the reported KCl crystal size in the reference is in between 50 and 100 µm, which is significantly larger than the size obtained in this work, Figure 34, this indicates that the crystal size does not influence the corrosion rate for KCl on T22, as the mass gains for the KCl exposures performed in this work and the reference KCl exposures are identical for the same exposure time.

8 Conclusions

All the investigated salts and mixtures increase the corrosion when compared to the clean reference samples. The increased mass gains as well as the rougher, thicker and more damaged oxide layer all point to that the extent of the metal oxidation increases.

The NaCl/$ZnCl_2$ and KCl/$ZnCl_2$ mixtures do not seem to increase the corrosion rate as much as their respective pure alkali chlorides. The mass gains for those systems are however significant and might be lowered by evaporation of $ZnCl_2$ during the first hours of exposure.

It is not clear whether the salt mixtures produce eutectic melts during exposure or not. Although indications of local salt melt attacks are seen, a homogeneous mixture of alkali chloride and $ZnCl_2$ is not obtained during the sample preparation. Two possibilities arise:

- No homogeneous eutectic melt is obtained during exposure due to that a thorough mixture of $ZnCl_2$ and alkali chloride does not form upon application prior exposure. Furthermore, loss of $ZnCl_2$ through evaporation shifts the melting temperature of the mixture to above exposure temperature. The corrosion observed is instead a result of other types of chloride induced corrosion.
- A eutectic or near-eutectic melt is formed, but in a much lesser extent than expected from a homogeneous salt mixture: Evaporation of both $ZnCl_2$ and alkali manage to keep the melting temperature low by conserving a near-eutectic composition, but the loss of salt mixture that can form a melt as well as loss of corrosive Cl^- through evaporation of $ZnCl_2$ results in a much more limited melt corrosivity during exposure.

Mixing the alkali chlorides with zinc chloride accelerates the loss of Cl^- during exposure, suggesting either an increased reaction rate for Cl^- or an increased evaporation rate for the chloride salts.

9 Future work

In order to determine the extent of corrosion caused by $ZnCl_2$, cross-sectional studies could be performed on samples exposed with pure $ZnCl_2$. Furthermore, to elucidate whether a local melt has been present and see how it has affected the oxidation of the metal, cross-sectional studies could also be performed on the $NaCl/ZnCl_2$ and $KCl/ZnCl_2$ systems in order to gain increased understanding of the behaviour of the mixtures during exposure.

To further determine the loss Na, K and Zn, ICP-OES could be performed as this is a crucial parameter that determines whether a melt can form.

The coating method could be improved as a homogeneous mixture obviously is not formed; a more evenly dispersed mixture would remove uncertainties regarding the distribution of the two constituent salts. This would increase the probability of eutectic melt formation.

In situ ESEM studies could be performed to monitor the onset of the corrosion caused by the mixtures. This could be used to confirm whether a melt is forming or not.

10 References

[1] Promotion of the use of energy from renewable sources: The European Union; [updated 09-07-2010; cited 2013 2/6]. Available from: http://europa.eu/legislation_summaries/energy/renewable_energy/en0009_en.htm.
[2] Directive 2009/28/EC, The European Union, (23-04-2009).
[3] 'Europe 2020': Green growth and jobs? : EurActiv; 2010 [cited 2013 2/6]. Available from: http://www.euractiv.com/priorities/europe-2020-green-growth-and-jobs-linksdossier-280116.
[4] Glossary:Biomass: Eurostat; [updated 29-11-2012; cited 2013 2/6]. Available from: http://epp.eurostat.ec.europa.eu/statistics_explained/index.php/Glossary:Biomass.
[5] Renewable energy primary production: biomass, hydro, geothermal, wind and solar energy: Eurostat; 2013 [updated 02-06-2013; cited 2013 2/6]. Available from: http://epp.eurostat.ec.europa.eu/tgm/table.do?tab=table&plugin=1&language=en&pcode=ten00082.
[6] Directive 2008/98/EC, The European Union, (19-11-2008).
[7] Treatment of waste: Eurostat; [updated 03-05-2013 cited 2013 6/6]. Available from: http://appsso.eurostat.ec.europa.eu/nui/show.do?dataset=env_wastrt&lang=en.
[8] Incineration: Eurostat; [updated 03-05-2013 cited 2013 6/6]. Available from: http://epp.eurostat.ec.europa.eu/portal/page/portal/waste/waste_generation_management/management/incineration.
[9] How is biomass converted to energy? : Canadian Centre for Energy; [cited 2013 6/6]. Available from: http://www.centreforenergy.com/AboutEnergy/Biomass/Overview.asp?page=4.
[10] Liske J, Svensson J-E, Johansson L-G, et al. Improved determination of service life of superheaters in boilers burning biomass and waste. 2013.
[11] Biodegradable Waste: European Commission; [updated 18-09-2012; cited 2013 6/6]. Available from: http://ec.europa.eu/environment/waste/compost/index.htm.
[12] Yin C, Rosendahl LA, Kær SK. Grate-firing of biomass for heat and power production. Progress in Energy and Combustion Science. 2008 12//;34(6):725-54.
[13] Summary of the EPA Municipal Solid Waste Program: U.S. Environmental Protection Agency; [updated 31/10/2013; cited 2013 8/6]. Available from: http://www.epa.gov/reg3wcmd/solidwastesummary.htm#term.
[14] Liske J. Alkali Induced High Temperature Corrosion of Stainless Steel - Experiences from Laboratory and Field. Göteborg, Sweden: Chalmers University of Technology; 2008.
[15] Vassilev SV, Baxter D, Andersen LK, et al. An overview of the chemical composition of biomass. Fuel. 2010;89(5):913-33.
[16] Gyllenhammar M, Herstad Svärd S, Davidsson K, et al. Additive for reducing operational problems in waste fired grate boilers. SP Sveriges Tekniska Forskningsinstitut, 2013.
[17] Waste: The European Commission; [updated 6/6/2013; cited 2013 8/6]. Available from: http://ec.europa.eu/environment/waste/index.htm.
[18] Smith WF, Hashemi J. Binary Eutectic Alloy Systems. Foundations of Materials Science and Engineering. 4 ed. Boston: McGraw-Hill; 2006.

[19] Folkeson N. Chlorine Induced Corrosion in Biomass and Waste Fired Boilers: Laboratory and Field Investigations. Gothenburg: Chalmers University of Technology; 2010.
[20] Nielsen HP, Frandsen FJ, Dam-Johansen K, et al. The implications of chlorine-associated corrosion on the operation of biomass-fired boilers. Progress in Energy and Combustion Science. 2000;26(3):283-98.
[21] High Temperature Materials for Power Engineering1990; Liège, Belgium: Kluwer Academic Publ.
[22] Uusitalo MA, Vuoristo PMJ, Mäntylä TA. High temperature corrosion of coatings and boiler steels in oxidizing chlorine-containing atmosphere. Materials Science and Engineering. 2003;346(1):168-77.
[23] Bramfitt BL, Benscoter AO. Carbon and Low-Alloy Steels. 2002. In: Metallographer's Guide: Practices and Procedures for Irons and Steels [Internet]. USA: ASM International. 1. [7].
[24] Other Steels – 16Mo3: Oakley Steel; [cited 2013 27/9]. Available from: http://www.oakleysteel.co.uk/16mo3.htm.
[25] Steel 13CRMO44: Metal Ravne; 2013 [cited 2013 27/9]. Available from: http://www.metalravne.com/selector/steels/13CRMO44.html.
[26] 304/304L Stainless Steel: AK Steel; 2007 [cited 2013 27/9]. Available from: http://www.aksteel.com/pdf/markets_products/stainless/austenitic/304_304L_Data_Sheet.pdf.
[27] Sanicro 28: Sandvik; [updated 29-03-2013; cited 2013 27/9]. Available from: http://www.smt.sandvik.com/en/materials-center/material-datasheets/tube-and-pipe-seamless/sanicro-28/.
[28] Jones DA. Principles and Prevention of Corrosion. 2 ed. Upper Saddle River, NJ: Prentice-Hall; 1996.
[29] Richardson TJA, Cottis B, Lindsay R, et al., editors. Shreir's Corrosion. 4 ed: Elsevier; 2010.
[30] Elliott RJ, Lira CT. Introductory Chemical Engineering Thermodynamics. Upper Saddle River, NJ: Prentice-Hall; 1999.
[31] Spiegel M. Corrosion in Molten Salts. In: Richardson TJA, editor. Shreir's Corrosion. Duisburg: Elsevier; 2010. p. 316-30.
[32] Grabke HJ, Reese E, Spiegel M. The effects of chlorides, hydrogen chloride, and sulfur dioxide in the oxidation of steels below deposits. Corrosion Science. 1995;37(7):1023-43.
[33] Enestam S, Bankiewicz D, Tuiremo J, et al. Are NaCl and KCl equally corrosive on superheater materials of steam boilers? Fuel. 2013;104:294-306.
[34] Li YS, Niu Y, Wu WT. Accelerated corrosion of pure Fe, Ni, Cr and several Fe-based alloys induced by $ZnCl_2$–KCl at 450°C in oxidizing environment. Materials Science and Engineering: A. 2003 3/25/;345(1–2):64-71.
[35] Viklund P, Hjörnhede A, Henderson P, et al. Corrosion of superheater materials in a waste-to-energy plant. Fuel Processing Technology. 2013;105:106-12.
[36] Bankiewicz D, Enestam S, Yrjas P, et al. Experimental studies of Zn and Pb induced high temperature corrosion of two commercial boiler steels. Fuel Processing Technology. 2013;105(1):89-97.
[37] Wang H, Li H, Yuan X-Z. Scanning Electron Microscopy. 2011. In: Pem Fuel Cell Diagnostic Tools [Internet]. Boca Raton: CRC Press.

[38] Leach RK. Scanning probe and particle beam microscopy. 2010. In: Fundamental Principles of Engineering Nanometrology [Internet]. UK: Elsevier Inc. 1.
[39] Goldstein JI, Lyman CE, Newbury DE, et al. Special Topics in Scanning Electron Microscopy. 2003. In: Scanning Electron Microscopy and X-ray Microanalysis [Internet]. New York: Springer Science. 3.
[40] Alford TL, Feldman LC, Mayer JW. X-ray Diffraction. Fundamentals of Nanoscale Film Analysis. New York: Springer US; 2007. p. 129-51.
[41] Smart LE, Moore EA. Solid State Chemistry. Boca Raton: CRC Press; 2005.
[42] Holze R. Diffraction and Other X-Ray Methods. 2009. In: Surface and Interface Analysis: An Electrochemist's Toolbox [Internet]. Berlin: Springer.
[43] König U, Gobbo L, Reiss C, editors. Quantitative XRD for Ore, Sinter, and Slag Characterization in the Steel Industry. 10th International Congress for Applied Mineralogy; 2011; Trondheim: Springer.
[44] Harris DC. Quantitative Chemical Analysis. 8 ed. New York: W. H. Freeman and Company; 2010.

Appendix 1

EDX analysis was performed on the crater edge in Figure 21: The results of the analysis are presented below.

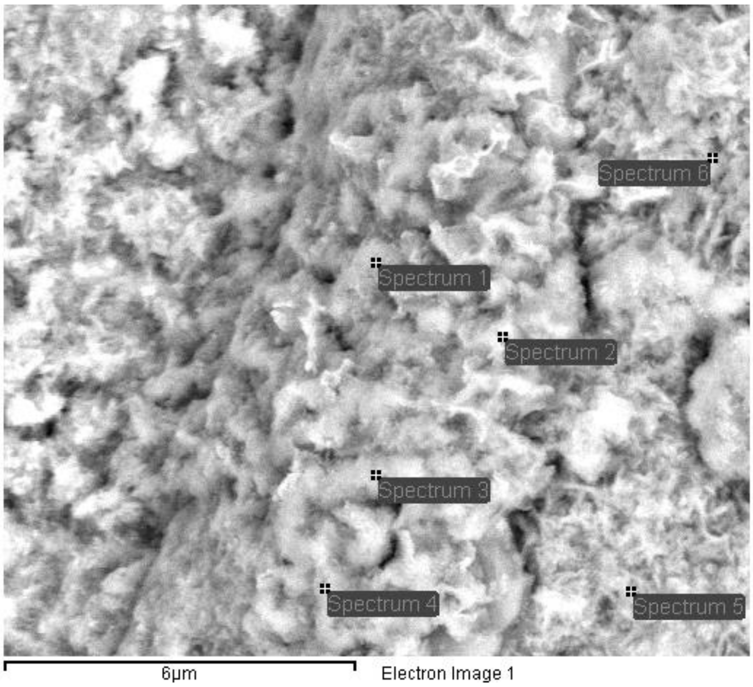

Figure 59: BSE image of the crater edge in Figure 21 that was analysed with EDX point analysis.

Table 22: Results from the EDX analysis from the area presented in Figure 59 (atomic%). *=Trace elements.

Spectrum	**O**	**Na**	**Cl***	**Mn***	**Fe**	**Cu***
Spectrum 1	54	3	0,1	0	39	4
Spectrum 2	60	5	1,2	1,4	31	1,5
Spectrum 3	60	3	0,5	0	37	0,5
Spectrum 4	60	3	0,3	0	37	0,8
Spectrum 5	65	3	0,2	0	32	0,3
Spectrum 6	60	3	0,1	0	37	0,5
Mean	59	3	0,4	0,2	36	1,3

EDX analysis was performed on an uncoated area on the sample exposed with NaCl for 24 hours. The results of the EDX analysis are presented below.

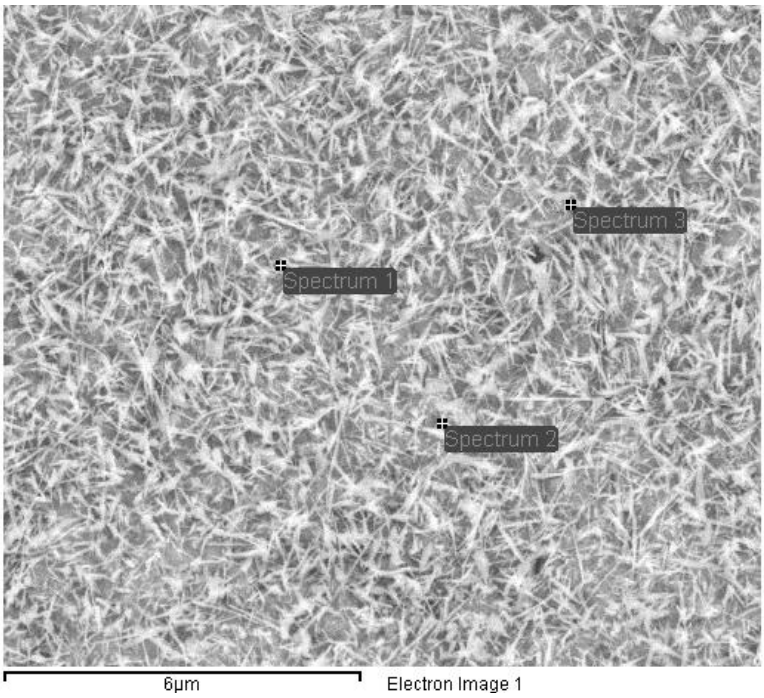

Figure 60: BSE image of an area on a sample exposed with NaCl for 24 hours that did not appear to become coated by salt that was later analysed with EDX.

Table 23: Results from the EDX analysis form the area presented in Figure 60 (atomic%). *=Trace elements.

Spectrum	**O**	**Cr***	**Fe**
Spectrum 1	59	0,4	40
Spectrum 2	59	0,6	40
Spectrum 3	59	0,6	41
Mean	59	0,5	41

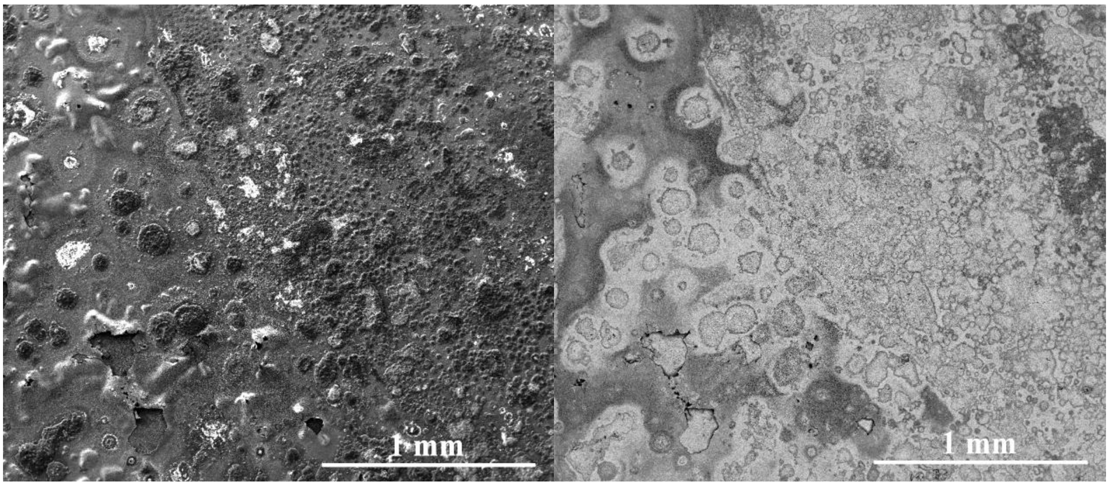

Figure 61: SE (left) and BSE (right) images of a sample coated with KCl and exposed in 5% O_2 + 40% H_2O for 24 hours at 400°C. The images summarize the surface features visible together as well as separate by themselves all over the sample surface.

EDX analysis was performed on a magnified portion in area b) in Figure 35. The results are presented below.

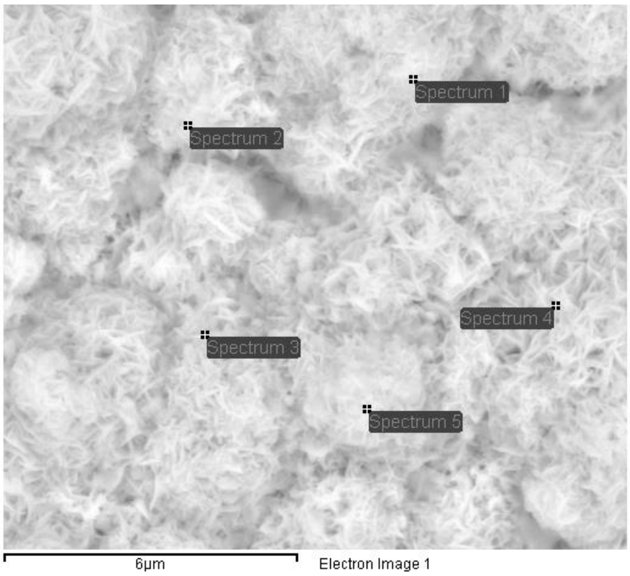

Figure 62: The area in image b) in Figure 35 that was analysed with EDX.

Table 24: The results of the EDX analysis of the area in Figure 62 (atomic%). The coarser area analysed where spectra 1, 2 and 6 were taken are slightly richer in K. *=Trace elements.

Spectrum	**O**	**Cl***	**K**	**Cr***	**Fe**
Spectrum 1	67	0,3	2	0,0	32
Spectrum 2	55	0,4	2	0,0	43
Spectrum 3	73	0,6	2	0,2	25
Spectrum 4	63	0,6	2	0,1	34
Spectrum 5	69	0,3	2	0,1	29
Mean	65	0,4	2	0,1	33

EDX analysis was performed on a magnified portion in area c) in Figure 35. The results are presented below.

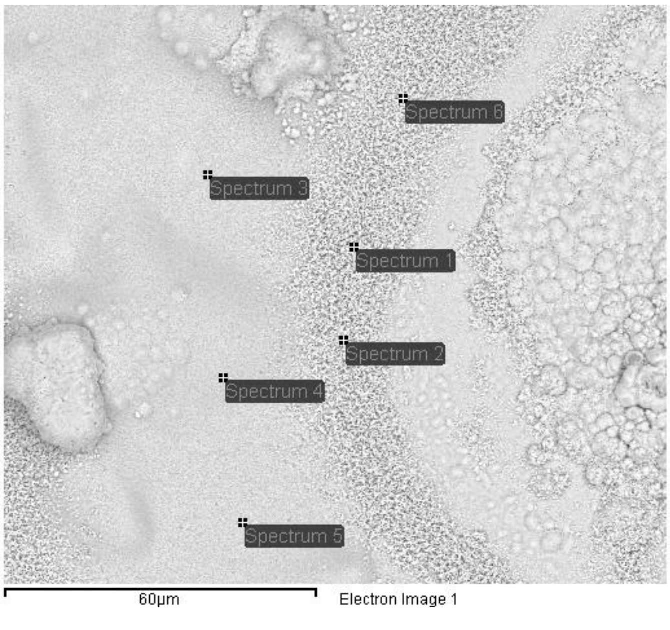

Figure 63: The area in image c) in Figure 35 that was analysed with EDX.

Table 25: The results of the EDX analysis of area in Figure 63 (atomic%). *=Trace elements.

Spectrum	**O**	**Si***	**K***	**Cr***	**Fe**
Spectrum 1	64	0,0	0,3	0,2	35
Spectrum 2	58	0,0	0,3	0,2	42
Spectrum 3	68	0,0	0,0	0,2	32
Spectrum 4	64	0,3	0,2	0,1	35
Spectrum 5	65	0,0	0,0	0,2	35
Spectrum 6	67	0,0	0,4	0,2	32
Mean	64	0,1	0,3	0,2	35

EDX analysis was performed on a magnified portion in area d) in Figure 35. The results are presented below.

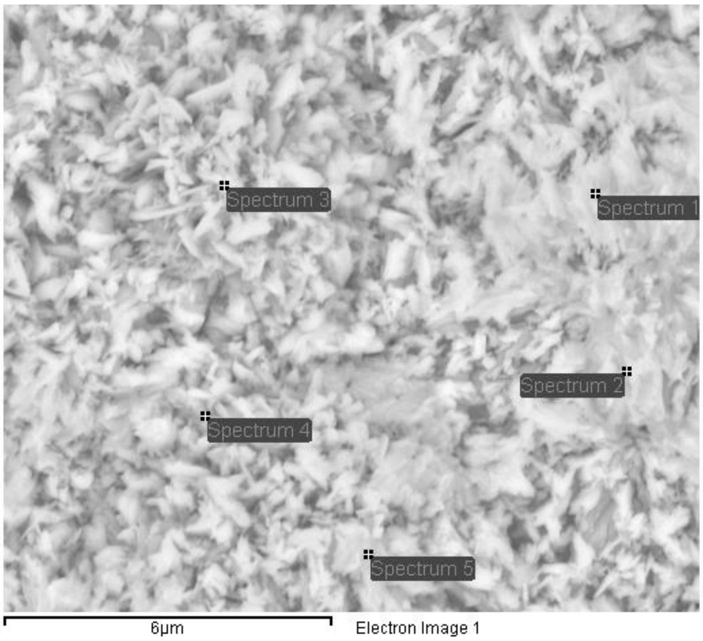

Figure 64: The area in image d) in Figure 35 that was analysed with EDX.

Table 26: The results of the EDX analysis of area in Figure 64 (atomic%). *=Trace elements.

Spectrum	**O**	**Si***	**K***	**Fe**
Spectrum 1	69	0,0	0,2	31
Spectrum 2	62	0,0	0,0	38
Spectrum 3	71	0,3	0,3	28
Spectrum 4	66	0,0	0,2	33
Spectrum 5	70	0,0	0,1	30
Mean	67	0,1	0,2	32

EDX analysis was performed on a magnified portion in area c) in Figure 42. The results are presented below.

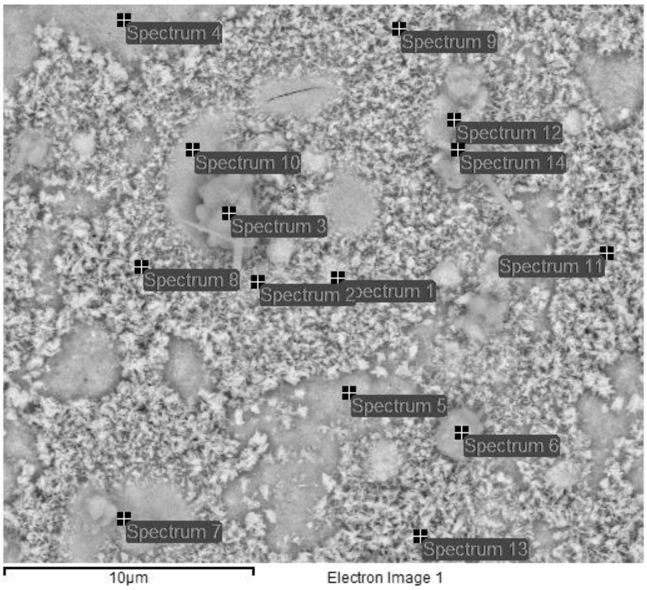

Figure 65: A magnification of area c) in Figure 42 that was analysed with EDX.

Table 27: The results of the EDX analysis of the area in Figure 65 (atomic%). The surface composition is relatively heterogeneous with some NaCl-rich particles resting on top. *=Trace elements.

Spectrum	**O**	**Na**	**Cl**	**Cr***	**Mn***	**Fe**	**Cu***	**Zn***
Spectrum 1	66	1	0	0,2	0,0	33.	0,0	0,0
Spectrum 2	68	2	1	0,2	0,1	29	0,0	0,0
Spectrum 3	37	27	8	0,1	1,0	25	0,6	0,9
Spectrum 4	64	0	0	0,2	0,2	36	0,0	0,0
Spectrum 5	62	0	0	0,3	0,2	38	0,0	0,0
Spectrum 6	44	25	9	0,1	1,0	19	0,4	1,0
Spectrum 7	62	2	1	0,2	0,2	35	0,0	0,0
Spectrum 8	71	2	0	0,2	0,0	27	0,0	0,0
Spectrum 9	59	0	0	0,4	0,2	40	0,0	0,0
Spectrum 10	64	4	0	0,2	0,2	31	0,2	0,0
Spectrum 11	56	0	0	0,6	0,2	44	0,0	0,0
Spectrum 12	51	4	1	0,3	0,3	43	0,5	0,0
Spectrum 13	65	1	0	0,3	0,2	34	0,0	0,0
Spectrum 14	50	17	5	0,2	0,4	26	0,5	0,5
Mean	59	6	2	0,3	0,3	33	0,2	0,2